# NANOWIRE-BASED ALTERNATING CURRENT OXIDE POWDER ELECTROLUMINESCENT MATERIALS AND DEVICES

By

SIWEI MA, M.ENG., B.S.

A Thesis Submitted to the School of Graduate Studies in Partial Fulfillment of the Requirements for the Degree Doctor of Philosophy

DOCTOR OF PHILOSOPHY (2019) McMaster University

Materials Science & Engineering Hamilton, Ontario

TITLE: Nanowire-Based Alternating Current Oxide Powder Electroluminescent Materials and Devices

AUTHOR: Siwei Ma, M. Eng. (University of Science and Technology, Beijing), B.S. (Yunnan University)

SUPERVISOR: Professor Adrian H. Kitai

NUMBER OF PAGES: xvi, 137

# Abstract

A novel type of alternating-current (AC) powder electroluminescent (EL) device that relies on nanowire-phosphor heterogeneous junction structure has been developed. It shows promise for manufacturing of highly stable powder EL devices. To pursue this goal, manganese ion ($Mn^{2+}$)-doped zinc germanate ($Zn_2GeO_4$:Mn) oxide phosphor was synthesized and used as EL powder material for the fabrication of the new types of AC powder EL devices. The $Zn_2GeO_4$:Mn oxide phosphor powder could eliminate the well-known degradation problem of zinc sulfide (ZnS)-based AC powder EL devices predominant in the current marketplace.

In order to realize a high brightness at a relatively low operating voltage, a conductive semiconductor nanowire architecture using zinc oxide (ZnO) and copper oxide (CuO) nanowires with sharp-tip features, was created and integrated into conventional AC powder EL structures. Particularly, vertically-aligned *n*-type ZnO nanowires arrays were successfully synthesized on a $Zn_2GeO_4$:Mn polycrystalline substrate for the first time, and the growth behavior using a chemical vapor deposition (CVD) process was investigated. The density of the ZnO nanowires could be effectively controlled by some experimental parameters, such as the density of gold catalyst nanoparticles, and spatial distance between substrate and CVD source powders. This novel ZnO nanowire-decorated $Zn_2GeO_4$:Mn phosphor architecture was used to fabricate top-emission AC powder EL devices. On the other hand, a vertically-aligned ZnO nanowire array was directly synthesized on a thin film indium-tin-oxide (ITO)-coated glass substrate for fabrication of bottom-emission AC

powder EL device. The nanowires were adopted to form heterogeneous junction structures between the tips of the nanowires and the $Zn_2GeO_4$:Mn EL powders, so that the composites could have a similar electrical field enhancement as in the needle-like $Cu_xS$ precipitates within widely-used ZnS:Cu EL powder materials. The behavior of these top- and bottom-emission AC powder EL devices was also studied.

Alternatively, vertically-aligned *p*-type CuO nanowires were prepared by a thermal oxidation method. Reliable heterogeneous junction structures were formed by a simple drop-coating method. The CuO nanowire-based AC powder EL device has excellent brightness maintenance with a loss of luminescent intensity under 1 % at over 10 cd/$m^2$ luminance during 360 hours of operation. The integrating of semiconductor nanowires into conventional AC powder EL device structures offers the very promising prospect of fabrication of simple, low-cost, scaled-up EL devices that could fundamentally solve the limited operational lifetime of current ZnS-based AC powder EL devices.

# Acknowledgements

First of all, I would like to express my deepest gratitude to my supervisor, Professor Adrian Kitai, who is not only a wonderful supervisor but a nice friend. I have been very fortunate to study and work with him. His solid expertise, hardworking attitude, research enthusiasm, and endless pursuit for high quality research impressed me deeply and set a great example for my future career. I very appreciate his great patience and tolerance during the entire period of my Ph.D. study.

I also sincerely thank all my committee members, Professor Igor Zhitomirsky and Professor Anthony Petric, for their encouragements, constructive suggestions, and insightful comments on my research. I am very grateful to Dr. Zhilin Peng for his good suggestion and help with SEM characterization. Assistance and support from technicians and staff members at McMaster University, Xiaogang Li, Doug Culley, Carmen Andrei, Andy Duft, Jim Garret, Jim Britten, Chris Butcher, and Victoria Jarvis were also greatly appreciated. The work could not go smoothly without their kind help.

It was my great pleasure to work at the Department of Materials Science and Engineering of McMaster University. I enjoy the happy time with my wonderful group members, Samuel Peter, Andrea Beauchamp, Eric Zhao, Lei Wang, Sirui Tan. I am also truly thankful to my friends at McMaster University, Kaiyuan Shi, Juan Wu, Yangshuai Liu, Chao Zheng,

Kezhuan Gu, Peng Dong, Yi Feng, Weiwei Zhang, Yinan Jiao, Minghe Wang, for their generous help in my work and life.

Last but not least, I would like to thank my dear parents and my wife Hanshuo Liu for their selfless love and endless support in my Ph.D. study and life. Their understanding and encouragement is the largest motivation in my life.

# Table of Contents

# List of Abbreviations and Symbols

| | |
|---|---|
| AC | Alternating Current |
| BEM | Boundary Element Method |
| CIE | Commission Internationale de l'Eclariage |
| CRT | Cathode Ray Tube |
| CVD | Chemical Vapor Deposition |
| DC | Direct Current |
| EDS | Energy Dispersive X-ray Spectroscopy |
| EL | Electroluminescence |
| EXAFS | Extended X-ray Absorption Fine Structure |
| FFT | Fast-Fourier Transform |
| FWHM | Full width at Half Maximum |
| HMTA | Hexamethylenetetramine |
| HRTEM | High-Resolution Transmission Electron Microscopy |
| LED | Light-Emitting Diode |
| MOCVD | Metal-Organic Chemical Vapor Deposition |
| PL | Photoluminescence |
| PMMA | Methylmethacrylate |
| SCCM | Standard Cubic Centimeters Per Minute |
| SEM | Scanning Electron Microscopy |
| TEFL | Thin-Film Electroluminescent |
| TEM | Transmission Electron Microscopy |
| UV | Ultraviolet |
| VLS | Vapor-Liquid-Solid |
| $V_{th}$ | Threshold Voltage |
| XRD | X-ray Diffraction |

# List of Figures

# List of Tables

# Chapter 1. Introduction

Electroluminescence (EL) describes the phenomenon by which electrical energy is converted to visible light emission other than by black body radiation. Therefore, EL sometimes is called 'cool light'. Historically, the EL phenomenon was first discovered in 1936, when Destriau [1] observed light emission from zinc sulfide (ZnS) phosphor powders dispersed in a transparent insulator and sandwiched between two electrodes connected to an external applied voltage. Depending to the phosphor configuration, EL devices may be categorized into two types: thin film EL (TFEL) and powder EL. TFEL is commercially available for environmentally demanding display applications. Alternating-current (AC) powder EL has long been used in nightlights, backlights of liquid crystal displays such as in illumination of panels since the 1970s [2]. In comparison with TFEL devices, AC powder EL devices are usually fabricated in a low-cost way, and an outstanding advantage of AC powder EL devices is that the emission colors can be easily adjusted by adopting a range of phosphor powders with a variety of emission colors. Other characteristics, such as uniform light emission, low power consumption, and excellent flexibility, provide AC powder EL device with significant application potentials in current market [3-12]. Conventionally, the light-emitting materials used in AC powder EL devices have been limited to sulfide-based phosphor powder such as ZnS:Cu phosphor. Electrically conductive $Cu_{2-x}S$ nanoprecipitates form regions of enhanced electric fields within the ZnS and field emission and hence electroluminescence is enabled [13-16]. However, AC

powder EL devices assembled with sulfide-based phosphor materials are well known to deteriorate during continued operation [17-22]. In addition, sulfide-based phosphor materials are sensitive to moisture leading to the requirement for encapsulation which adds cost. The degradation process of sulfide-based EL devices is accelerated as operating temperature increases [18,20]. Therefore, these inherent drawbacks of the sulfide-based phosphor materials used for commercially available AC powder EL devices cause instability and the consequent short-term reliability, which greatly inhibits the practical application of AC powder EL devices.

Oxide phosphor materials have recently attracted much attention because of their excellent physical and chemical stability, low-cost, and convenient manufacturing method [23-32]. Using oxide phosphor materials in AC powder EL devices could eliminate the instability problem and satisfy the requirement for long lifetime application. However, the threshold voltage needed to excite EL emission in oxide phosphor-based devices is too high to produce practically bright and efficient EL emission. To address this problem, nanowire-type architectures are proposed in this thesis to form intimate contact with oxide phosphor powders. By taking advantage of the field-enhancement property originating from the needle-like structure of the nanowires with a sharp-tip morphology, nanowires are shown to significantly improve the performance of oxide-based AC powder EL devices.

Three types of AC powder EL device formed by integrating semiconductor nanomaterials are presented in this thesis. Therefore, an AC powder EL device including development history, materials, structure, and underlying operating principles will be examined in detail. The structure of this thesis is illustrated as follows: Related background,

development of AC powder EL devices, necessary fundamental knowledge, and literature review of previous work are elaborated in Chapter 2. In Chapter 3, the experimental details and characterization techniques are described, and especially the conventional synthesis methods of oxide semiconductor nanowire are emphasised. Following that, the investigation of the ZnO nanowire growth behavior and the performance of the ZnO-based nanowires in AC powder EL devices is systematically demonstrated in Chapter 4. Chapter 5 shows the synthesis of *p*-type CuO nanowires and EL performance of the CuO nanowires-based AC powder EL devices.

At the end of the thesis, Chapter 6 concludes the work accomplished in this thesis. The suggested future work and possible technique routes to achieve the goal are discussed in Chapter 7.

# Chapter 2. Literature Review

## 2.1 Overview of AC Powder Electroluminescence (EL) Devices

### 2.1.1 Development of AC powder EL devices

In 1936, French scientist Georges Destriau [1] reported light emission in zinc sulfide (ZnS) powder activated with an excess of copper, which was suspended in castor oil when a strong electric field was applied. This type of EL is recognized as powder EL today. Figure 2.1 shows the original structure of the Destriau cell [2].

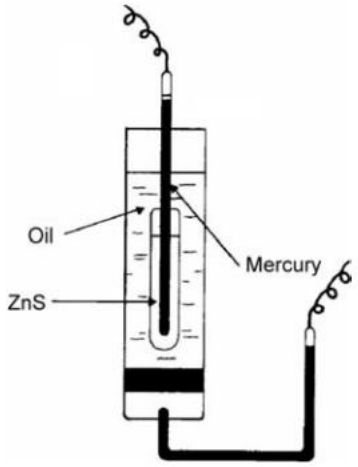


**Figure 2.1** The original Destriau EL cell [2].

This was the first record of EL in phosphor powder materials under applied voltage and was known as the 'Destriau effect'. At the very beginning, there was great difficulty in devising a structure in which he could apply high fields to a thin layer of powder to generate

visible light since transparent electrically conductive coatings on glass were not available at that time. Therefore, the device structure he used was a large capacitor with a mercury electrode. However, this structure was soon modified to a demountable capacitor, as shown in Figure 2.2 [33].

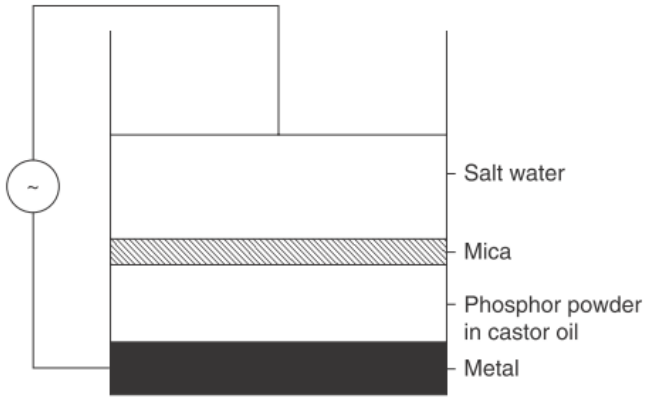


**Figure 2.2** Schematic diagram of a modified Destriau EL cell [33].

In this structure, the phosphor powder was mixed with castor oil and spread in a thin layer on a metal plate. An insulating transparent mica layer was placed on the top of the phosphor-castor oil layer. Over the mica layer is a layer of salt water used as top electrode in place of a solid state transparent conducting electrode. This structure enabled immediate light emission in a high electric field although the AC voltage could be up to 15 kV and the EL was extremely poor. This EL effect received little attention in the following decades after Destriau's observation. Even in 1950, Leverenz questioned the EL mechanism of the light emission of the powder phosphor and stated that it might in fact be excited by ultraviolet (UV) light, which is produced by the electrical breakdown of the gases in the fairly porous powder phosphors [34].

During the Second World War through to the late 1940s, development of high-performance polymers and ceramics was initiated. More importantly, transparent conducting electrodes were achieved for the first time. These developments triggered great interest in AC powder EL devices. From the 1950s to the middle of 1960s, AC powder EL devices were widely studied in very many of the world's major electronic laboratories. Enormous academic and industrial research efforts were devoted to powder EL display devices [35,36].

Generally, AC powder EL devices possess a simple device structure and can be fabricated with a low-cost manufacturing method. In particular, at a low luminance of 3.4 $cd/m^2$, lifetime (defined as operating time for the luminance to drop to half of its original luminance) is close to infinite [37]. AC powder EL devices have been known to operate continuously for over ten years at 100V rms at 60 Hz. Furthermore, the materials used in AC powder EL devices are generally inorganic polycrystalline solids rather than the single crystal materials used in LED devices. This feature permits large area devices to be manufactured at a competitively low price. Highly uniform light emission over large areas is available mainly due to the polycrystalline nature of AC powder EL devices. The light emitted from each grain of phosphor material is normally not seen as a distinct source by the observer, and the light per unit area emitted is the result of numerous grains or crystals. For this reason, a less perfect material than single crystal LED materials is capable of creating highly reproducible lighting without requiring the binning associated with LED devices. However, AC powder EL devices face several significant challenges for display applications: (1) low discrimination ratio, which is defined as the ratio of luminance at V

to the luminance at V/2; (2) low contrast ratio; and (3) short lifetime at moderate to high luminance [2].

The low discrimination ratio is due to the fundamental physics of the light emitting mechanism of the AC powder phosphor. It is well-known that an AC powder EL device does not exhibit a sharp threshold voltage in its brightness-voltage characteristic. This feature indicates that a powder EL device is not suitable for high-resolution passive matrix multiplexed displays. One way to overcome this issue is to incorporate a Thin Film Transistor (TFT) drive circuit into the powder EL device display as suggested by Fischer in 1971 [38] and explored by Brody [39]. Unfortunately, experimental devices had a considerable number of blemishes, resulting from poor quality of the TFTs. Meanwhile, TFTs were at their early stage and amorphous silicon technology did not exist at that time. Therefore, this technology was soon abandoned.

The low contrast ratio in moderate to high ambient illumination is due to the high reflectivity of the powder phosphor itself. Filters can be used to increase contrast ratio at the cost of decreased luminance. Consequently, higher voltages and frequencies were required to drive the display, which greatly decreased the lifetime of the AC powder EL display devices.

The short lifetime at moderate to high luminance is due to the exponential decay feature of the AC powder EL phosphor materials. Fischer [38] explained that the decay in brightness is related to the blunting of nano-scale $Cu_{2-x}S$ precipitates (see section 2.1.4) occurring by the diffusion of copper ions the ZnS lattice upon application of high AC electric fields. The degradation is further aggravated by a high moisture environment, high

operating temperature and frequency. At about 170 cd/m$^2$, in most cases, the lifetime of powder EL lamps is only 1000 hours.

In spite of considerable technical effort from the 1950s to the mid1960s, the inability to improve the lifetime of AC powder EL displays lead to its disfavor in the late 1960s. At the same time, other technologies, such as gas discharge, LEDs, vacuum fluorescence, liquid crystals and thin film electroluminescence, attracted more and more research interest. These newly emerging technologies greatly diminished interest in powder EL devices. By the end of 1974, when the Sharp Company developed a double-insulator AC thin film electroluminescent display with high performance and reliability, almost all the research and development teams at the various AC powder EL companies throughout the United States were disbanded [37]. Since then, little fundamental work has been reported, although important progress has been achieved in packaging. A chemical vapor deposition method is now used to encapsulate ZnS:Cu,Cl phosphor powders with a Ti-Si-O film coating in order to improve the lifetime by preventing moisture penetration [40]. By maintaining constant current or constant power, lifetime of an AC powder EL device producing 200 cd/m$^2$ has been extended to more than 3000 hours [41].

### 2.1.2 Structure and Materials of AC Powder EL Devices

A typical structure of an AC powder EL device consisting of ZnS:Cu,Cl phosphor material is shown in Figure 2.3 [2]. To date, the widely-used powder phosphors excited by an alternating electric field are limited to a comparatively small group of phosphors, mainly of the ZnS type. As shown in Figure 2.3, the phosphor layer consists of suitably doped ZnS

powders with particle size of 5~20 μm suspended in a dielectric matrix which acts as a binder as well. This phosphor layer is 50~100 μm thick and is sandwiched between two electrodes, one of which is transparent and is supported by a substrate made of either glass or flexible plastic. The colour of light emitted from the device is determined by the luminescence centers in the ZnS phosphor materials. For example, one of the most common ZnS phosphors used in AC powder EL devices is the green-emitting ZnS:Cu,Cl (or Al) material. In this material, the Cu luminescence center acts as an acceptor and is partly responsible for the colour of the emission, while Cl (or Al) serves as a donor which also impacts emission colour. The amount of Cu added in the preparation process of these phosphors is $10^{-3}$ to $10^{-4}$ (mass ratio) of ZnS and is one order of magnitude larger than that added to ZnS phosphors used in CRTs.

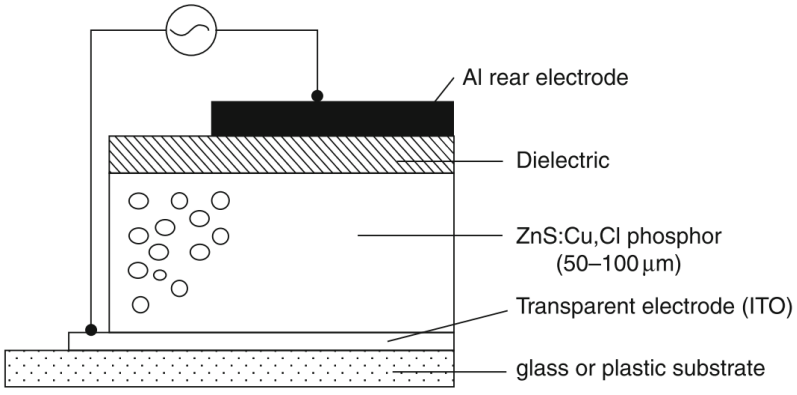


**Figure 2.3** Typical structure of ZnS-based AC powder EL device [2].

The classical phosphor materials, formed by either binary or ternary system, have been investigated over the years used for AC powder EL devices, as shown in Table 2-1.

**Table 2-1 ZnS-based phosphor materials used in AC powder EL devices**

| Phosphor | Emitting Colour | References |
|---|---|---|
| ZnS:Cu,Cl(Br, I) | Blue | [1,42] |
| ZnS:Cu,Cl(Al) | Green | [43] |
| ZnS:Mn,Cl(Br, I) | Yellow | [44] |
| ZnS:Mn,Cu,Cl | Yellow | [45] |
| ZnSSe:Cu,Cl | Yellow | [46] |
| ZnCdS:Mn,Cl(Cu) | Yellow | [1] |
| ZnCdS:Ag,Cl(Au) | Blue | [1] |

### 2.1.3 EL Characteristics of AC Powder EL Devices

The EL phenomenon is observed when an AC voltage of about 100~200 V is applied across the electrodes of an AC powder EL device, corresponding to an average electric field of order $10^4$ V/cm in the ZnS material. The luminance-voltage characteristics of a typical AC powder EL device are shown in Figure 2.4 [41]. The relation between the bias voltages and EL intensity can be evaluated by the following equation [47]:

$$L=L_0\exp\left[-\left(\frac{V_0}{V}\right)^{1/2}\right] \qquad (2-1)$$

where L is the luminance, V is the voltage, and $L_0$ and $V_0$ are constants which depend on the particle size of phosphor materials, the dielectric constant of the embedding medium and the device thickness. It has been established empirically that one of the key parameters affecting EL characteristics is the particle size, and a critical trade-off exists between EL efficiency and operational lifetime (defined by the time when the luminance becomes one

half of the initial value). The efficiency increases in proportion to $\sim d^{-1/2}$, where $d$ is the particle size, which produces the nonlinearity relationship of the luminance versus voltage. Operational lifetime, however, decreases in proportion to $\sim d$. Above a certain bias voltage, the probability for an electron to be accelerated to a given energy and excite subsequently the luminescent centers will increase sharply, corresponding to a rapid increase in the luminescent intensity. In addition, the luminance increases with AC frequency in the frequency region of ~100 Hz to 10 kHz. For example, a luminance of 100 cd/m$^2$ has been achieved for devices at a frequency of 400 Hz and a bias voltage of 200 V [41].

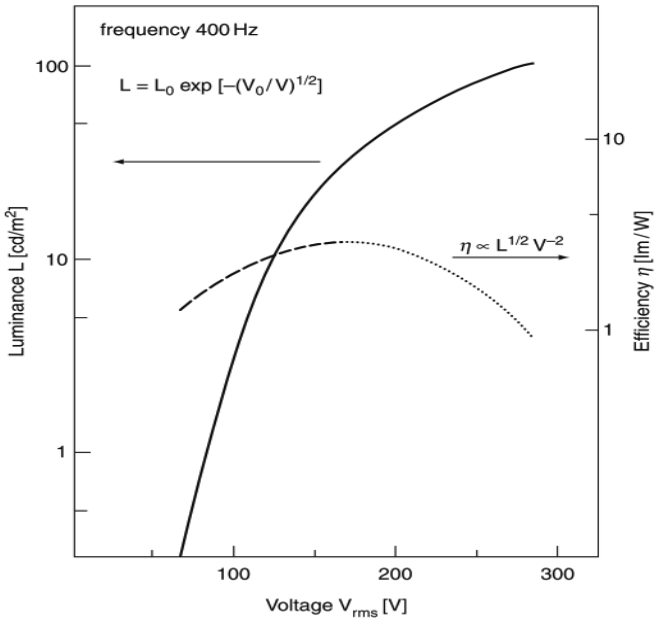


**Figure 2.4** Typical luminance-voltage and efficiency-voltage characteristics of AC powder EL device [41].

A typical voltage dependence of EL efficiency, $\eta$, is also shown in Figure 2.4. The value range of efficiency is 1 to 5 lm/W. The efficiency increases initially with increased

applied voltage up to a maximum value, but then decreased gradually with further increases in voltage. The EL efficiency dependence on the voltage V is expressed by [41]:

$$\eta = L^{1/2}V^{-2} \qquad (2-2)$$

where L is luminance intensity, V is the applied AC voltage. The maximum efficiency can be obtained at a voltage well below the highest luminance level.

### 2.1.4 Mechanism of Light Emission in AC Powder EL Devices

Many theories have been proposed to explain AC-excited EL of embedded ZnS-type phosphor powders, such as the impact ionization model, Zener emission model, and inverted impact ionization model. However, the explanation for AC powder EL is still open to speculation. Until now the most popular and reasonable theory has been the bipolar field-emission model, which was proposed by Fischer in 1963 [15]. Devices have been fabricated in many labs as well as by our lab recently [48] appear to be consistent with the bipolar field emission model. A careful study of the interior of ZnS:Cu,Cl phosphor particles was performed by using an optical microscope in Fischer's experiment. It was observed that the shape of the lighting-emitting region within a single phosphor particle profiles as double lines similar to twinkling tails of a comet upon application of an AC voltage, as described in Figure 2.5 [49,50].

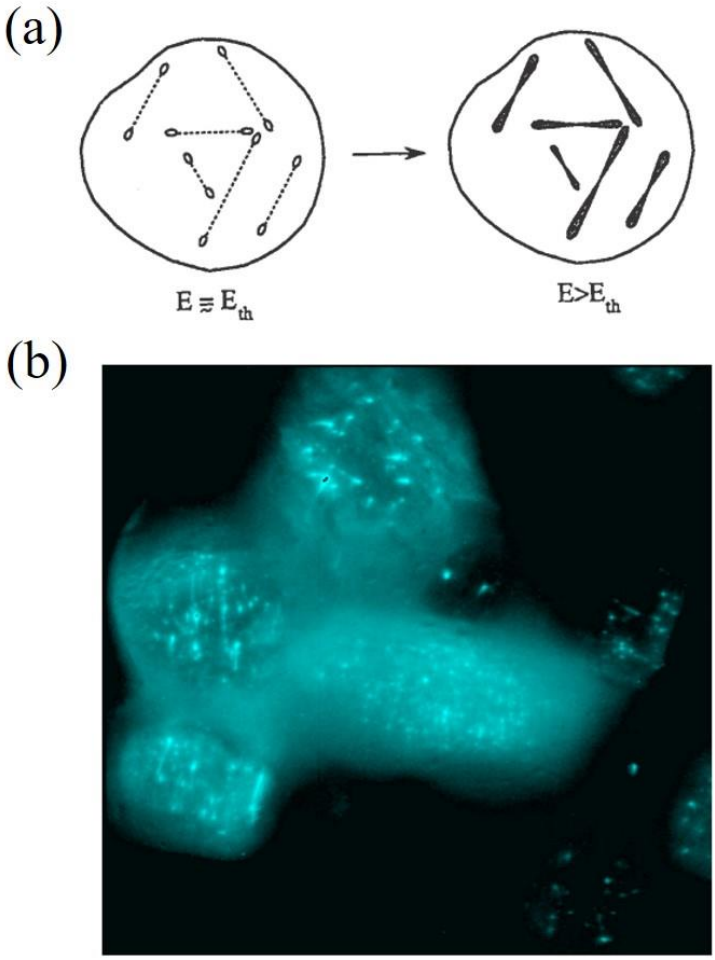


**Figure 2.5** Typical microscopic view of EL from a single ZnS:Cu,Cl particle. (a) Double lines at threshold voltage and above the threshold voltage are illustrated [49]. (b) Light microscopy image of EL emitted from ZnS:Cu,Cl particles under external electric field [50].

From the above observation, it is found that there are many dark segregations and precipitates inside the phosphor particles (Figure 2.6) [13].

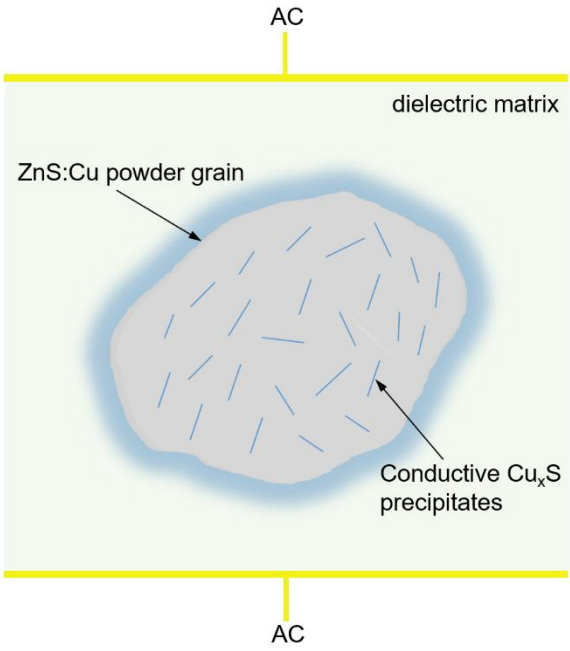


**Figure 2.6** ZnS:Cu,Cl phosphor particle containing dark segregations and light-emitting spots [13].

According to these observations, Fischer proposed the bipolar field-emission model, for the EL mechanism in the ZnS-type AC powder EL device. First, he believed that the dark segregations and precipitates inside the phosphor particles are $Cu_{2-x}S$. The ZnS phosphor powders are typically prepared by sintering at high temperature (1100~1200 °C) at which the hexagonal wurtzite phase predominates. When the powders cool, there is a phase transition from the wurtzite to the cubic zinc-blende structure. Copper preferentially precipitates on defects formed in the hexagonal-to-cubic transformation as a result of the reduction of their solubility in ZnS. The copper precipitates form thin $Cu_{2-x}S$ needles embedded in the ZnS crystal matrix (Figure 2.7(a)) [51]. $Cu_{2-x}S$ is known to be a p-type semiconductor with high conductivity. Between these $Cu_{2-x}S$ needles and ZnS powder, heterojunctions are formed (Figure 2.7(b)) [49].

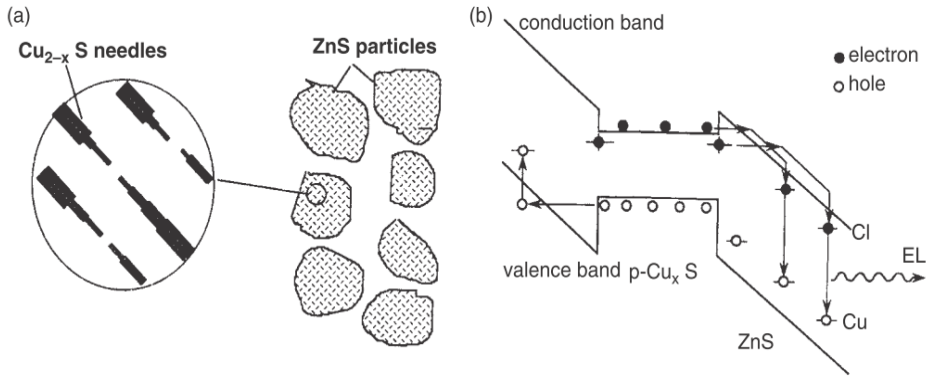


**Figure 2.7** EL emission mechanism and schematic energy-band diagram of powder EL device: (a) $Cu_{2-x}S$ precipitate needles embedded in the ZnS crystal matrix [51]. (b) Schematic energy-band diagram of ZnS-type AC powder EL device [49].

When an external electric field is applied to the phosphor particles, relatively high electric fields will be concentrated on the tip of the $Cu_{2-x}S$ needles (the effective tip radius is generally on the order of 100 nm) compared with that of other regions in the ZnS particles. Consequently, an applied field of $10^6$ -$10^7$ V/m can be amplified to a local field of $10^8$ V/m or more. This electric field is strong enough to induce tunneling of holes from one end of the needle and electrons from the other end into the ZnS:Cu,Cl lattice. The electrons are subsequently captured in nearby shallow traps inherent in Cl donor site, while the holes are trapped by the Cu recombination centers (acceptor sites). Eventually, a polarization field that opposes the applied field is formed nearby the tips of the $Cu_{2-x}S$ needles. When the AC field is reversed, injected electrons can combine with trapped holes (from the previous half cycle) at the recombination centers to produce EL each time when the field is reversed. Figure 2.8 shows the illustration of the basic principle of the bipolar field-emission model [15].

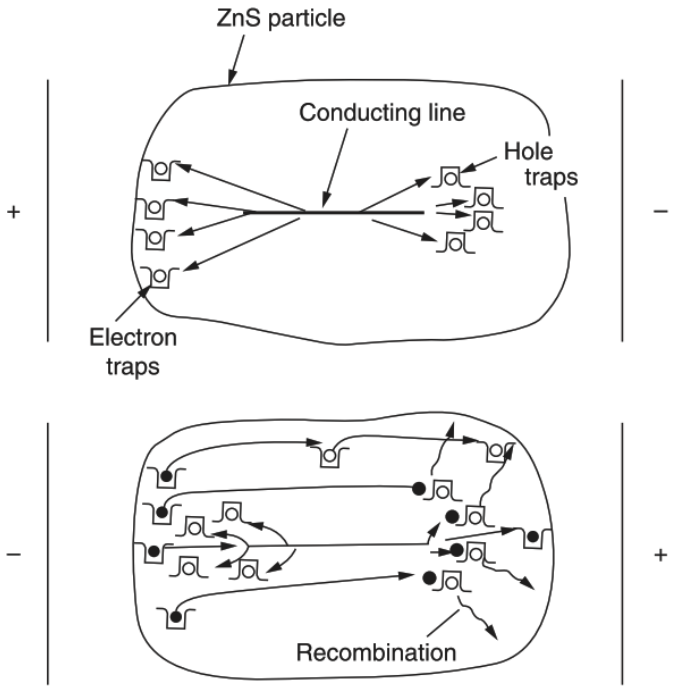


**Figure 2.8** Illustration of the basic principle of the bipolar field-emission model. Top: upon application of electric field, electrons and holes are ejected from the opposite ends of the conducting inclusion, where the field is intensified, into the ZnS lattice. Holes are trapped after a short path. Electrons can travel farther. Bottom: at field reversal, trapped electrons flow back to recombine with trapped holes (light emission). Other new electrons are field-emitted into the trapped holes, meanwhile, new holes are field-emitted at the other end of the conducting lines [15].

As a conclusion to the bipolar field-emission model, EL emission from a ZnS AC powder EL device is caused by the radiative recombination of electron-hole pairs through donor-acceptor pairs. The instantaneous field-emission current through the $Cu_{2-x}S$-ZnS heterojunction follows the Fowler-Nordheim equation:

$$I = A\frac{E^2}{W^{3/2}}\exp\left(-B\frac{W^{3/2}}{E}\right) \qquad (2-3)$$

where I is field-emission current, A and B are constants, E is the field strength and W is the work function. In this case, W corresponds to the energy difference between the electron affinity of ZnS and that of the conductive $Cu_{2-x}S$ precipitates.

It is worth noting that one of the necessary requirements for AC powder EL is that the conducting particles, such as $Cu_{2-x}$ S precipitates in ZnS EL phosphors, must have relatively sharp edges or tips. The electric field near the sharp edges of conducting materials, in the form of heterojunctions, is significantly higher than the average electric field far away from the sharp edges within the phosphor crystals. Therefore, the conductive sharp-pointed particles perform the same role as the conducting copper sulfide imperfection lines embedded in ordinary ZnS EL powders. When an electric field is applied to the phosphor powder, electrons will be ejected from the sharp tips of the conducting particles into the ZnS lattice and recombine with the holes which are trapped by luminescent centers to produce EL with the reversal of the electrical field.

Although the Fischer model is still widely accepted, a number of studies have been conducted in an attempt to confirm the existence of the postulated $Cu_2S$ phase and in turn the exact mechanism of AC powder EL. However, there has not been a definitive answer until now. For example, Ono [52] reported the detection of copper sulfide needles in the form of $Cu_2S$. Guo [53] observed a higher concentration of copper in the twin boundary areas and crystal streaks of sphalerite using high resolution transmission electron microscopy (HRTEM) and scanning electron microanalysis. Recent articles by Bridges and co-workers [50,54], maintained that copper sulfide is present in the form of tiny CuS-like clusters by means of extended X-ray absorption fine structure (EXAFS). They found that

during milling, the CuS precipitates were removed from the phosphor matrix by cleavage along the stacking planes. They also found that degradation and subsequent rejuvenation of AC powder EL emission was possible. Thermal treatment above 240 °C produced a significant degradation and change in spectral shape whereas below this temperature there was not a change, which indicated that two mechanisms were operative [21]. Fern and co-workers [55] found thermally quenched ZnS:Cu powder showed the Zn k-edge to be of reduced intensity because the electronic properties were modified. By using synchrotron radiation X-ray powder diffraction (XRPD) technique, they found that there was a large variation in crystallography of individual phosphor grains. Very recently, Silver reported that the alignment of the planar stacking faults of ZnS:Cu particles relative to the applied electric field is critical for light emission. Perpendicular alignment of the stacking faults results in no emission of light. As the alignment gradually approaches parallel, emission increases and reaches a maximum at parallel [56]. However, though others considered linear defects [57] and Fischer also considers copper sulfide defects [49], they found no direct evidence for copper sulfide needles. Therefore, the precise nature of the role of copper sulfide clusters and the charge generation process presently remain open to debate and conjecture. It is worth considering that typical Cu concentrations in AC powder EL phosphors are lower than ~ 0.1% due to the low solubility of Cu in ZnS crystal matrix. Thus, any $Cu_{2-x}S$ defects must be tiny, certainly too small to be observed in the 1960s and possibly challenging to be imaged even today. Fortunately, the very latest transmission microscopes have an angstrom-scale resolution and it might be valuable to check for such structures on well prepared samples.

### 2.1.5 Applications of AC Powder EL Devices

AC powder EL lamps and information displays historically suffer serious shortcomings, such as low luminance, short useful operating life, poor visibility in normal room light, and no visibility under high ambient light. What is worse, the high-voltage control circuit presented great obstacles, and operations at temperatures much above room temperature caused rapid deterioration of intensity of emitted light. In spite of this, AC powder EL features include low power consumption, uniform light emission over a large area, and an easy screen-print fabrication method, which allows for fabrication on a variety of substrates [57]. Over the last twenty years the extensive use of AC powder EL devices has included a wide range of modern technological applications, such as backlighting in both mobile phone keypads and liquid crystal displays, computer and television screens, watches, control panels, automotive and aeronautical instrument panels. Meanwhile, they are used in advertising billboards. AC powder EL devices with plastic cell structures provide great versatility in product design in terms of weight, compactness, robustness. In addition, AC powder EL devices can be produced to have extreme flexibility so that they can be folded, creased, and pierced while maintaining complete functionality. This allows design concepts previously unachievable to be available.

### 2.1.6 Present Limitation of AC Powder EL Devices

Lifetime and degradation represent a key issue for the application of AC powder EL devices. Lifetime is defined as the operating time over which the luminance decreases to one half of the initial value. Figure 2.9 shows a typical example of EL light output versus time [18]. The degradation rate depends on the driving conditions (such as frequency and luminance levels) and on the environmental conditions, especially on temperature and humidity. The luminance decay with time is usually expressed by:

$$L/L_0 = (1+at)^{-1} \qquad (2-4)$$

where $L_0$ is original luminance intensity, L is the measured intensity, t is time, a is a constant roughly proportional to the driving frequency [41]. Furthermore, it is very difficult to have both long lifetime and high luminance simultaneously for AC powder EL devices because they are trade-off characteristics.

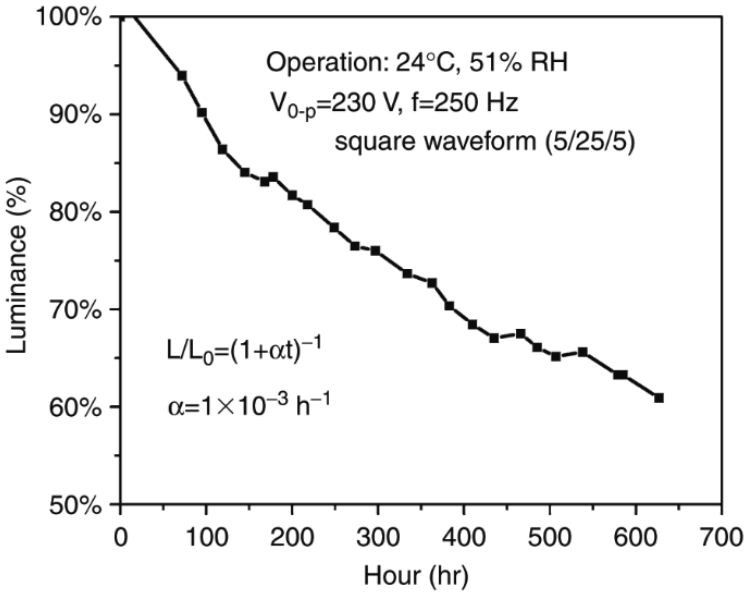


**Figure 2.9** Luminance maintenance curve of AC powder EL lamp at the operation conditions of V = 230V, f = 250 Hz [41].

According to the above bipolar field-emission model, the degradation is related to the diffusion of copper in the ZnS lattice with the help of the externally applied electric field. It is known that metals of group I (Ag and Cu) are fast-diffusion impurities in II-VI compounds [59]. The tips of the copper sulfide-decorated imperfection lines, which induce a highly localized electric field in the phosphor region, can be blunted by the diffusion of copper ions or by the attraction of copper ions from the adjacent host crystal under the influence of the high AC field. As operating time increases, copper sulfide lines become shorter and approach a final state which does not initiate sufficient electric field to excite luminescence. It has been experimentally confirmed that sulfur vacancies are one factor which accelerates EL deterioration, although the sulfur vacancy density is not increased by deterioration [60]. It implies that the sulfur vacancies assist copper diffusion in ZnS particles.

However, this explanation for the degradation in ZnS:Cu EL phosphor was recently challenged by Carter and co-workers [50] using extended X-ray absorption fine structure. According to their EXAFS results, the identification of $Cu_{2-x}S$ precipitates as CuS instead of $Cu_2S$ was made. It was suggested that the CuS precipitates, which have no electroluminescence themselves, are unchanged during the degradation of the device. In addition, isolated Cu ions, which were present as a solute in the ZnS lattice and formed along with CuS clusters during the phase transition upon cooling, trap electrons and work as highly effective recombination centers. Therefore, the degradation of the AC powder EL device is explained as the diffusion of isolated EL-active Cu ions to CuS clusters or the ZnS particle surface, resulting in the concentration of isolated Cu decreasing as EL degradation progresses. This explanation is quite possible because the degraded powder devices can be recovered under a heat treatment of relatively low temperature because of the low decomposition temperature for CuS in the ZnS crystal. The recovered luminance depends on the temperature and time of the heat treatment [21]. Consequently, the cause of powder EL degradation is far from fully understood and further research work is still needed. Regardless of which model is more likely to approach the real case, however, it can be concluded that the diffusion of Cu ions in and around $Cu_{2-x}S$ is substantially responsible for the loss of EL brightness. It has been experimentally proved that EL lamps operated at elevated temperature degrade much faster than those operated at low temperature, which is the most suggestive evidence that powder EL degradation is a diffusion-related phenomenon [18].

Another serious challenge for AC powder EL is that the ZnS-based host materials are sensitive to moisture and operating environment. The reaction shown below occurs between ZnS and water to produce $SO_2$.

$$ZnS + 2H_2O \rightarrow SO_2 + Zn + 2H_2 \qquad (2-5)$$

Through this reaction, sulfur escape from the ZnS phosphor particles, generating sulfur vacancies and zinc vacancies in the phosphor. It has been reported that the luminance of the ZnS phosphor deteriorates when the number of sulfur vacancies increases [60]. For this reason, two methods for preventing degradation have been developed. One method uses anti-humidity film, such as fluorocarbon film, to package the entire device. Another method is coating the phosphor particles themselves by transparent thin films with anti-humidity properties. However, both methods will increase the difficulty in device manufacturing process and consequent high-cost problem.

### 2.1.7 Measurement of EL Characteristics of AC Powder EL Devices

It is proved that the characteristics of AC powder EL devices, such as luminance, threshold voltage, luminous efficiency, color coordinates and lifetime, significantly depend on the measuring conditions and driving source form, i.e. drive voltage, drive waveforms and drive frequency. Therefore, building up general and standard measuring conditions is highly desirable for comparing of the values of EL characteristics from different AC powder EL devices. In the following the suggested standard measuring and evaluation methods of AC powder EL devices are discussed in detail. These methods could also be

properly extended to measurement and analysis of EL characteristics of other EL devices, such as DC powder EL devices, AC thin-film EL devices, and DC thin-film EL devices.

(1) Luminance L and Threshold Voltage $V_{th}$

The AC driving wave forms are usually sinusoidal waves and square pulse waves of alternating polarity with frequencies of 50 or 60 Hz, or 1 kHz. The luminance of AC powder EL devices depends on peak voltage values, the values of the applied AC voltage should be indicated in peak-to-peak voltage values ($V_{pp}$) rather than in root-mean-square (rms) values. When an AC driving wave form is imposed on an EL device, light is emitted from the EL device and is characterized by luminance. Here luminance is a photometric term indicating the radiated power in terms of human eye sensitivity, i.e. a physical measure of luminous intensity per unit area, in units of cd/m$^2$. Occasionally, another unit of luminance shown in some literatures is the foot-Lambert (fL) defined by [52]:

$$1\,fL = \frac{1}{\pi} \times \frac{cd}{(ft)^2} = 3.426 cd/m^2 \qquad (2-6)$$

The threshold voltage $V_{th}$ is defined as the applied voltage corresponding to the luminance of EL device of 1 cd/m$^2$. Alternatively, there is another way of defining the threshold voltage of EL devices, which is based on the charge vs. voltage (Q-V) curve plotted by using the Sawyer-Tower circuit [2,52]. Figure 2.10 shows a typical Q-V curve of AC powder EL devices. The shape of the Q-V curve is characterized as a loop monitored by an oscilloscope. For a set of different applied voltages, the Q-V loops as well as the device luminance in unit of cd/m$^2$ are recorded. The loop becomes larger with increasing applied voltage due to more charge being driven through the phosphor layer by each voltage cycle. It is experimentally determined that the luminance of an EL device is largely

proportional to the amount of charge per unit area (or charge density) that flows across the phosphor layer during each AC voltage pulse, and to the frequency of these pulses [2]. Because luminance depends substantially on the drive frequency and drive wave forms, the frequency and drive wave form of the applied AC electrical cycle should be specified when luminance values are measured.

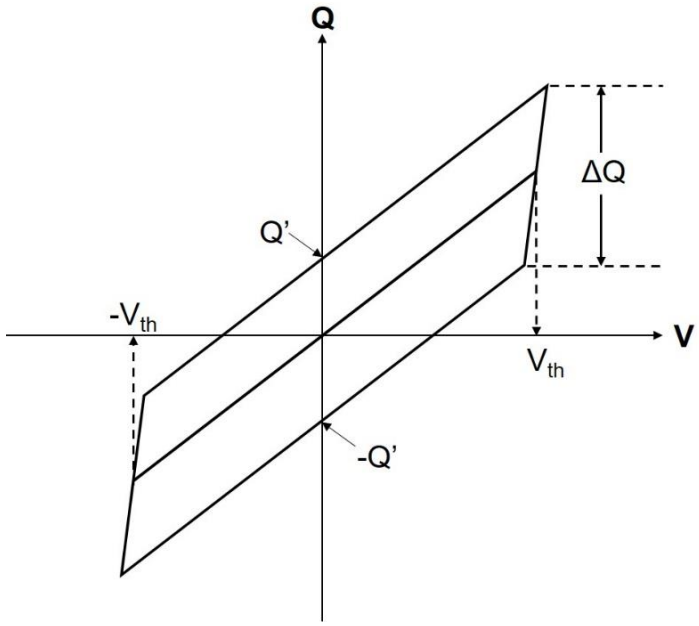


**Figure 2.10** Sawyer-Tower output trace showing the charge vs. applied voltage (Q-V) relationship for an EL device. $V_{th}$ is the threshold voltage of the EL device; $Q_{th}$ is the threshold charge; $\Delta Q$ is the transferred charge; Q' is the remaining charge in the EL device when applied voltage is zero [52].

(2) Luminous Efficiency η

The area encompassed within the above Q-V diagram (Figure 2.10) gives the energy density delivered to an EL device per cycle, $E_{in}$, i.e., input power density per cycle. Therefore, the $E_{in}$ multiplied by the frequency *f* of the applied AC driving wave is equal to the electrical power density, $P_{in}$, dissipated in an EL device, which can be expressed by [2]:

$$P_{in} = f \times E_{in} = 4 \times f \times V_{th} \times Q' \quad (2-7)$$

where $V_{th}$ is the threshold voltage of the EL device, and Q' is the remaining charge density in the EL device when the applied voltage is set to 0 V. When a Q-V loop is not approximated by a parallelogram shape, $P_{in}$ must be evaluated numerically, for example, counting the loop area from the grids of an oscilloscope monitor.

After obtaining the input power density $P_{in}$ [$W/m^2$] and luminance L [$cd/m^2$] values, the luminous efficiency η [lm/W] can be calculated by [52]:

$$\eta[lm/W] = \pi \times \frac{L[cd/m^2]}{P_{in}[W/m^2]} \quad (2-8)$$

(3) Chromaticity

Chromaticity indicates the quality of a color form an emitting light regardless of its luminance. The physical perception of color is based upon three RGB monochromatic components. The Commission Internationale de l'Eclariage (CIE) 1931 has defined a standard of chromaticity coordinates which represents the attributes of color by a three-dimensional diagram. The Cartesian coordinates of this tridimensional diagram are derived from spectral tristimulus values, $\bar{x}(\lambda)$, $\bar{y}(\lambda)$ and $\bar{z}(\lambda)$ [52], as shown in Figure 2.11. The $\bar{y}(\lambda)$ curve is intentionally chosen to be identical to the luminous-efficiency function of human eyes, which is normalized at a peak at 550 nm.

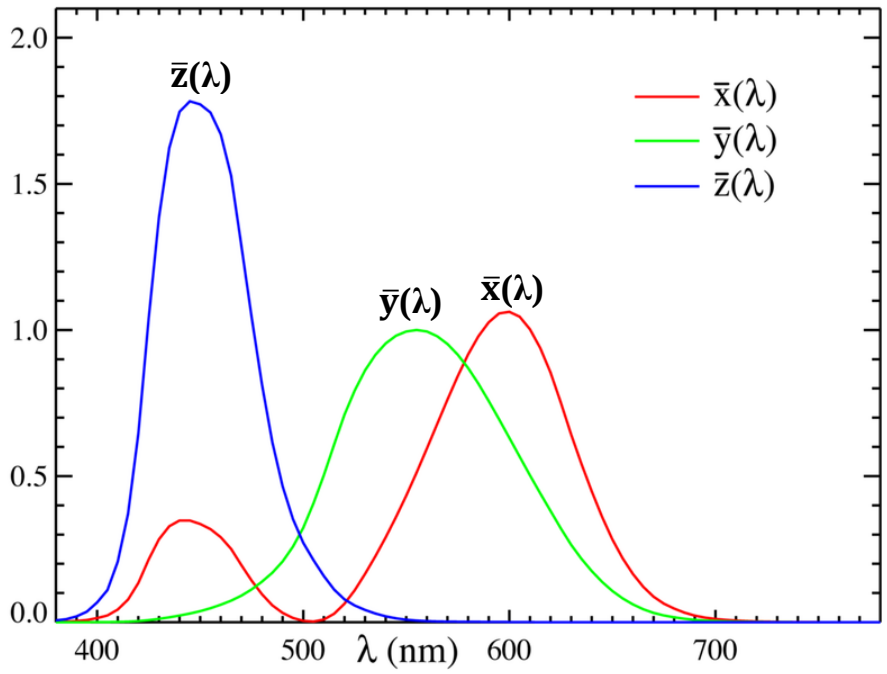


**Figure 2.11** CIE 1931 standard color mixture curves for $\bar{x}(\lambda)$, $\bar{y}(\lambda)$ and $\bar{z}(\lambda)$ [52].

The CIE coordinates, x, y, and z are defined by the ratios:

$$x = \frac{X}{X+Y+Z}$$

$$y = \frac{Y}{X+Y+Z}$$

$$z = \frac{Z}{X+Y+Z} \qquad (2-9)$$

where X, Y and Z are calculated by the following integrations over the entire spectrum of visible light:

$$X = \int \phi(\lambda)\bar{x}(\lambda)d\lambda$$

$$Y = \int \phi(\lambda)\bar{y}(\lambda)d\lambda$$

$$Z = \int \phi(\lambda)\bar{z}(\lambda)d\lambda \qquad (2-10)$$

where $\phi(\lambda)$ is spectral radiance of EL emission, which is bounded to ensure the values of X, Y, and Z are bounded. $\lambda$ is the wavelength of the visible light, and the standard limits of the integral are $\lambda \in$ (380 nm, 780 nm).

Since the sum of x, y and z is unity (x+y+z=1), it is sufficient to identify only x and y values to calculate the z value. That is, the CIE color diagram can be expressed as a two-dimensional projection into the xy plane. Figure 2.12 shows a standard CIE chromaticity diagram [61]. In the diagram, the upper arc is the locus of saturated colors, and the central region appears white. All the colors that the human eye can distinguish are enclosed in the area between the arc of saturated colors and the bottom straight contour lines, which is labelled as magenta. A black body locus is shown as the $T_c(k)$ curve, which indicates the change of whiteness with different blackbody temperatures. The color varies from deep red to bluish white with increasing temperature.

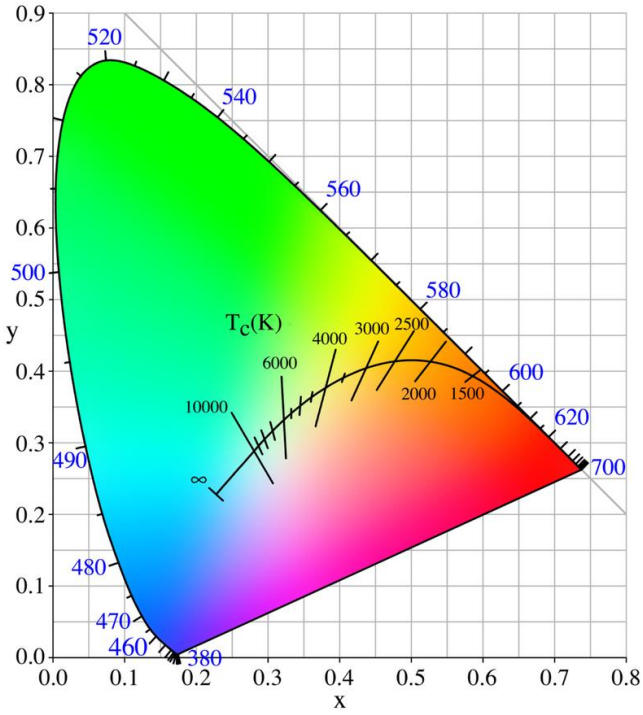


**Figure 2.12** CIE 1931 chromaticity diagram with regions of three primary colors [61].

## 2.2 Phosphor Materials for AC Powder EL Devices

### 2.2.1 Basic Principle of Phosphor Materials

The word ‘phosphor’ comes from the Greek language and means ‘light bearer’, to describe light-emitting or luminescent materials [41]. Typically, phosphor materials are composed of a transparent microcrystalline host (or a matrix) and a luminescence center (or an activator) [41,52]. The host material is responsible for the electrical and optical properties of the phosphor. The luminescence center controls the emission spectra of luminescence. In most phosphors, the luminescence center is formed by intentionally incorporated impurity atoms to the host material in small quantities. It provides distinct

energy levels in the energy gap between the conduction and valence bands of the host material. The interaction of the incident energy source with a luminescent material is critical for the generation of light. For example, pure stoichiometric ZnS does not show electroluminescence characteristics. Luminescence can be caused by introduction of lattice defects, by deviation of stoichiometric ratio of Zn-S, and by addition of controlled amounts of specific impurities (dopants). Generally, when dopant atoms are introduced, defects and stoichiometric deviation are simultaneously produced, either through the rearrangement of crystal lattice or through the physical and chemical processing conditions under which dopant is added. Typical examples of dopant atoms (luminescence centers) are Mn and Cu. Other dopants leading to the reduction of EL intensity are termed as 'killers' or 'quenchers'. For example, Co, Fe, and Ni are well-known quenchers in EL powder phosphors.

As a host material, several requirements must be satisfied to achieve efficient luminescence. Firstly, the band gap of the host material must be larger than the energy of the photons generated from the doped luminescent centers in order to prevent the emitted visible light being absorbed by the host material. Secondly, host material must stand a high electric field of the order of $10^8$ V/m without dielectric breakdown owing to the field emission mechanism. Finally, the host materials must be capable to provide a medium for the efficient transport of high energy (>2 eV) electrons [47].

On the other hand, emission light color or wavelength is determined by the radiative relaxation of the luminescence center, whereas the relaxation process of the luminescence center is determined by the quantum mechanical properties itself through either inter-shell or intra-shell electronic transitions following selection rules. In other words, the light

emission is caused by the atomic transition within the luminescence center of phosphor. Specifically, in an atom, the energy states of an electron, known as a Fermion, are characterized by four quantum numbers, indicating as the principal quantum number *n*, angular momentum number *l*, magnetic quantum number $m_l$, and spin quantum number *s*, individually. Electronic transitions that involve a change of principal quantum *n* are called inter-shell transitions, while those that occur without involving a change of *n* are called intra-shell transitions. Electronic transitions are driven by an electric dipole moment and the transition moment integral is defined as [47]:

$$M = \int \Psi' \hat{T} \Psi d\tau \qquad (2-11)$$

where $\Psi'$ is the excited (final) state wavefunction, $\Psi$ is the ground (initial) state wavefunction, $\hat{T}$ is the dipole moment operator, and integration $\int d\tau$ is performed over all space. The total wavefunction $\Psi$ can be expressed as:

$$\Psi = \Psi_e \Psi_s \Psi_v \qquad (2-12)$$

where $\Psi_e$ is the electronic orbital wavefunction, $\Psi_s$ is the electron spin wavefunction and $\Psi_v$ is the nuclear vibrational wavefunction. Therefore, the above transition moment integral can be expressed as:

$$M = \int \Psi'_e \hat{T} \Psi_e d\tau \int \Psi'^{*}_s \hat{T} \Psi_s d\tau \int \Psi'^{*}_v \hat{T} \Psi_v d\tau \qquad (2-13)$$

The intensity of a transition, or the intensity of light absorption, is related to the transition moment integral by a term called oscillator strength, which characterizes the dipole moment of an electronic transition. The oscillator strength is defined as [47]:

$$F = \left( \frac{8\pi^2 m_e \nu}{3he} \right) * M^2 \qquad (2-14)$$

where M is the aforementioned transition moment integral, $m_e$ is mass of an electron, $\nu$ is oscillation frequency, $h$ is the Planck constant, and $e$ is charge of an electron. If any of the integrals in equation 2-13 is zero, M and F are zero. It means that this transition is forbidden. Selection rules are derived and set for the transition which $M \neq 0$.

Consequently, the first selection rule is called the Laporte selection rule, which is based on the premise that the transition moment is an intrinsic property of the atom or ion so that it should not change by the application of a symmetry operation. For example, if the dipole moment operator $\hat{T}$ is odd, the sign of the first integral part of equation 2-13, $\int \Psi'_e \hat{T} \Psi_e d\tau$, will change associated with inversion. It implies that there is a corresponding negative value for each positive value in the transition moment function, and thus the transition moment integral over all space M is zero which results in no absorption (or emission) of radiation because no any electron transition is allowed. From this perspective, the production $\Psi'_e \hat{T} \Psi_e$ must be even as a whole integral $M \neq 0$. Because the dipole moment operator is an odd function, either the wavefuntion of the initial state or the final state must be even and the other wavefunction must be odd to ensure the entire production is even. The result driven from this requirement is the so-called Laporte selection rule which can be expressed by [47]:

$$\triangle l = \pm 1 \qquad (2-15)$$

where $\triangle l$ is the change in the angular momentum quantum number. To make sure an electronic transition to be allowed, the angular momentum quantum number must change

by factor of 1. Therefore, the Laporte selection rule demonstrates that intra-shell transitions, i.e. d-d, f-f, are forbidden but some inter-shell transitions such as s-p, p-d, d-f, are allowed and consequently the absorption or emission of photon radiation are observed.

The second selection rule for electron transition is called the spin selection rule. Inspection of equation 2-13 reveals that the second integral part $\int \Psi'_s{}^* \hat{T} \Psi_s d\tau$ must have a nonzero value if an electron transition is to be allowed ($M \neq 0$). Owing to the orthogonality of the spin wavefunction, the integral part $\int \Psi'_s{}^* \hat{T} \Psi_s d\tau$ is zero if $\Psi'_s \neq \Psi_s$. Therefore, a transition occurs only if the initial and final spin states of the electron involved are identical. The spin selection rule results from the fact that there is no spin associated with a photon, which could be summarized as [47]:

$$\Delta s = 0 \qquad (2-16)$$

where *s* is the spin quantum number of an electron. According to the spin selection rule, for example, singlet-singlet and doublet-doublet transitions are allowed but singlet-triplet and quartet-doublet transitions are forbidden.

These selection rules are general and can be applied to all optical transitions theoretically, however, there are several conditions that relax them. For example, Laporte selection rule can be relaxed when the luminescent center is placed in a lattice site without a center of symmetry (site with uneven crystal field components, i.e. tetrahedral). This relaxation of the selection rule is important to AC powder EL device, such as green EL phosphors (i.e., ZnS:Cu,Al) is Laporte forbidden because the luminescence center ions locate at the tetrahedral sites of ZnS host lattice [47].

The luminescence of phosphor materials can be excited by many types of energy. For example, in cathodoluminescence, the phosphor is excited by a beam of energetic electrons. In photoluminescence the phosphor is excited by electromagnetic radiation, usually by ultraviolet illumination, and in EL by an electric voltage or injection current, X-ray luminescence involves X-ray excitation, chemiluminescence depends on the energy of a chemical reaction, triboluminescence depends on mechanical energy, and so on [47,62]. Particularly, the light emission generated in EL behaviour in phosphor materials generally involves the injection of charge carriers into the phosphor lattice, excitation of luminescence centers by energetic charge carriers (impact excitation), and radiative relaxation of luminescent centers. In general, the luminescent center can be raised to its excited state when the electrical energy is applied to the phosphor material. The luminescent center eventually relaxes to its ground state by dissipating the absorbed electrical energy. The relaxation process may be accomplished by: (i) emitting photons (radiative relaxation), (ii) emitting phonons to the host lattice of phosphor (nonradioactive relaxation), (iii) transferring energy to other luminescent centers. In order to achieve high efficiency in phosphor materials, the nonradioactive process is necessary to be suppressed.

### 2.2.2 Development of Phosphor Materials in AC Powder EL Devices

#### 2.2.2.1 Sulfide-Based EL Phosphor Materials

Most phosphor material for AC powder EL research has been focused around sulfide-based phosphors and by far the most important EL powder is zinc sulfide (ZnS). Typically, ZnS is a semiconductor material and exists in two main structural modifications, the low

temperature form which is cubic zinc blende with band-gap energy of 3.7 eV, and the high temperature form which is hexagonal wurtzite with band-gap energy of 3.8 eV [63]. In either phase, each $Zn^{2+}$ ion is coordinated by four $S^{2-}$ions in a tetrahedral configuration. Because of its excellent electrical properties such as the large band-gap energy, direct recombination and low leakage current, ZnS is ideal for being used as phosphor material by doping with transition metals or rare-earth metals [64,65]. Furthermore, owing to the advantage of the simple manufacturing process, the convenience of being able to print large areas while maintaining high power efficiency, ZnS phosphor powders were suitable for back lighting of liquid crystal panels or for flat panel displays before the maturation of LEDs [66]. Typically, ZnS-based phosphors can emit different color light by tuning the doping elements (or luminescence centers), as shown in Table 2−1. Luminescence centers in these phosphor materials are formed by deep donors or deep acceptors, or by their associations at the nearest-neighbour sites. For example, the energy levels of ZnS:Cu,Al are shown in Figure 2.13 [67].

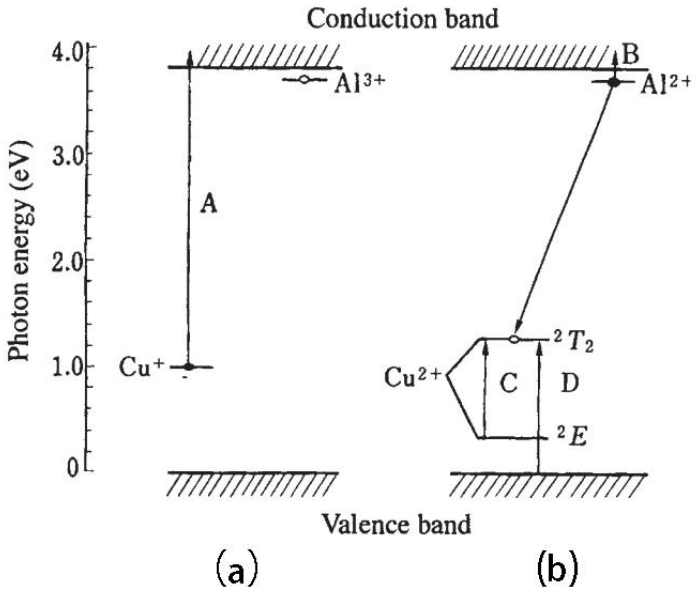


**Figure 2.13** Energy levels and absorption transition of ZnS:Cu,Al phosphor before excitation (a) and during excitation (b) [67].

As shown in Figure 2.13, before excitation, a Cu ion (the acceptor) is monovalent (1+), while an Al ion (the donor) is trivalent (3+), so that charge compensation is realized when they substitute the sites of $Zn^{2+}$ ions in the lattice. This is quite reasonable since Cu and Al ions are doped with nearly the same concentrations and they are providing charge-compensation for each other. There exits an absorption band due to the transition of an electron from the copper acceptor level to the conduction band, as shown by the arrow A in this figure. It shows the characteristic excitation band of the center. When excited, a hole is trapped by $Cu^{+}$ ions and an electron is trapped $Al^{3+}$ ions, resulting in both Cu and Al ions becoming divalent (2+). Simultaneously, the levels of $Cu^{2+}$ ($3d^9$ configuration) are split by the crystal field into $^2T_2$ and $^2E$ states, with $^2T_2$ lying higher in the cubic zinc-blende structure. In the process of the relaxation due to the reversal of the applied electric field, the electron trapped by the $Al^{2+}$ ion will recombine with the hole trapped by $Cu^{2+}$ and

luminescence is produced. As a result, Cu and Al ions recover to monovalent and trivalent again, respectively.

The emission spectra of ZnS-based EL phosphor materials are shown in Figure 2.14 [41]. Emission colors depend on the specific luminescent centers incorporated in the phosphors. When the ZnS lattice is activated with Cu (activators) and Cl, I, and Al (co-activators), donor-acceptor pairs are formed. As mentioned above, the EL is produced by the radiative recombination of electron-hole pairs at donor-acceptor pair sites. The combination of Cu and Al in ZnS:Cu,Al phosphor generates green (~550 nm) emission color. The combination of Cu and Cl in ZnS:Cu,Cl phosphor produces blue (~460 nm) and green emission bands. The relative intensities depend on the relative amount of Cu to Cl. ZnS:Cu,I shows a blue emission. It should be noticed that ZnS:Cu in which no co-activators are incorporated shows a red emission. By further incorporating $Mn^{2+}$ ions into ZnS:Cu,Cl phosphor material, the resultant ZnS:Cu,Mn,Cl shows a yellow emission (~ 580 nm) due to the intra-shell transition of $Mn^{2+}$ ions.

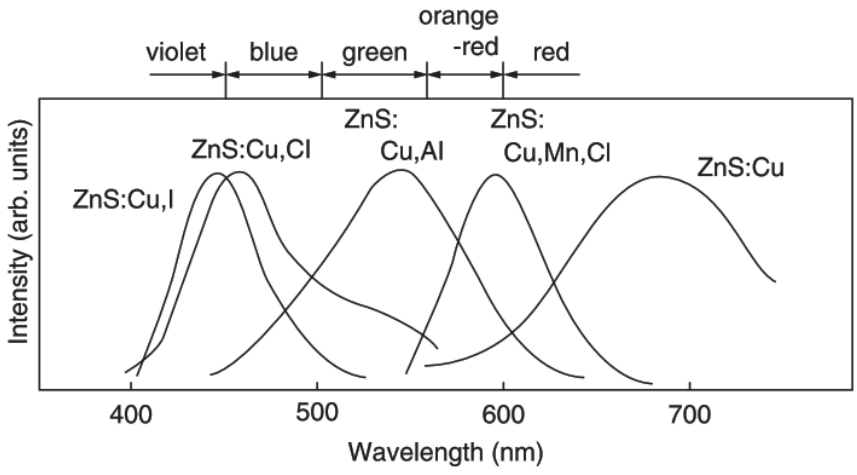


**Figure 2.14** The emission spectra of ZnS-based EL phosphor materials [41].

#### 2.2.2.2 Oxide-Based EL Phosphor Materials

Although ZnS-based phosphors exhibit excellent EL as mentioned above, the intrinsic problems such as chemical instability and sensitivity to moisture make them difficult to pattern on substrates by chemical etching or photolithography techniques. As an alternative to sulfide-based phosphors, oxide-based phosphors were not traditionally considered as promising candidates for ACPEL phosphor host materials at the early age of the development of EL phosphor powders. Their band gaps (> 4 eV) were considered too large for transporting significant current densities of hot electrons (> 2 eV). Meanwhile, oxide-based phosphor materials do not crystallize as readily as sulfide-based phosphors. However, compared to sulfide-based phosphors, oxide-based phosphors have inherent insensitivity to moisture and excellent chemical stability. The manufacture of oxides is often relatively simple and safe.

$Zn_2SiO_4$ as a host material for oxide-based phosphors has attracted much attention in application of fluorescent lamps, field emission displays and plasma display panels [68-71]. It is worth noting that the blue emission of $Zn_2SiO_4$ phosphor doped with Ti, Ce and Tm is one of the first reported oxide blue phosphors in EL devices. The blue emission from $Zn_2SiO_4$:Ti exhibited a peak centered at a wavelength of about 420 nm. In 1991, Minami [68] reported that a bright green emission was achieved in EL device consisting of $Zn_2SiO_4$:Mn oxide phosphor. A luminance of 90 cd/m$^2$ and a maximum luminous efficiency of 0.3 lm/W were obtained under an applied voltage of 400 V at 60 Hz. and the maximum luminance is 16 cd/m$^2$ driven by a sinusoidal wave at 1 kHz [70]. Although $Zn_2SiO_4$:Mn shows promising properties for EL devices, one disadvantage is the high post

annealing temperature required to crystallize the phosphor host material and to activate the luminescent center. In order to decrease the post annealing temperature, a flux such as LiF was introduced into the $Zn_2SiO_4$:Mn thin film phosphor material. It was postulated that point defects introduced by Li and F ions permit charge compensation while lowering the crystallization temperature. The crystallization was achieved at 660~700 °C for 1 hour, however, the luminance was less than 50 cd/$m^2$ driven by a square wave pulse at 60 Hz [71].

A greatly improved oxide green emission phosphor was reported by Kitai's group when low crystallization temperature was achieved in $Zn_2Si_{1-x}Ge_xO_4$:Mn material system [72,73]. As shown in Table 2-2, the properties of $Zn_2SiO_4$ and $Zn_2GeO_4$ are quite similar, but the crystallization temperature of $Zn_2GeO_4$ is about 300 °C lower than that of $Zn_2SiO_4$.

**Table 2-2 Properties of $Zn_2SiO_4$ and $Zn_2GeO_4$ host materials for EL phosphors** [73]

| | $Zn_2SiO_4$ | $Zn_2GeO_4$ |
|---|---|---|
| Crystal structure | Rhombohedral | Rhombohedral |
| Lattice constants (angstrom, Å) | a=13.94, c=9.31 | a=14.23, c=9.53 |
| Melting point (°C) | 1512 | 1490 |
| Dielectric constant | 9.5-10.5 | 14.7 |
| Crystallization temperature (°C) | 900-1000 | 650-700 |
| Theoretical density (g/$cm^3$) | 4.24 | 4.82 |
| Refractive index | 1.69 | 1.80 |
| Band gap (eV) | 5.5 | 4.7 |
| Peak wavelength (nm, 2 at% $Mn^{2+}$) | 528 | 535 |

#### 2.2.2.3 $Zn_2GeO_4$:Mn EL Phosphor Material

Zinc germanate ($Zn_2GeO_4$) has been evaluated as a potential phosphor in alternating current thin-film electroluminescent displays [30]. In this phosphor, Ge atoms substitute for the Si atoms from $Zn_2SiO_4$. The resulting composition, $Zn_2GeO_4$, possesses a lower crystallization temperature and smaller bandgap. Crystallization temperature as low as 650 °C have been reported. A slight raise in processing temperature to 810 °C could improve the luminance of the phosphor in application of AC powder EL devices. The EL emission peak, ~540 nm, of $Zn_2GeO_4$:Mn has been characterized as having a short decay time (100 microseconds), resulting from the formation of a perfect crystal structure and the low coordination number (4) of manganese ions in the host lattice. The dopant Mn as a $Mn^{2+}$ ion substitutes effectively for $Zn^{2+}$ ions. This is achieved since both $Zn^{2+}$ and $Mn^{2+}$ are 2+ ions and have similar ionic radii (0.74 nm for $Zn^{2+}$, 0.8 nm for $Mn^{2+}$) to bond in a tetrahedral configuration. Mn, being a transition metal, has an unfilled inner-shell or 3d shell, which gives rise to a ground state as well as an excited state.

Nevertheless, it is important to note that the details about nanowire-based light generation in $Zn_2GeO_4$:Mn AC powder EL device have not been definitely figured out yet. Our lab did a meaningful exploration in which SiC whiskers were mixed into $Zn_2GeO_4$:Mn powders so that a green light could emit nearby SiC whiskers under applied AC voltage [48]. The result is consistent with electron emission from the shape-edged SiC whiskers to the phosphors matrix causing light emission. It further indicates that electron emission from SiC whiskers is the primary mechanism for light emission. If a sample is made without SiC whiskers no light emission is observed when an AC voltage is applied. Another possible

way that light emission may be occurring in nanowire-based $Zn_2GeO_4$:Mn AC powder EL devices is through an impact ionization mechanism. In this circumstance, the electrons being emitted from the conducting nanowires may be 'hot' and therefore able to impact-excite $Mn^{2+}$ in the phosphor producing green light emission.

In addition, there may be a more complicated mechanism involving a charge transfer process: electrons emitted from the conducting nanowires may be trapped in charge traps, such as cation vacancies in the phosphor crystal, possibly due to the formation of metastable $Mn^{4+}$, and valence states of Ge ions other than 4+, and then may form space charge in the phosphor. For example, if the trap is a $Mn^{2+}$ ion that becomes a $Mn^{1+}$ as a result of electron trapping, it is possible that the subsequent valence states transition from 1+ to 2+ of the Mn ion could cause a light emission event as the electron is released. This electron release would likely occur during the inversion of the external AC field. Alternatively, a $Mn^{3+}$ ion could be acting as an electron trap causing the Mn ion to return to a $Mn^{2+}$ excitation state and subsequently to a $Mn^{2+}$ ground state. Consequently, more detailed investigation is required to find out the dominant excitation mechanism in the nanowire-based $Zn_2GeO_4$:Mn AC powder EL device.

# Chapter 3. Methodology for Synthesis, Modelling and Characterization

## 3.1 Introduction of Nanowire Synthesis

According to the bipolar emission mechanism in AC powder EL device (see Section 2.1.4), the conducting $Cu_{2-x}S$ precipitates with relatively sharp edges play a critical role in initiating EL phenomenon. The electric field near the sharp tips of the conducting precipitates in the phosphor is considerably higher than the average electric field of other regions, approximately 100 times enhanced. Unfortunately, there are no conducting needles that precipitate from $Zn_2GeO_4$:Mn phosphor material when we attempt to take advantage of the excellent luminance efficiency of this material. In this project, conducting zinc oxide (ZnO) or copper oxide (CuO) nanowires with sharp tips are introduced to $Zn_2GeO_4$:Mn phosphor, forming nanoscale heterojunction structures at the contact areas with the phosphor. Through the heterojunction structures, ZnO and CuO nanowires are expected to perform the same role as the conducting $Cu_{2-x}S$ precipitations embedded in ZnS EL powders.

### 3.1.1 Introduction of ZnO Nanowire Synthesis

Recently, nanomaterials have attracted tremendous interest because of their outstanding performance in electronics, optics, and photonics. Nanomaterials are usually classified into three categories based on their dimensions: zero-dimensional (0D), one-dimensional (1D),

and two-dimensional (2D) nanomateiral. 0D nanoarchitectures known as quantum dots or nanoparticles with an aspect ratio near unity, have been widely used in displays, solar cells, catalysts and biological applications [74-93]. 2D nanostructures, such as thin-film structure, have also been extensively used as biosensors, optical coatings, photonic devices, and energy storage [94-114]. 1D nanomaterials, especially 1D semiconductor nanostructures such as nanowires, nanorods, nanotubes, nanofibers, and nanowhiskers have been the subject of intense interest in both academic research and industrial applications due to their potential as both interconnects and functional building blocks for fabrication of electronic, photoelectronic, electromechanical, and electrochemical nanodevices [115-151]. Among 1D semiconductor nanomaterials, zinc oxide (ZnO) nanowire is one of the most important nanomaterials for functional nanodevices in today's research community [134-140].

ZnO is a direct wide band-gap (3.37eV) semiconductor with a large exciton binding energy (60 meV at room temperature), making it an important semiconductor for optoelectronics [135,138-140]. ZnO is transparent to visible light and can be made highly conductive by doping. ZnO structures have two different crystalline forms: hexagonal wurtzite and cubic zinc-blend form. Under common conditions, ZnO exhibits a hexagonal wurtzite structure with $a$ = 0.32498 nm, $b$ = 0.32498 nm, and $c$ = 5.2066 nm. The ratio of $c/a$ of about 1.60 is close to the ideal value for a hexagonal cell $c/a$ = 1.633 [138-140]. The ZnO crystalline structure could be described as alternating planes consisted of tetrahedrally coordinated $O^{2-}$ and $Zn^{2+}$ stacked along the $c$-axis (Figure 3.1). Nanowire-like ZnO materials are the ideal system for studying the transport process in one-dimensional objects, which are of benefit not only for understanding the fundamental phenomena in low

dimensional nanomaterials but also for developing new generation nanodevices with excellent performance. Since the successful growth of aligned ZnO nanowires on a single-crystal substrate [116,152,153], a system that may be very useful for vertical device fabrication has been discovered. As a result, substantial effort has been devoted to acquire more control over alignments, including supporting substrates, distribution of nanowires, and density of nanowires, to maximally meet the application requirement of nanodevices.

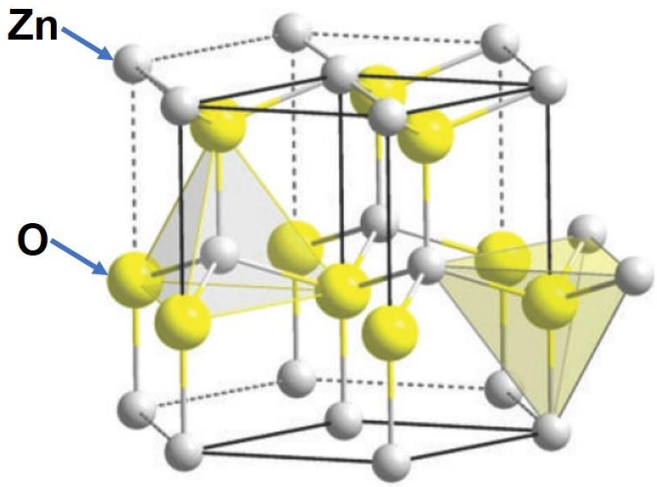


**Figure 3.1** The wurtzite crystalline structure of ZnO [138].

To fabricate vertically aligned ZnO nanowires, three main techniques were usually used so far. The first technique is based on the well-known vapor-liquid-solid (VLS) growth mechanism, in which gold nanoparticles were used as the catalyst to direct the nanowire growth. *a*-plane sapphire which has perfect lattice matchup with ZnO *c* plane was usually used as the growth substrates, and the growth was carried out at relatively high temperature of 850−1000 °C [116,154-156]. The VLS process has been the most widely used technique for growth of ZnO nanowires because of its relatively low cost and simple procedure. The

second technique is metal-organic chemical vapor deposition (MOCVD), in which metal-organic zinc precursor (e.g. diethyl zinc, $Et_2Zn$) was used as the zinc source and aligned ZnO nanowires were epitaxially grown on sapphire substrates (or silicon wafers) at 400−500 °C in a low-pressure MOCVD system [157-159]. The third technique is based on a solution phase synthesis method, in which ZnO nanocrystals (5−10 nm in diameter) were coated on a substrate (e.g., silicon wafer) to act as the seed layer followed by hydrothermal ZnO growth in an aqueous solution of zinc nitrate hydrate at 90 °C [160-162]. The solution process is favored for its very low cost and the ease of scale-up but has low crystalline quality compared with the VLS- and MOCVD-grown ZnO nanowires. It worth noting that most electrical and optical applications of ZnO nanowires prepared by the above-mentioned methods remain constrained by the expensive substrates (such as sapphire). In addition, the density of ZnO nanowires grown on the surface of the substrate still cannot be controlled unless a catalyst pattern created by a mask or lithography step is used.

#### 3.1.1.1 Synthesis of ZnO Nanowire via VLS Process

The VLS growth mechanism, first proposed and studied in detail in the 1960s and 1970s by Wagner and Givargizov [163-165], is an ideal synthetic technique to control nanowire growth. There are several ways of making the process work, and here we focus on one of the simplest in which nanowire growth is controlled by a chemical vapor deposition (CVD) method. In principle, by choosing a materials system with a simple eutectic phase diagram, a catalyst droplet, generally a liquid Au-semiconductor eutectic alloy, is formed on a surface and exposed to carrier gases that provide the growth materials for semiconductor

nanowires, as shown in Figure 3.2. The growth materials are adsorbed preferentially at the catalytic droplets, compared with the remaining regions of the surface. The droplets become supersaturated and the growth material precipitates from the droplets. The droplets, subsequently, continues to absorb the growth materials and a wire-shape of the growth material forms beneath the droplets, with the droplet remaining on the tip. The diameter of the deposited nanowire depends on the droplet size, while its length is determined by the growth time and process conditions.

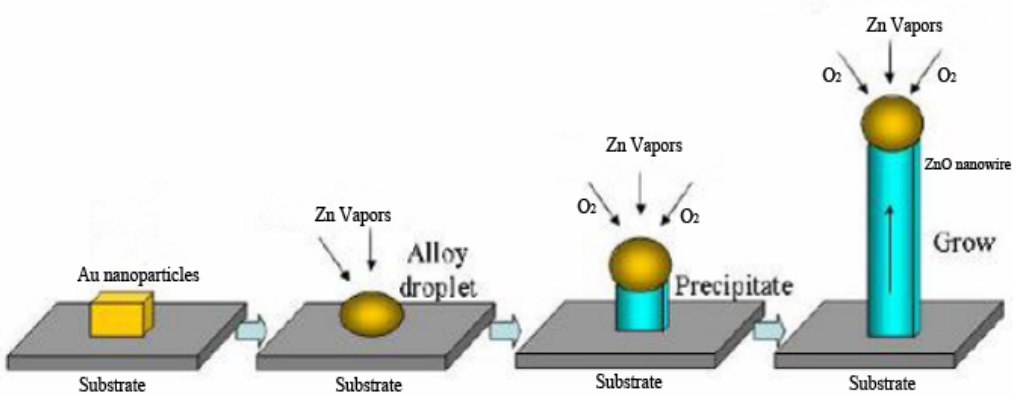


**Figure 3.2** Schematic diagram of VLS mechanism in vertical growth process of ZnO nanowire.

### 3.1.1.2 Synthesis of ZnO Nanowire via Hydrothermal Process

Synthesis of ZnO nanowires through a liquid phase method exhibits many advantages when compared to a vapor phase method, such as low cost, low temperature, scalability, and ease of handling. Particularly, liquid phase synthesis occurs at a relatively low temperature (usually < 200 °C), which allows for a greater choice of substrates including inorganic and organic substrates. Here the process of solution phase synthesis is referred to

as the hydrothermal growth method. The hydrothermal growth process of ZnO nanowires generally consists of the following steps [166-175]:

1) A thin ZnO seed layer is coated on a certain substrate. This layer can reduce the thermodynamic barrier, resulting in promotion of nucleation for the further growth of ZnO nanowires on the substrate;
2) An alkaline reagent, for example, NaOH or hexamethylenetetramine ($(CH_2)_6N_4$, or HMTA), is mixed with an $Zn^{2+}$ salt solution, such as $Zn(NO_3)_2$ or zinc acetate ($Zn(CH_3COO)_2$). The aqueous solution is used as a precursor solution for nanowire growth;
3) The substrate coated with the ZnO seed layer is placed in the growth solution at a certain temperature and a certain period;
4) The resultant substrate is removed from the growth solution and is washed and dried.

In typical hydrothermal method, ZnO nanowires are synthesized based on the following chemical reactions when HMTA and $Zn(NO_3)_2$ mixture is chosen as the precursor solution:

$$(CH_2)_6N_4 + 6H_2O \rightarrow 4NH_3 + 6HCHO \quad (3-1)$$

$$NH_3 + H_2O \leftrightarrow NH_3 \cdot H_2O \quad (3-2)$$

$$NH_3 \cdot H_2O \leftrightarrow NH_4^+ + OH^- \quad (3-3)$$

$$Zn^{2+} + 2OH^- \leftrightarrow Zn(OH)_2 \quad (3-4)$$

$$Zn(OH)_2 \leftrightarrow ZnO + H_2O \quad (3-5)$$

During the nanowire growth process, HMTA hydrolyzes into formaldehyde and ammonia, performing as a *p*H buffer by slowly decomposing itself to provide a gradual and

controllable resource of ammonia, which can form ammonium hydroxide and support $OH^-$. $Zn^{2+}$ can complex with $OH^-$ to form monomeric hydroxyl species such as $Zn(OH)_2$. Then solid ZnO nuclei are produced by the dehydration of these hydroxyl species. The ZnO nuclei continue to grow by the condensation of the hydroxyl groups with the zinc-hydroxyl complexes. In addition, HMTA and ammonia can also coordinate to the ZnO crystal, retarding the growth rate of certain plane surfaces of the ZnO crystal.

The hydrothermal growth process can be controlled by adjusting the reaction parameters, such as reactants concentration, growth temperature and growth time, etc. Generally, the concentration of growth solution determines the nanowire density, while the growth temperature and duration determine the shape and aspect ratio of the resultant ZnO nanowire.

### 3.1.2 Synthesis of CuO Nanowire via Thermal Oxidation Method

Copper Oxide (CuO) is known to be a *p*-type semiconductor material with a narrow bandgap of approximate 1.4 eV, and it is also a typical antiferromagnetic material with local magnetic moment per unit formula of 0.6 $\mu_B$ [176]. In recent years, CuO has received extensive attention for its potential applications in fields such as solar cells, field-emission emitters, electronic cathode, photocatalyst and sensors [176-186]. Particularly, for field-enhancement application, CuO nanowires with a large aspect ratio are more favorable than its bulk and film counterparts. To date, CuO nanowires have been synthesized by various methods such as chemical routes, template approaches and electrospinning techniques. However, a much simpler and more convenient route for the synthesis of aligned CuO

nanowires via directly thermally-oxidized copper substrates has been reported recently [182-186], which shows the huge potential to be adapted for large-scale quantities. The CuO nanowire arrays obtained from the thermal oxidation method usually exhibit good crystallinity, high aspect ratios, and uniform density distribution, which render them attractive and promising building blocks for fabricating high-performance electronic devices.

The thermal oxidation method, generally, refers to growth of metal oxide nanowires by heating of corresponding metals directly in an atmosphere involving oxygen gas. The nanowires are regarded as the products from reaction between metal and oxygen gas. For example, CuO nanowires can be synthesized on a Cu substrate by heating the Cu plate in air at above 400 °C [182,185].

The growth mechanism of CuO nanowires through thermal oxidation of Cu substrate was proposed by Gonçalves et al [180] very recently and is widely accepted by other research groups now. According to his proposed model, CuO nanowires are formed as a result of rapid, short-circuit diffusion of the Cu atoms across grain boundaries and/or defects in a $Cu_2O$ underlayer. A schematic of the proposed growth model is shown in Figure 3.3. Initially a $Cu_2O$ thin layer is formed on a Cu substrate. This layer is highly porous and defective due to the large interface compressive stress. Since the $Cu_2O$ layer totally covers the surface of the Cu substrate, further oxidation requires that Cu atoms reach the $Cu_2O$/air growing interface by two pathways: lattice and grain-boundary diffusion. The migration of Cu atoms via lattice pathway leads to a continuous increase of the $Cu_2O$ and CuO layers, whereas the diffusion of Cu atoms via grain-boundary pathway results in the formation of

CuO nanowires. The time dependence of the nanowire length, observed in the thermal oxidation process, can be directly attributed to grain-boundary diffusion of Cu atoms toward the $Cu_2O$/CuO interface since the variations in the nanowire densities and diameters during growth process are small [180]. In fact, the morphology of the nanowires is determined by the microstructure of the underlying $Cu_2O$ and CuO layers where the short-circuit diffusion of Cu atoms takes place.

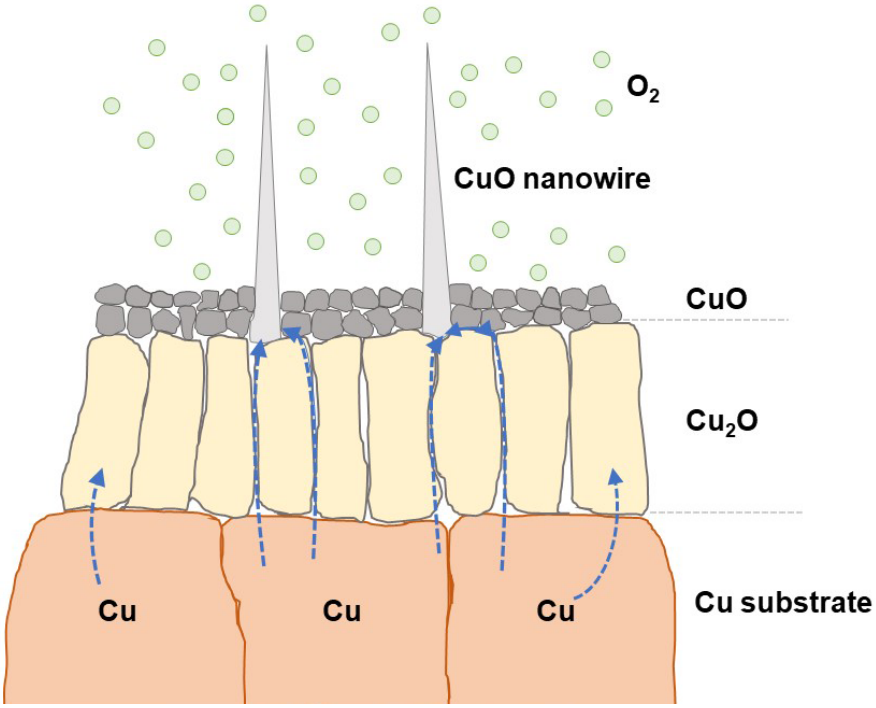


**Figure 3.3** Schematic diagram of proposed model for the growth mechanism of CuO nanowires via thermal oxidation method.

## 3.2 Synthesis of EL Phosphor Materials

Almost all EL phosphors are synthesized by solid-state reactions between raw materials at a certain high temperature [37,41]. Figure 3.4 shows the general synthesis process of EL phosphor materials. Briefly, the high-purity raw materials including the host, activators,

and/or additives are blended, mixed, and then sintered thoroughly. Subsequently, the sintered phosphor product undergoes crush, milling, and then sieving in order to remove coarse and excessively crushing particles. In some situations, the phosphor product also needs to be subjected to surface treatment such as surface polish.

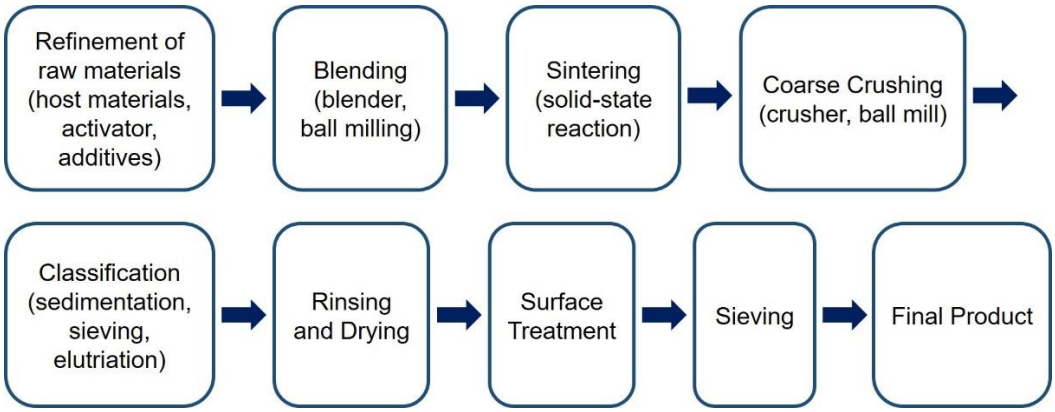


**Figure 3.4** General synthesis process of EL phosphor materials [41].

The performance of EL devices is essentially determined by the property of phosphor powder materials, which is affected by particle size and surface treatment of phosphor. It is important to control the particle size during the synthesis process for satisfying the application requirements of EL devices. For example, the optimum coating thickness of thin-film EL devices is roughly proportional to the average particle size of the phosphor powders. The smaller the particle size is, the thinner the coating thickness can be. Also, fine-particle phosphors can achieve dense coating layers for EL devices. However, luminescence efficiency tends to become lower with reduction of phosphor particle size. Therefore, phosphor materials possessing of a small particle size and high luminescence efficiency will be optimized EL powders [41].

## 3.3 Finite Element Modelling Method

The simulation the electric field in the nanowire-based AC powder EL device is achieved by a finite element modelling method, which is usually carried out by electromagnetic field simulation software. Agros 2D from the Hermes Library, a powerful technique for two-dimensional electromagnetic and electrostatic-field simulation through the finite element method (FEM), was employed.

Before simulation, it is assumed that the $Zn_2GeO_4$:Mn phosphor is a linear and isotropic material with a relative permittivity of 14.7 and the nanowires are conductors. In addition, it is assumed that there is no electrical breakdown in the phosphor material and PMMA dielectric layer, the latter having a dielectric constant of 4. The electrostatic simulation is based on Poisson's Equation:

$$\nabla \cdot (\varepsilon_r \varepsilon_0 \nabla \phi(x, y)) = -\rho(x, y) \qquad (3-6)$$

where $\phi(x, y)$ is the electric potential, $\varepsilon_r$ is the relatively permittivity, $\varepsilon_0$ is the permittivity of vacuum ($8.85 \times 10^{-12}$ F/m), and $\rho(x, y)$ is the charge density.

The first step in simulation is mesh generation. The solution volume is divided into a large number of elements and vertices as shown in Figure 3.5. A given potential value (120V) is assigned to the top electrode (ITO) and the bottom electrode (Ni/Au paste) is set to 0 V. Once the potential $\phi(x, y)$ is generated, the electric field simulation automatically calculates the electric field E using $E(x, y) = -\nabla \phi(x, y)$ according to the following boundary conditions for any two media (medium 1and medium 2).

$$\text{Tangential E: } E_{1t} = E_{2t}; \qquad (3-7)$$

$$\text{Normal E: } \varepsilon_1 E_{1n} - \varepsilon_2 E_{2n} = \rho_s \tag{3–8}$$

where $E_{1n}$ is the normal component of electric field directed away from medium, $E_{2n}$ is the normal component of electric field directed away from medium 2, $\rho_s$ is the surface charge density at the interface between two media. Thus the total field energy can be calculated by equation as follow:

$$U = \iiint \frac{\varepsilon_r \varepsilon_0}{2} E^2 dv \tag{3–9}$$

Starting from a few hundred triangles, the number of triangles continuously increases until the field energy between two iterations is less than 1% which is considered as convergence and computation is finished.

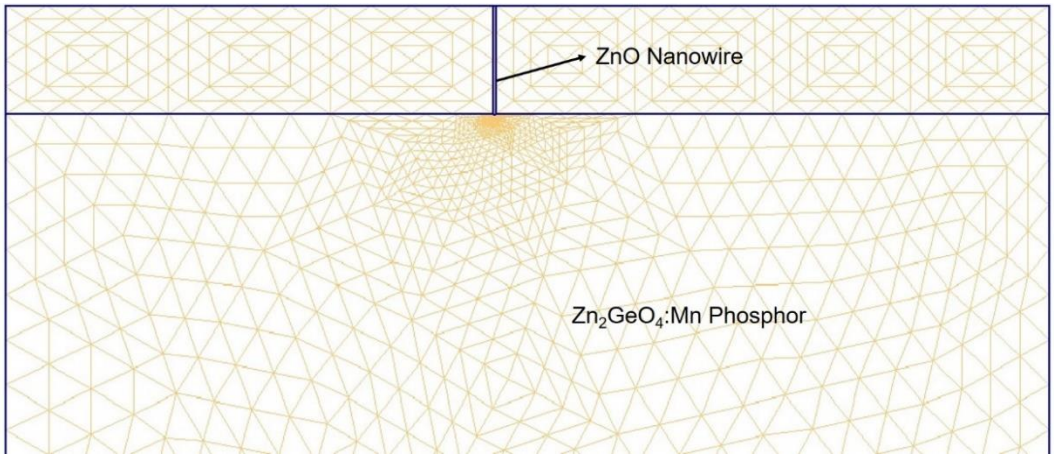


**Figure 3.5** Illustration of the mesh generation in the Agros 2D finite-element modelling for the ZnO nanowire-based AC Powder EL device.

## 3.4 Characterization and Measurement Techniques

### 3.4.1 Scanning Electron Microscopy (SEM)

SEM (JEOL 7000F) is the main technique to characterize each component of the nanostructured EL powder device, such as phosphor pellets, Au nanoparticles, nanowires, PMMA layer etc. All images were obtained using the secondary electron detector, with ~3 keV acceleration voltage.

### 3.4.2 Transmission Electron Microscopy (TEM)

TEM (JEM 2010F) was used to obtain crystalline information of the as-synthesized nanomaterials. The diffraction pattern can confirm the prior growth direction of nanowires. High-resolution TEM shows the alignment of atom lines in various crystal planes and also defects in crystals. Energy dispersive X-ray spectrum (EDS) combined with TEM was collected using a Si:Li detector with 5 keV acceleration voltage, which is used to measure the relative concentrations of the component elements in the nanowires.

### 3.4.3 X-Ray Diffraction (XRD)

The structures of the phosphor material and nanowires, as well as the junction structures between phosphor and nanowires are determined by comparing observed X-ray diffraction (XRD) patterns to those in the Joint Committee on Powder Diffraction (JCPD) Database. The diffraction patterns were collected by a Nicolet diffractometer using a copper $K_{\alpha}$ radiation of 0.154 nm (Bruker D8 Advance Powder).

### 3.4.4 Photoluminescence (PL) Spectrum

Photoluminescence is the excitation of photons by absorption of incident light. It can be used to provide a qualitative analysis of a sample. The wavelength of the emitted light is usually longer than the incident light. PL spectrum can be used to obtain information about the excitation process that leads to the photon being emitted. In this work, a PL spectrum was used to characterize the light emission in the $Zn_2GeO_4$:Mn phosphor materials. The spectrum shows the wavelength of peak emission intensity in the phosphor materials, as well as the luminance of the phosphor materials. In addition, it was used to measure the emission wavelength of a ZnO nanowire array, which is related to the structured defects in ZnO nanowires. A He-Cd laser with a wavelength of 325 nm was used as an excitation source.

### 3.4.5 Electroluminescence (EL) Measurement System

For EL measurement, sinusoidal pulses with bias voltage were applied between the two electrodes using a pulse generator-amplifier combination, and then the applied AC voltage and frequency were monitored using an oscilloscope (Tektronix TDS 1002B). EL emission from the device was collected by an optical fiber connected to an Acton SP-2300 monochromator. Luminance was measured by a Minolta LS100 Luminance Meter.

# Chapter 4. ZnO Nanowire-Based AC Powder EL Devices

## 4.1 Fabrication of CVD-Growth ZnO Nanowire-Based AC Powder EL Devices

$Zn_2GeO_4$:Mn phosphor powders are synthesized by solid-state reaction and undergo cold pressing to form pellets, which are used as substrates for further ZnO nanowires growth. Secondly, vertically-aligned ZnO nanowires are grown on the as-prepared $Zn_2GeO_4$:Mn phosphor pellets by chemical vapor deposition (CVD) process. Thirdly, the $Zn_2GeO_4$:Mn phosphor pellets with ZnO nanowires are connected to the external metal and ITO electrodes for EL characterization .

### 4.1.1 Preparation of $Zn_2GeO_4$:Mn Phosphor Pellet

The procedure of preparation of $Zn_2GeO_4$:Mn phosphor pellets follows our previous work [48]. Pure ZnO, $GeO_2$ and MnO powders were mixed and ball-milled with zirconia milling balls (5.08 mm in diameter) in ethanol overnight. The mixture was then sintered in air at 1100 °C for three hours, in which a reaction occurred:

$$GeO_2 + 2(1-x)ZnO + 2xMnO \rightarrow Zn_{2-2x}Mn_{2x}GeO_4 \qquad (4-1)$$

The value of $x$ was chosen to be 4 at % in this reaction. The resultant product was again ball-milled and sintered in order to ensure that the reaction was completed. After that, the as-prepared $Zn_2GeO_4$:Mn phosphor powders were pressed into a circular pellet with a

diameter of ~1cm by a hydraulic press, which can provide a force of 24,000 lbs (or 1.36 GPa). The pressed $Zn_2GeO_4$:Mn phosphor pellets were then annealed in nitrogen ambient at 1100 °C for three hours in order to obtain a high-crystalline phosphor product.

$Zn_2GeO_4$:Mn phosphor material is used as the light emission layer in the AC powder EL device. This phosphor has a very strong photoluminescence (PL) emission under ultraviolet (UV) excitation of 325 nm. It can emit a bright green light under illumination of ~254 nm UV light which was produced by a mercury lamp, as shown in Figure 4.1.

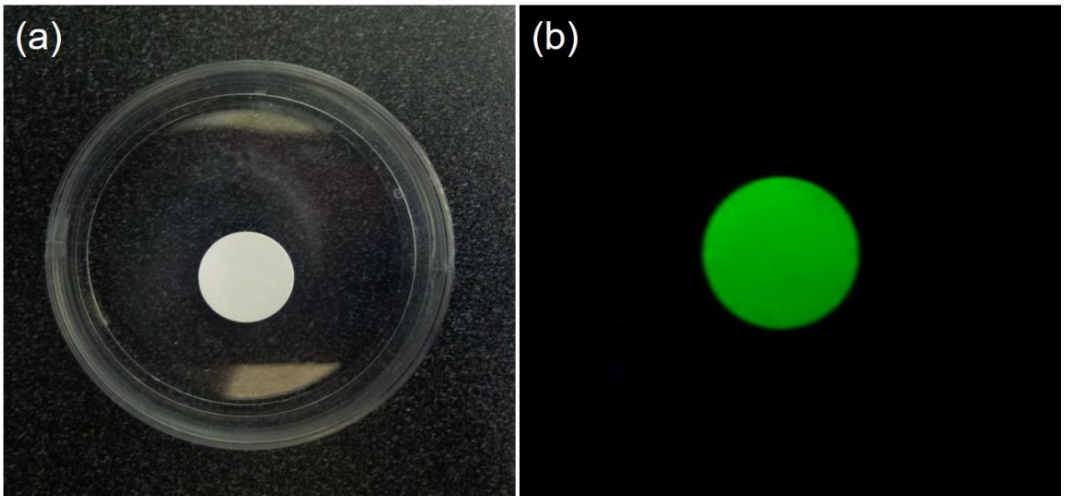


**Figure 4.1** The as-prepared $Zn_2GeO_4$:Mn phosphor pellet under illumination of UV light. (a) The phosphor pellet in natural environment; (b) A green emission of the same phosphor pellet under illumination of ~254 nm UV light. The diameter of the phosphor pellet is ~1 cm.

#### 4.1.1.1 Densification of $Zn_2GeO_4$:Mn phosphor Pellet

Increasing the density of phosphor pellet can efficiently increase its luminance due to reduce of inherent defects such as holes and grain boundaries with increase the size of phosphor grains. The method employed to increase the density of phosphor pellet was post-

annealing, in which different annealing temperatures were applied to study the densification process (Figure 4.2).

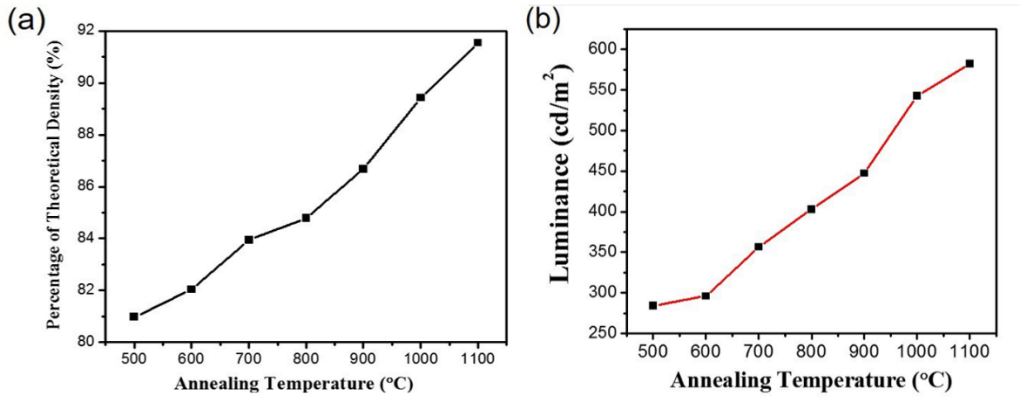


**Figure 4.2** Densification process of the phosphor pellet. (a) Percentage of theoretical density (~ 4.73 g/cm$^3$) of $Zn_2GeO_4$:Mn phosphor as a function of annealing temperatures; (b) Luminance of the phosphors versus annealing temperatures.

The average density of the fresh pressed phosphor pellets is approximate 3.50 g/cm$^3$. The pellets were annealed in nitrogen ambient at a set of specific temperatures ranging from 500 °C to 1100 °C, as shown in Figure 4.2(a). At an annealing temperature of 1100 °C, the density of the pellet increased by ~20% to 4.32 g/cm$^3$, which yields ~ 92% of the theoretical density of $Zn_2GeO_4$:Mn phosphor of 4.73 g/cm$^3$. Meanwhile, the luminance of the phosphor pellet was higher and higher with increasing annealing temperature because of optimizing grain growth of the phosphor.

### 4.1.1.2 X-Ray Diffraction of $Zn_2GeO_4$:Mn Phosphor Pellet

Figure 4.3 shows the X-ray diffraction (XRD) patterns of the as-synthesized $Zn_2GeO_4$:Mn phosphor pellet, which experienced post-annealing at 1100 °C for 3 hours. All of the diffraction peaks match very well with $Zn_2GeO_4$ crystal of a rhombohedral

structure (JCPDS 11-0687) with lattice constants of a = b = 14.23 Å and c = 9.53 Å. Because the radius of the substitutive $Mn^{2+}$ (~0.8 nm) is very close to that of $Zn^{2+}$ (0.74 nm), nearly no difference in diffraction pattern was detected.

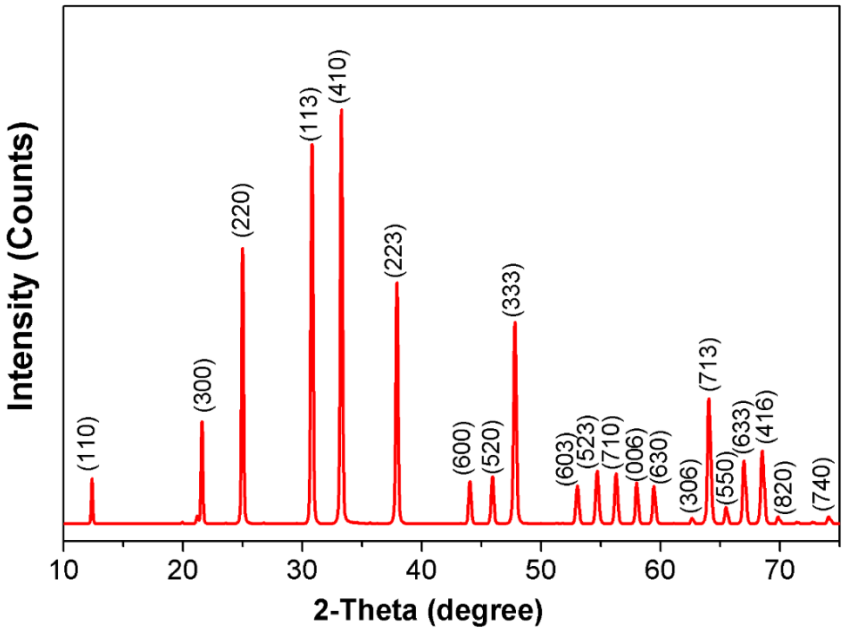


**Figure 4.3** XRD pattern of the as-prepared $Zn_2GeO_4$:Mn phosphor pellet.

### 4.1.1.3 Photoluminescence Spectrum of $Zn_2GeO_4$:Mn Phosphor Pellet

The photoluminescence (PL) emission spectrum for a $Zn_2GeO_4$:Mn phosphor pellet that emits green light is shown in Figure 4.4. The emission of the phosphor pellet excited with 325 nm laser showed a peak at 535 nm, which is due to the $^4T_1(^4G) \rightarrow {}^6A_1(^6S)$ transition of $Mn^{2+}$ ions sitting on tetrahedrally coordinated $Zn^{2+}$ sites [30]. The PL spectrum is indistinguishable from the EL spectrum in $Zn_2GeO_4$:Mn phosphor due to the same state transition of $Mn^{2+}$ ions.

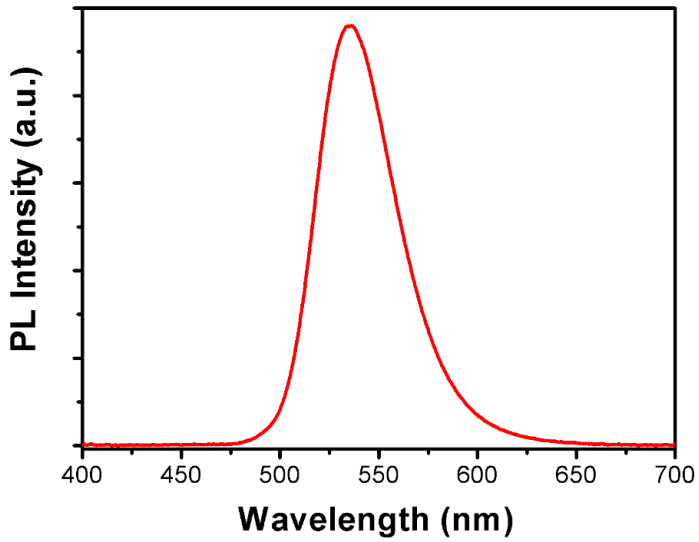


**Figure 4.4** PL spectrum of $Zn_2GeO_4$:Mn phosphor pellet. The red line shows a typical spectrum with a peak wavelength of 535 nm.

### 4.1.2 CVD Growth of Vertically Aligned ZnO Nanowires

After obtained high-quality $Zn_2GeO_4$:Mn phosphor pellets, a thin Au film with a certain thickness was deposited on the phosphor pellets by the sputtering deposition method. The thickness of deposited Au film can be adjusted by controlling deposition time. The Au-coated phosphor pellets were put into a tube furnace system and annealed for 30 min or three hours, depending on the thickness of deposited Au film, at 950 °C or 1100 °C under argon ambient.

The Au-coated phosphor pellets, subsequently, were employed as substrates for growth of ZnO nanowires through a CVD method. The experimental system is as illustrated in Figure 4.5. The temperature of the system is controlled by a thermocouple inserted in the middle of the furnace.

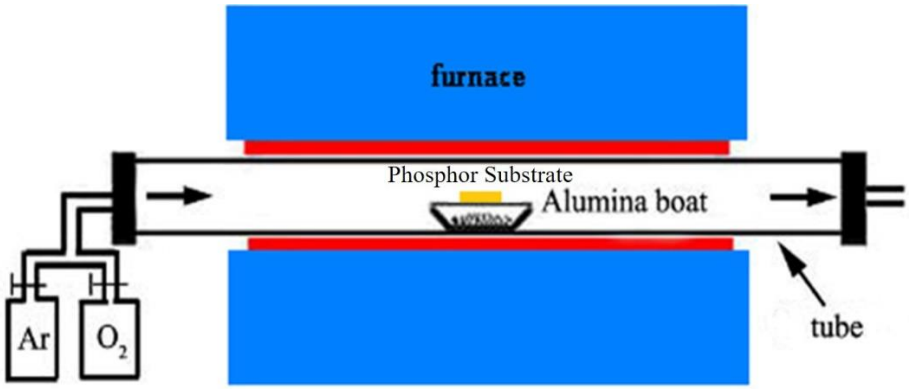


**Figure 4.5** Schematic diagram of the experimental system for ZnO nanowires growth via CVD method.

A mixture of equal amounts (by weight) of pure ZnO powder (Alfa Aesar, ~ 100 mesh, 99.9 %) and graphite powder (Alfa Aesar, ~325 mesh, 99 %) was used as the evaporating source. The source was contained in an alumina boat placed at the center of a mullite tube which was inserted in a horizontal tube furnace. At one end of the tube, there were inlets for oxygen and argon gases whose flow rates were controlled by flowmeters, respectively. The Au-coated phosphor pellets were used as substrates and placed directly above the source, with the Au-coated side facing toward the source. The set temperature of the system was 950 °C.

At the beginning of experiment, 60 sccm (standard cubic centimeters per minute) of Ar gas was introduced into the tube for an hour to purge the system. Then the furnace was heated to the set temperature at an approximate rate of 50 °C/min. When the system reached the set temperature, the flow rate of Ar and $O_2$ were adjusted to 50 sccm and 1 sccm, respectively. The temperature was held at the peak temperature for 30 min or one hour. Finally, the products were removed from the furnace after the system cooled down to room temperature.

#### 4.1.2.1 Study on The Growth Behaviour of Vertically Aligned ZnO Nanowires

By using the CVD method, vertically aligned ZnO nanowires were grown on the $Zn_2GeO_4$:Mn phosphor pellet that underwent annealing at 1100 °C for 3 hours. Many researchers have shown that the growth of ZnO nanowires by CVD is very sensitive to process conditions [187-195]. Subtle changes in experimental conditions, such as source temperature, the distance between substrate and source, gas flux, substrate material, and choice of catalyst etc., can cause distinct changes in the shape, size and density of the nanowires. In addition, according to the VLS growth mechanism, the size, shape, and spatial density of the ZnO nanowires are significantly determined by the size and spatial density of Au catalysts. The morphologies of the nanowires are also proved to be influenced by the source powder used in the CVD growth process. In this research, the effects of the oxygen gas flow, the gold catalyst layer, and the source powder material are demonstrated to determine the morphologies of the ZnO nanowires.

**1) Effect of Oxygen Gas Flow**

When ZnO nanowires are grown by using a mixture of ZnO and graphite as the CVD source, the density, lengths, and diameters of the nanowires are affected by the introduced $O_2$ flow and the thickness of Au film. There is no nanowire growth when $O_2$ is not introduced into the system [187]. Wang and co-workers [188-192] have shown that high-quality aligned ZnO nanowires can only be achieved at a reasonable supersaturation level of Zn vapor and the oxygen partial pressure has a strong influence on the supersaturation of Zn vapor when ZnO and graphite are used as source. According to their report, there is

no nanowire growth when the oxygen volume percent exceeds 3 % of the $Ar/O_2$ gases mixture. Wan [187] reported that the average density and length of ZnO nanowires increase with increasing of $O_2$ amount during the process. But excess $O_2$ may degrade the growth of nanowires. Consequently, ZnO nanowires with high density and good quality can be only obtained at a suitable duration of $O_2$ flow. Figure 4.6 shows the effect of the oxygen partial pressure on the growth of ZnO nanowires. In this experiment, the thickness of the Au film is 45 nm, and the $O_2$ flow is fixed at 1 sccm. Four different ratios of $Ar:O_2$ (40:1, 50:1, 60:1: 70:1 sccm) were used while keeping other process conditions constant. The result indicates that clean, high-quality ZnO nanowires can be obtained at a suitable $Ar/O_2$ ratio.

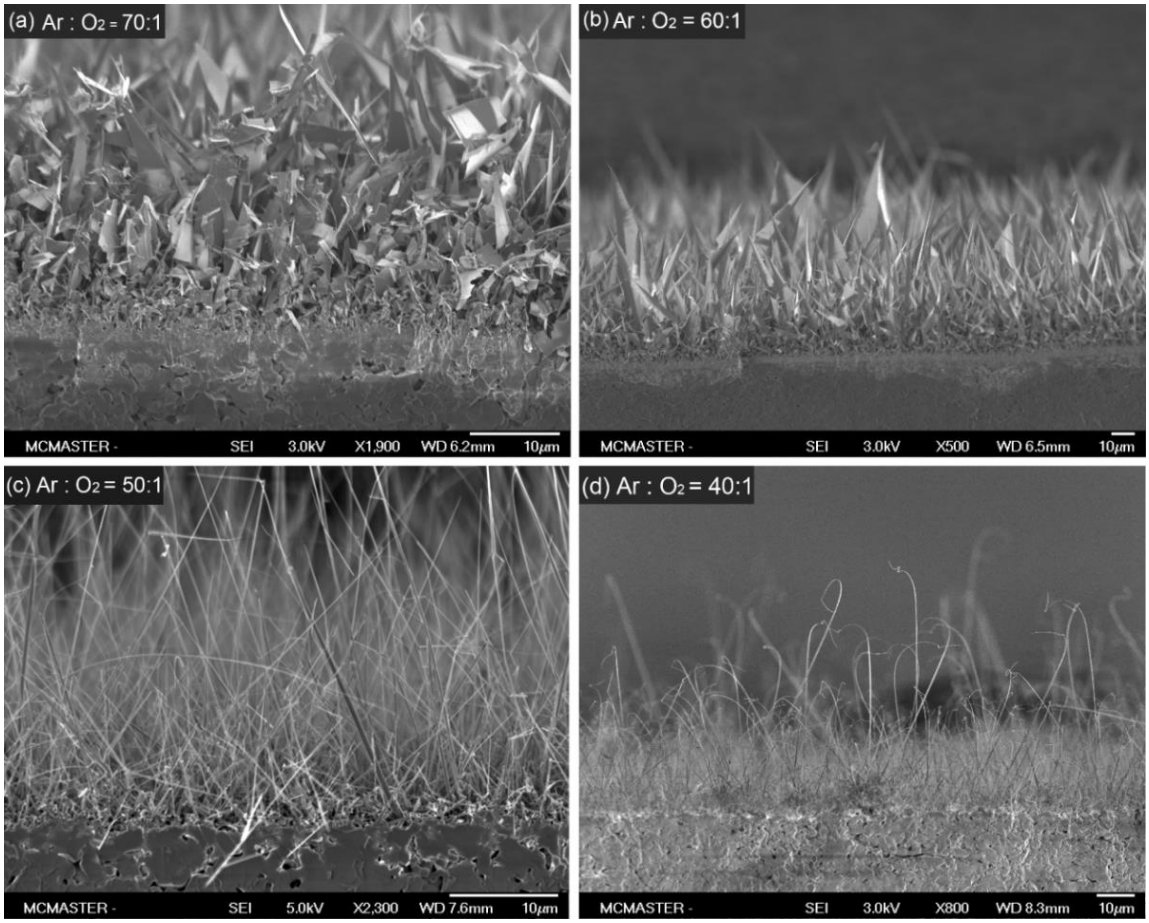


**Figure 4.6** Cross-sectional SEM images of ZnO nanostructures grown on at different ratio of $Ar/O_2$ gaseous mixture: (a) $Ar/O_2$ is 70; (b) $Ar/O_2$ is 60; (c) $Ar/O_2$ is 50; (d) $Ar/O_2$ is 40.

### 2) Effect of Thickness of Au Nanoparticle Layer

To investigate the effect of the thickness of the Au catalyst on the growth of ZnO nanowires, Au catalyst films of 3, 8, 15 and 45 nm thick are used. Figure 4.7 shows the dependence of the SEM images on the thickness of the Au film when the ratio of $Ar/O_2$ gaseous mixture is maintained at 50:1. It indicates that the thickness of deposited Au film can influence the density and diameter of the nanowires. The density and average lengths of the nanowires decreased apparently with reducing the thickness of Au catalyst film on

the $Zn_2GeO_4$:Mn phosphor substrate, while the diameters of nanowires decrease slightly when the thicknesses of Au films increase.

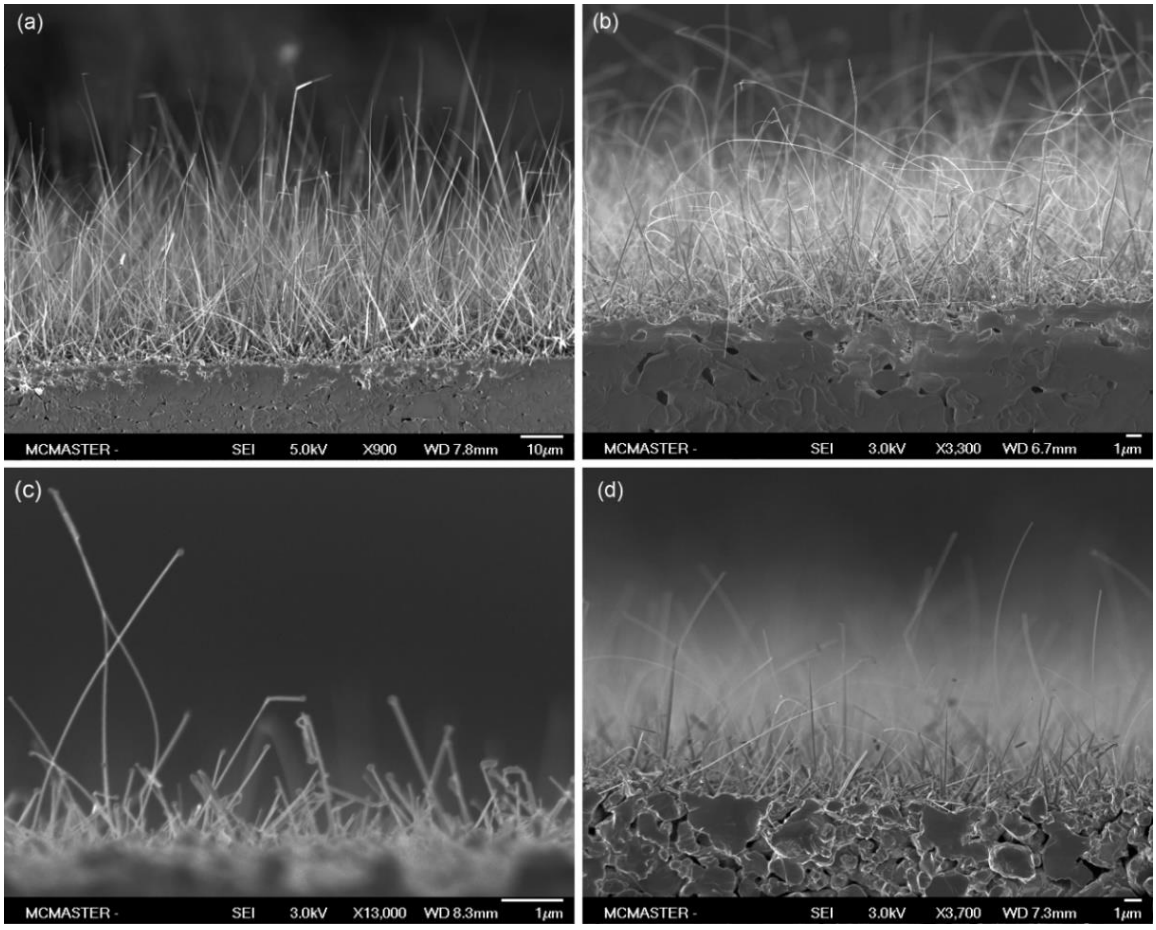


**Figure 4.7** Cross-sectional SEM images of ZnO nanowires grown $Zn_2GeO_4$:Mn phosphor substrate as catalyzed by a deposited Au film with thicknesses of (a) 45 nm; (b) 15 nm; (c) 8 nm; and (d) 3 nm.

### 3) Effect of CVD Source Powder Materials

By using different vapor sources, it was discovered that ZnO nanostructures with other morphologies readily formed rather than nanowires. For example, when pure Zn powder was used as source, a large yield of tetra-pods nanostructures can be synthesized (Figure 4.8). Other morphologies of ZnO nanostructure, such as sheet-like and grid-like structures,

can also be formed under different process conditions. These different nanostructures may have interesting physical properties, and particularly optical properties.

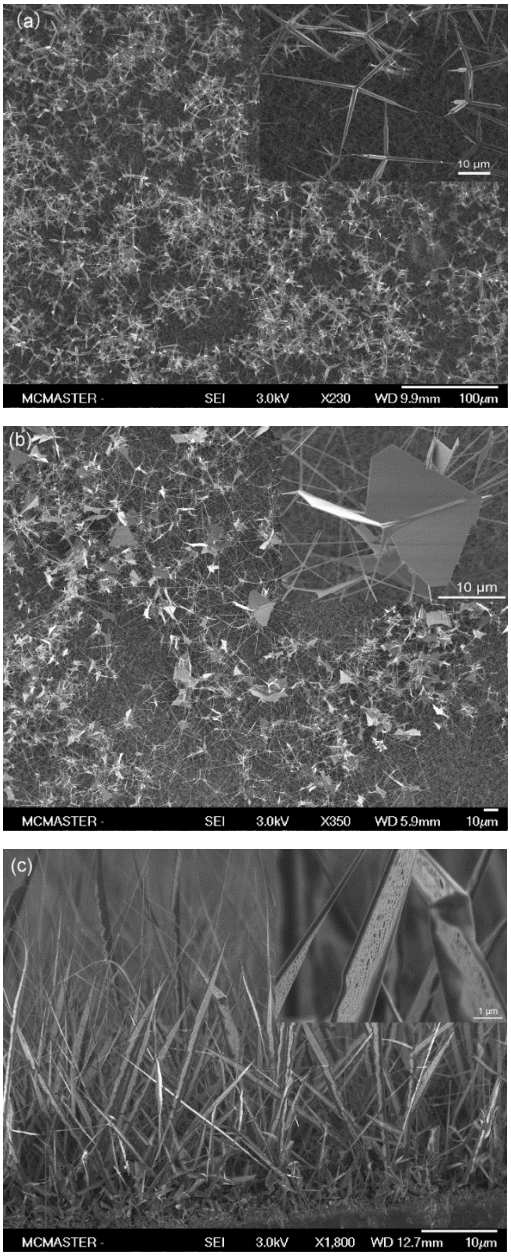


**Figure 4.8** SEM images of various morphologies of ZnO nanostructures grown on $Zn_2GeO_4$:Mn phosphor substrate using pure Zn powder as the vapor source.

#### 4.1.2.2 Density-Controlled Growth of Vertically Aligned ZnO Nanowires

From the application point of view, the density of the aligned ZnO nanowires is very important since it directly influence the distribution of electric field near the tips of nanowires in EL devices, and it is also related to how the nanowires interact with each other optically, electronically, and mechanically. In a field emission process, for example, an array of densely-packed nanowires greatly reduces the field enhancement effect at the nanowire tip to a level not much different from a flat metal plate, while too loosely distributed nanowires cannot meet the desired requirement of brightness [196-199]. Effectively control the density of the aligned nanowires for optimal performance can be realized through adjusting the space between the aligned nanowires. So far, two methods are used in tailoring the density. One method is to adjust the concentration of catalyst in a colloidal solution before applying it onto the substrate [196], but the uniformity of nanoparticle distributions over a large surface area is questionable because of the agglomeration of the particles during the drying process. Another method is to use a patterning technique, such as mask, electron-beam lithography, or scanning probe microscopy, which can provide precise control over the density but at a much higher cost. These approaches also cannot meet the requirement for large-area growth. Therefore, it is the pivotal point to find out an effective and simple pathway for the control of nanowire density without using sophisticated techniques. In this research, we proposed two practical approaches to control the spatial density of nanowires: i) Control the density of Au catalyst particles by adjusting the annealing process of the pre-deposited Au thin film; ii) Varying

of the spatial distance between the Au-coated phosphor substrate and source powder during CVD growth process.

**1) Control of The Density of Au Catalyst Nanoparticles**

The spatial density of ZnO nanowires array is significantly determined by the spatial density of Au catalyst nanoparticles when the growth of nanowires follows the vapor-liquid-solid (VLS) model. In order to investigate spatial-density control of ZnO nanowires on the polycrystalline $Zn_2GeO_4$:Mn phosphor substrates, an approach is to adjust the spatial density of Au catalyst nanoparticles prior to the CVD nanowire growth process. In this scenario, after obtaining high-quality $Zn_2GeO_4$:Mn phosphor pellets, Au thin films of approximate 8 nm were deposited on the phosphor pellets by sputtering deposition and annealed at 1100 °C for different annealing duration of pre-deposited Au thin films. As a result, isolated Au catalyst nanoparticles with three different spatial densities were formed on the phosphor pellet substrates and employed for density-controlled growth of ZnO nanowires in a CVD synthesis process. Figure 4.9 shows that Au catalyst nanoparticles having various densities were formed on the phosphor pellet substrates.

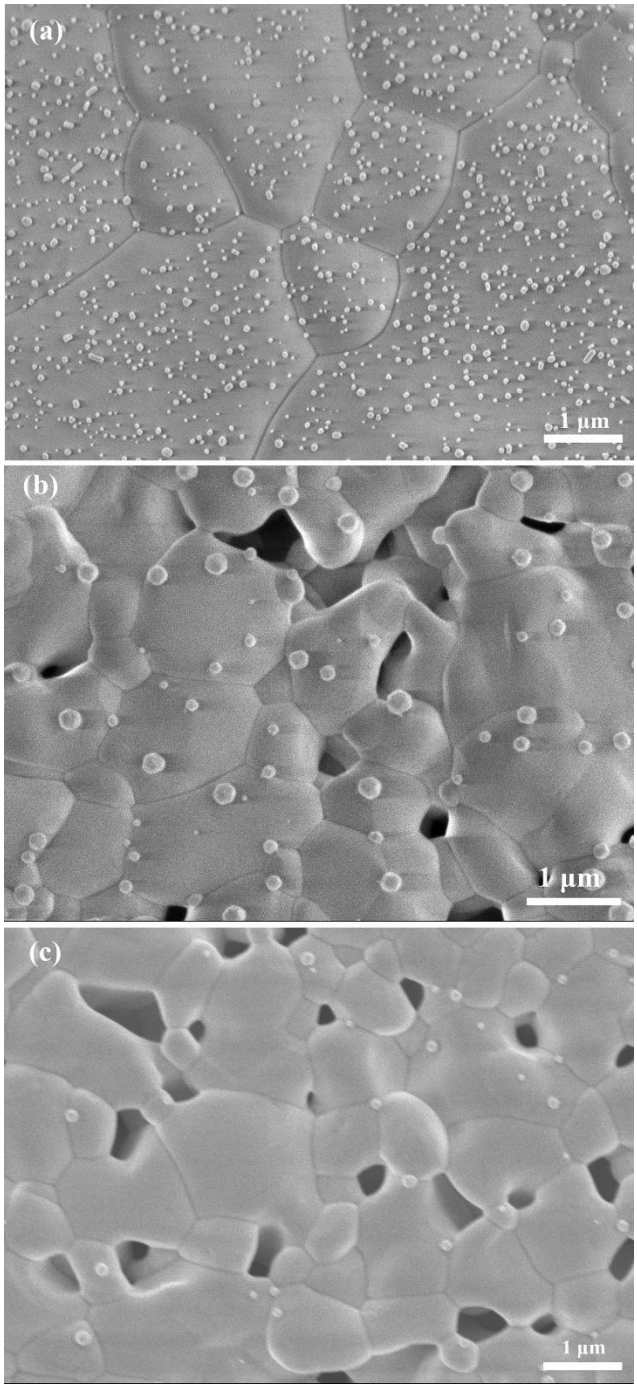


**Figure 4.9** SEM images of the Au catalyst nanoparticles after annealing at three different process conditions: (a) 1100 °C for 0.5 hour; (b) 1100 °C for 1 hour; (c) 1100 °C for 2 hours.

Then the above samples with different densities of Au nucleation were used as the substrates to grow ZnO nanowires through the CVD method. Because the evaporation and coalescence effects of the Au nanoparticles increase with increasing of annealing duration, the longer the annealing duration is, the lower the spatial density of the Au catalyst nanoparticles on the phosphor substrate becomes. Figure 4.10 shows the aforementioned growth situation of the nanowire samples with various Au catalyst nucleation densities. The average spatial density of the vertical nanowires is about 4 per $\mu m^2$ in figure (a), about 2 per $\mu m^2$ in figure (b), and about 1 per $\mu m^2$ in figure (c), respectively. The spatial density of the as-synthesized nanowires exhibits a positive proportional relationship with the spatial density of the Au nucleation. That is, the spatial density of the nanowires is largely determined by the spatial density of the Au catalyst nucleation. Consequently, the density of the ZnO nanowires could be effectively adjusted by the spatial density of the Au catalyst nucleation on the $Zn_2GeO_4$:Mn phosphor substrate.

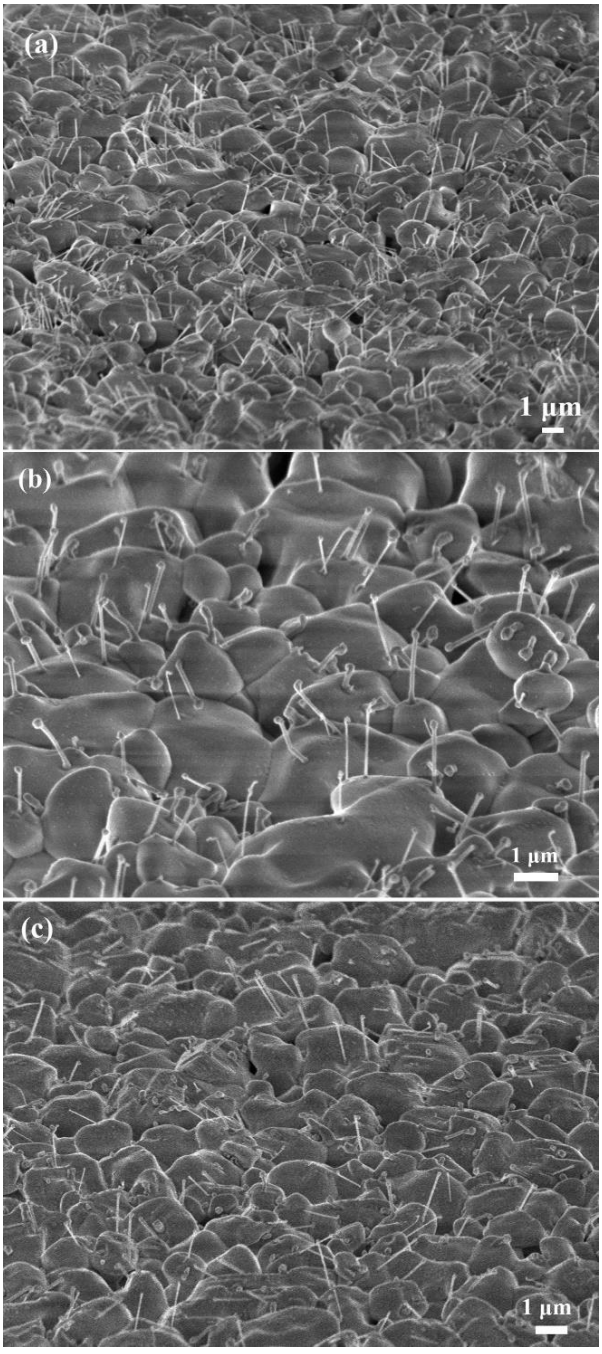


**Figure 4.10** SEM images showed the variation in the density of the as-synthesized ZnO nanowires on $Zn_2GeO_4$:Mn phosphor pellet substrate via three different aforementioned annealing conditions. (a) 1100 °C for 0.5 hour; (b) 1100 °C for 1 hour; (c) 1100 °C for 2 hours.

**2) Control of The Spatial Distance between Phosphor Substrate and Source Powder**

In this study, another approach through adjusting the spatial distance between the phosphor substrate and source powders during CVD growth process, is alternatively demonstrated to achieve spatial-density controlled-growth of ZnO nanowires on the $Zn_2GeO_4$:Mn phosphor. To this end, $Zn_2GeO_4$:Mn phosphor substrates coated with ~ 8 nm of Au thin film were placed between two zones of CVD source powders (a mixture of ZnO and graphite). That is, one zone of source powder was located at the upstream side of the substrate, and the other was located at the downstream side in the tube. The distance from each zone to the center of the substrate was the same. The position of the system is shown in Figure 4.11(a). After the CVD growth process, a gradually varying density distribution of ZnO nanowires was observed on the $Zn_2GeO_4$:Mn phosphor substrate. The average lengths of ZnO nanowires decreased from zone 1 to 4 on the phosphor substrate, as shown in Figure 4.11 (b)-(e). The density distribution trend is almost the same in the upstream side, resulting in a symmetric distribution with respect to the center area (zone 4) of the phosphor substrate [200].

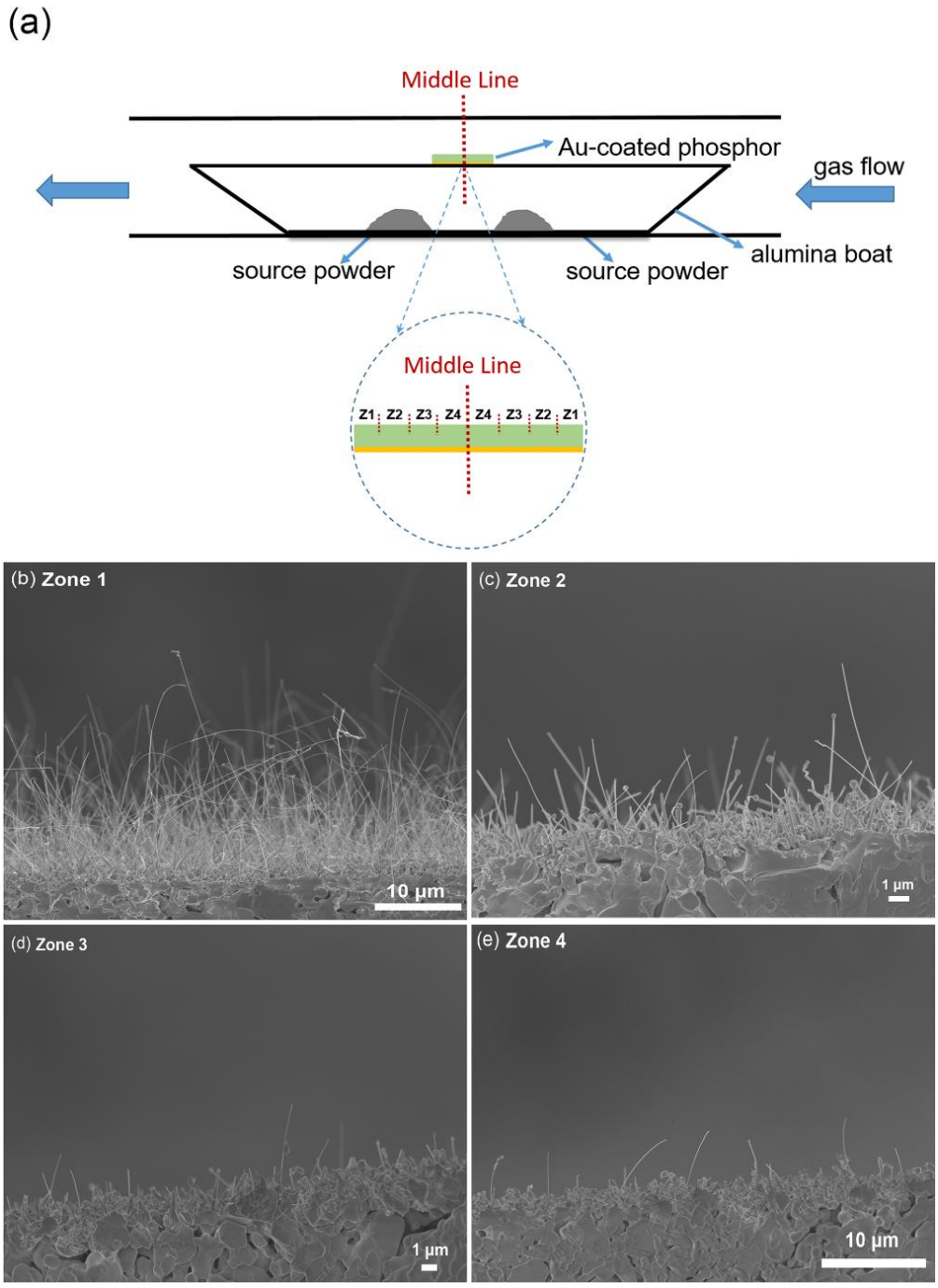


**Figure 4.11** Symmetric density distribution of ZnO nanowires on the phosphor substrate. (a) Schematic diagram of the system used in this experiment. (b)-(e) Cross-sectional SEM images of ZnO nanowires grown on different regions of the substrate. Each zone number indicated in images (b)-(e) corresponds to the relevant z-number in (a) [200].

This clearly shows the density distribution pattern of the nanowires on the phosphor circular substrate. Figure 4.12 shows the histogram which demonstrates the linear nanowire density corresponding to the location zones indicated in the cross-sectional SEM images in Figure 4.11. This lateral growth approach was found to be repeatable and we have done approximately ten growths with the same source powder geometry yielding predictable nanowire density results. From an experimental point of view, the spatial gradient in nanowire density is useful since it allows a series of nanowire densities to be explored in only one growth.

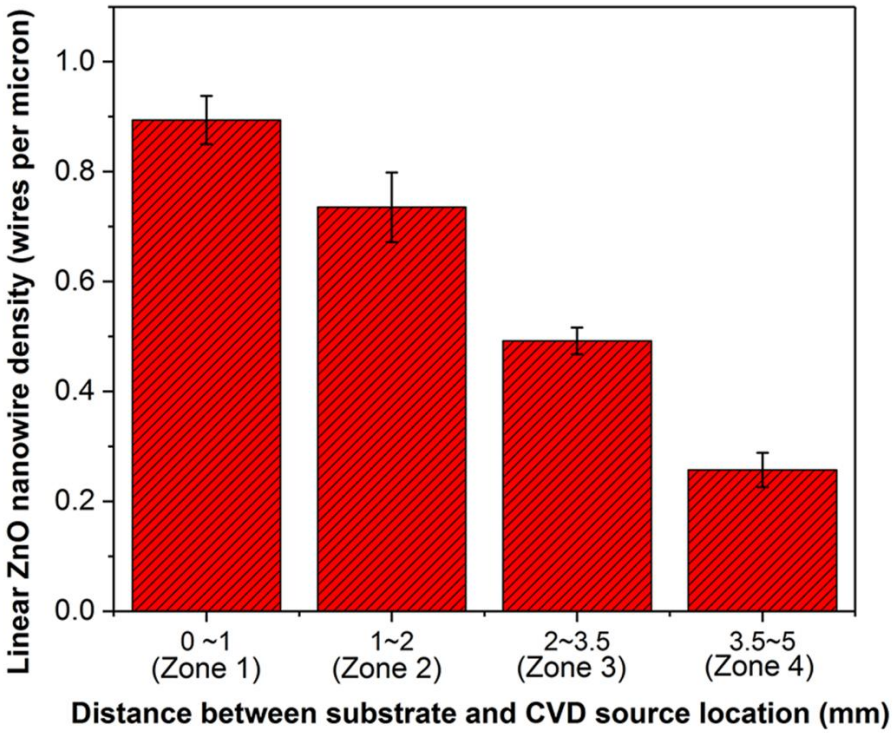


**Figure 4.12** Linear ZnO nanowire density as a function of the distance between the phosphor substrate and the location of the source powder in CVD synthesis (the diameter of a circular $Zn_2GeO_4$:Mn phosphor substrate is 1 cm).

This novel symmetric growth pattern is clearly associated with the concentration of ZnO vapors that gradually decreases with lateral distance from each source powder zone and reaches a minimum at the central area of the phosphor substrate (see Figure 4.13). After the set temperature (950 °C) is reached, zinc vapor is continuously formed during the carbothermal reaction and oxidized by the oxygen vapor in the ambient. Heated ZnO vapor diffuses to the catalyst-anchored surface of the substrate and nucleates at catalyst positions. The chance for ZnO vapor to engage with Au nucleation positions apparently decreases due to decreasing of ZnO vapor concentration. Therefore, the highest density of ZnO nanowires is located at the substrate edges which are in closer proximity to the source positions followed a gradually decreasing trend towards the central area, in which the lowest density of the nanowires was observed. It is worth noting that the surface of the $Zn_2GeO_4$:Mn phosphor substrate is not as smooth as silicon wafer or glass substrates used in most other research on ZnO nanowire growth. It has grain surface roughness in the micron scale and features a high density of grain boundaries. The topography of the substrate definitely affects the surface diffusion and movement of zinc vapor in the CVD synthesis process of ZnO nanowires. Consequently, the density of ZnO nanowire also can be influenced by the unique topography of the $Zn_2GeO_4$:Mn phosphor substrate.

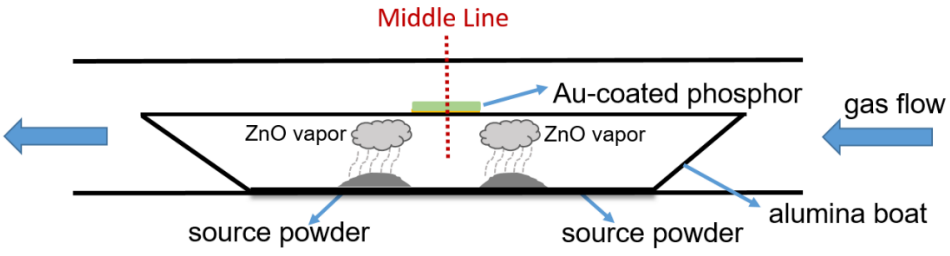


**Figure 4.13** Schematic image for the symmetric growth during CVD process.

#### 4.1.2.3 Structure Characterization of The As-Synthesized ZnO Nanowire

The XRD result of the ZnO/$Zn_2GeO_4$:Mn composite in Figure 4.14 shows that the pattern of the composite is composed from two individual sets of patterns of ZnO and $Zn_2GeO_4$:Mn crystals. Each set matches the pure component (ZnO or $Zn_2GeO_4$:Mn) very well. No impurity phase was detected. The intensities of ZnO diffraction peaks are apparently higher than that of $Zn_2GeO_4$:Mn crystal because the incident ray went through the sample from the ZnO nanowires top layer to the $Zn_2GeO_4$:Mn bottom layer. The diffraction peaks of a ZnO crystal can be indexed to a hexagonal structure with cell constants of a = 3.25 Å and c = 5.20 Å, while $Zn_2GeO_4$:Mn has rhombohedral index with cell constants of a = b = 14.26 Å and c = 9.54 Å. In addition, the diffraction intensity of the (002) plane in the X-raypattern of ZnO crystal is very strong, which confirms that the preferential growth direction of ZnO nanowires is <0001>, forming the lengths of the nanowires.

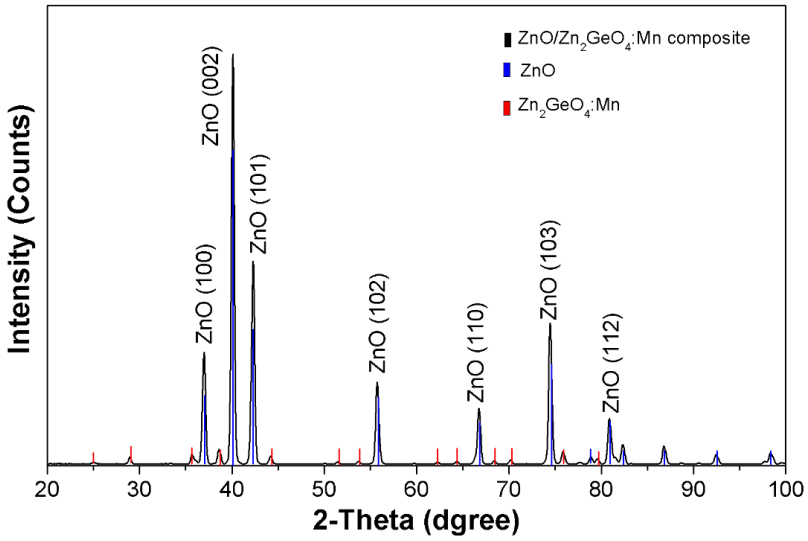


**Figure 4.14** XRD pattern of the ZnO/$Zn_2GeO_4$:Mn composite.

Additional structural characterization of the ZnO nanowires was carried out using transmission electron microscopy (TEM). Figure 4.15(a) shows a TEM image of a ZnO nanowire. The surface of the nanowire is clean and without any amorphous phase. High-resolution TEM image (Figure 4.15(b)) and selected area electron diffraction pattern (inset in Figure 4.8(b)) reveals that the spacing of 0.52 nm between adjacent lattice planes corresponds to the interplanar spacing of *c* axis of ZnO hexagonal crystal, confirming <0001> as the growth direction for the as-synthesized ZnO nanowires. This <0001> preferential growth direction is also reflected in the high diffraction intensity of (002) peak of XRD pattern in Figure 4.16.

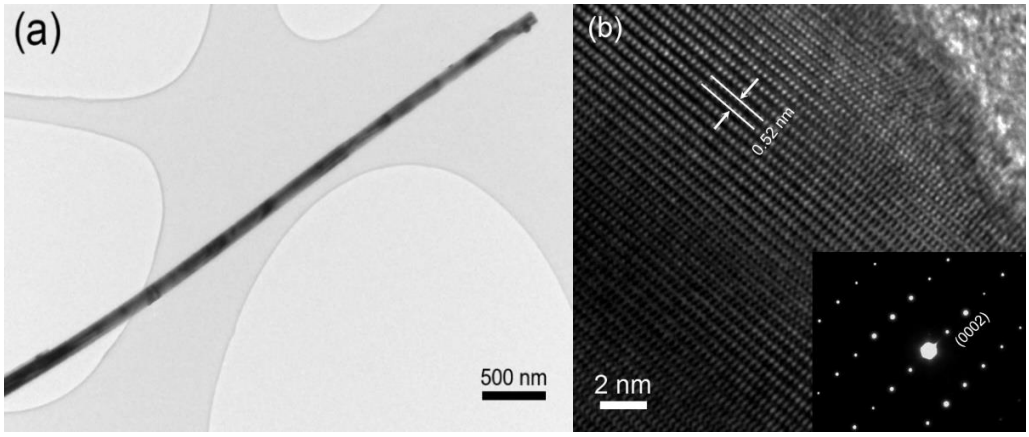


**Figure 4.15** TEM images of a ZnO nanowire. (a) Low-magnification TEM image of a ZnO nanowire lain on a copper grid; (b) High-resolution TEM image of a single-crystalline ZnO nanowire showing the lattice fringes. The inset is the corresponding selected area electron diffraction pattern.

The energy dispersive X-ray spectrum (EDS) of the ZnO nanowire is shown in Figure 4.16. The linear-scanning mode was used in the EDS spectrum to measure the component elements within a single ZnO nanowire. The result indicates that the composition is ZnO. The peaks of Cu and Si in the spectrum were generated from the grid and the peak of C is caused by carbon coating process.

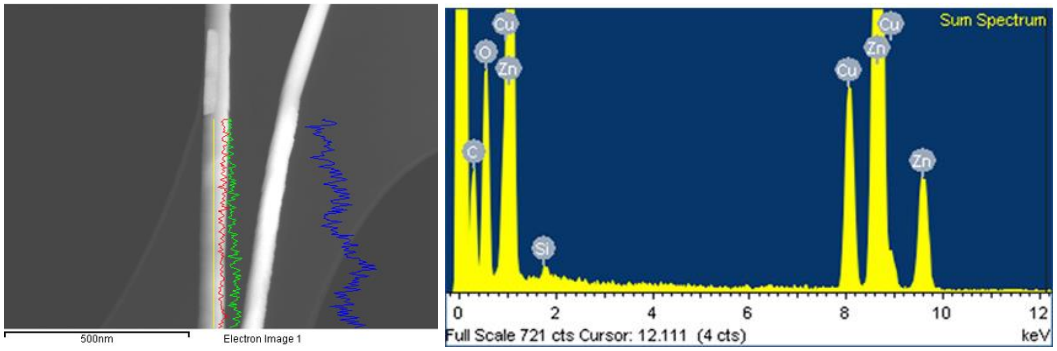


**Figure 4.16** The Energy Dispersive X-ray spectrum (EDS) of the ZnO nanowire using linear-scanning mode.

In order to investigate the PL performance of pure ZnO nanowires, a sample comprising ZnO nanowires which were swept off from the $Zn_2GeO_4$:Mn substrate and deposited on a clean silicon wafer. A He-Cd laser (325 nm) was used as the excitation source. Figure 4.17 shows a room-temperature PL spectrum of ZnO nanowires with an average diameter of 200 nm. Strong emission at 380 nm was observed corresponding to the near band-edge emission of ZnO. In addition, a broad green emission at ~520 nm is commonly referred to as a deep-level or trap-state emission [194], which is generally attributed to singly ionized oxygen vacancies in ZnO and the emission results from the radiative recombination of a photogenerated hole with an electron occupying the oxygen vacancy [201].

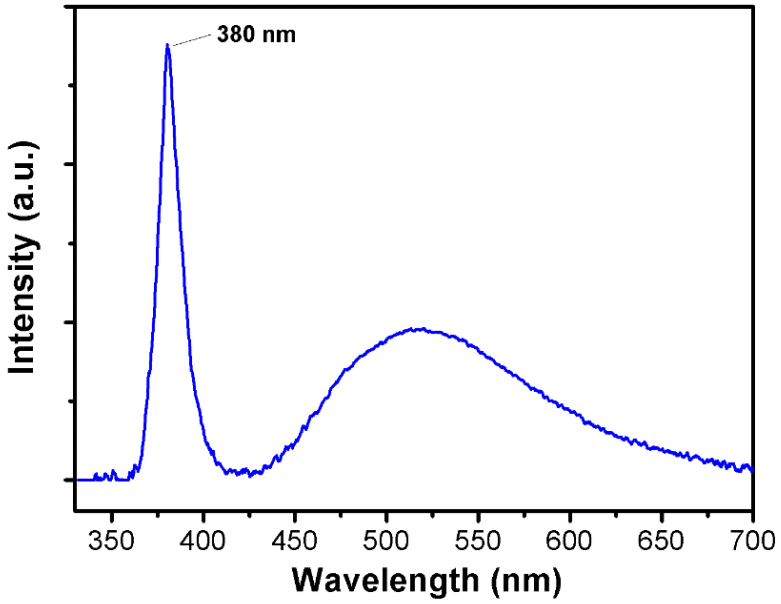


**Figure 4.17** PL spectrum of ZnO nanowires grown on a silicon wafer.

### 4.1.3 Assembly of CVD-Growth ZnO Nanowire-Based EL Device

To accomplish the fabrication of an AC powder EL device, a transparent and relatively-low dielectric layer is needed to fill the space between ZnO nanowires and the top ITO electrode. Methylmethacrylate (PMMA) is spin-coated to envelop the nanowires and forms a thin dielectric layer (~ 1 μm) after curing. Subsequently, a 100~200 nm ITO film is sputtered to form the front common electrode by magnetron sputtering system. Meanwhile, a Ni/Au paste is used to form the back electrode and is mounted on a metal plate. Finally, an AC voltage is applied to the device to generate EL emission (see Figure 4.18).

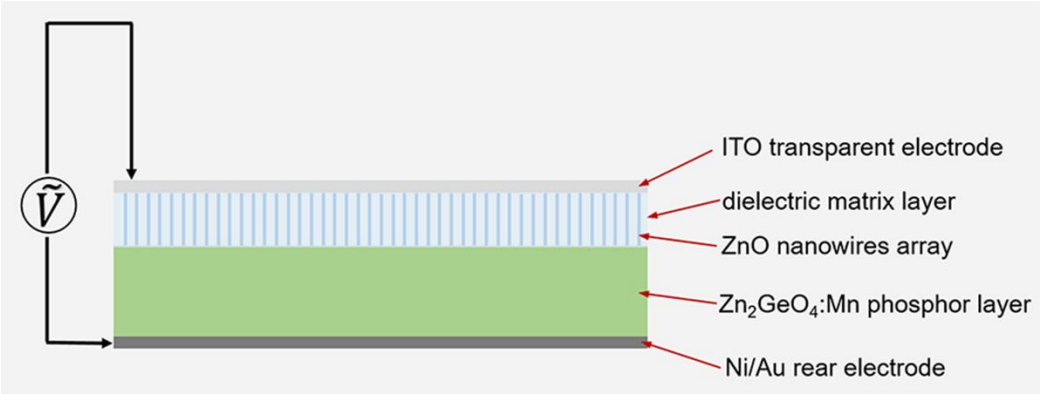


**Figure 4.18** Schematic diagram of the as-fabricated AC powder EL device based on ZnO nanowires array grown on $Zn_2GeO_4$:Mn phosphor pellet.

### 4.1.4 Simulation of Electric Field for ZnO Nanowire-Based EL Devices

The explanation of light generation from ZnO nanowires-based EL device was demonstrated in the bipolar field-emission model (see Section 2.1.4). If the conducting nanowire is considered as a long isolated charged cylinder which is surrounded by vacuum

in an electric field, the field intensity of the nanowire at the nanowire tip can be expressed as [202]:

$$E = \frac{\lambda}{\pi \varepsilon_0 D} \qquad (4-2)$$

where $\lambda$ is linear charge density along the nanowire, $\varepsilon_0$ is the permittivity of vacuum, and $D$ is diameter of the nanowire. It can be seen from equation 4-2 that a thinner nanowire can induce a higher field under the same linear charge density. But the precise value of field intensity is more complicated when the interfaces of nanowires and phosphors are introduced into the calculation. The distribution of electric field within the phosphor substrate, therefore, is not modelled in detail. However, if a certain voltage is applied to a conducting nanowire grown on phosphor substrate with a perfect interface, it can be firmly predicted that a higher electric field will be produced in the phosphor region where a heterojunction structure is formed at the tip of the conducting nanowire, comparing with other regions in the phosphor.

In order to quantitatively characterize the electric field in the phosphor, static electric simulations were performed by using a 2D electric field simulation software (Agros 2D). Here we assume: (1) no breakdown in both phosphor and fill-in dielectric material (such as PMMA); (2) an average nanowire diameter D of 100 nm is used in the simulation and the applied voltage V is set to 120 V between the top and bottom electrodes. Figure 4.19 (a) shows that the simulated distribution of electric field within the phosphor substrate. The dependence of the electric field on depth is shown in Figure 4.19 (b). The highest intensity is obtained at the tip of the nanowire, and the intensity of the electric field is on the order

of $10^7$ V/m. The curve shows that the electric field decreases rapidly as the distance from the tip increases and within ~8 μm from the tip of nanowire it relaxes to about the average electric field, which is calculated to be ~5 x$10^5$ V/m by assuming that the device performs like a capacitor and the distance between two planar electrodes is ~200 μm. The simulation matches the electric field calculation result by using the boundary element method (BEM) very well [203,204].

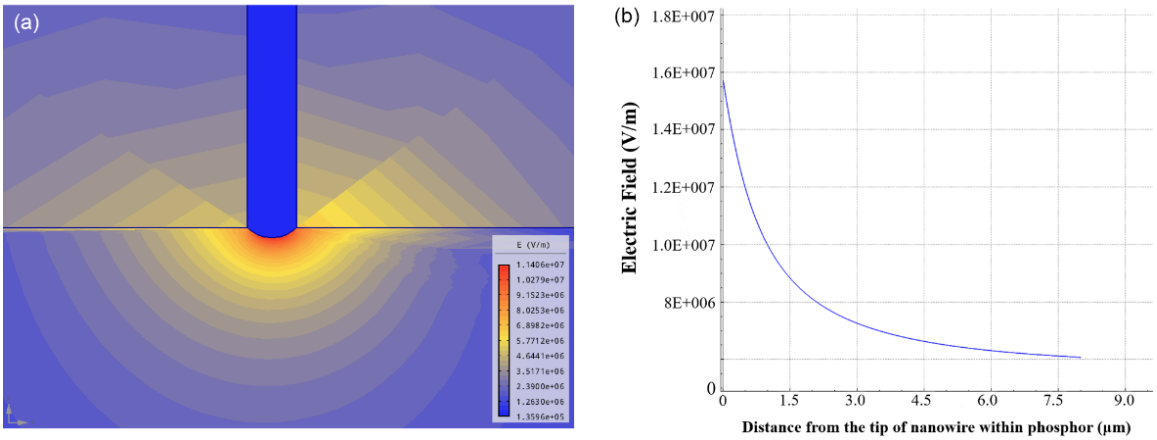


**Figure 4.19** (a) 2D simulation of distribution of electric field within the phosphor layer resulting from the formation of heterojunction introduced by the conducting nanowire; (b) Electric field in the y-direction as a function of the distance from the nanowire tip.

### 1) Effect of Nanowire Diameter (D) on Local Electric Field

According to equation 4-2, the electric field intensity is inversely proportional to D, where D is the diameter of the conducting nanowire. Therefore, smaller nanowires can induce a higher localized field in the phosphor body under the same conditions compared to a large nanowire. Figure 4.20 shows the dependence of electric field on the diameter when the applied voltage is 120 V, calculated by the Agros 2D software. As a result,

decreasing the size of the nanowires is an effective way to increase the localized electric field, eventually lower the operating voltage and increase the brightness of the EL device.

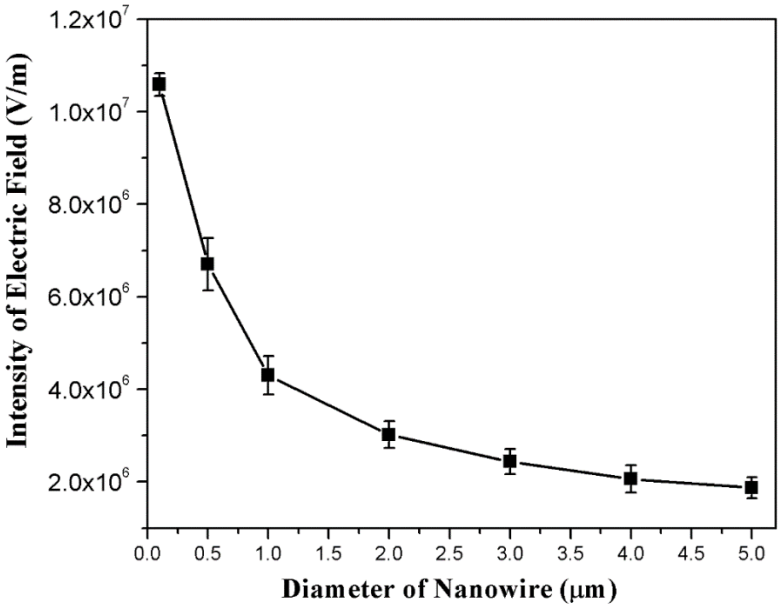


**Figure 4.20** Dependence of localized electric field on diameters of ZnO nanowire.

**2) Effect of Spatial Density of Nanowires on Local Electric Field**

As mentioned above, the density of the aligned ZnO nanowires is very important since it directly influence the distribution of electric field near the tips of nanowires in EL devices. Recent studies on field-emission properties of carbon nanotubes and ZnO nanowires reveal that both the turn-on voltage and emission current density strongly depend on the areal density of nanowires [196-199]. In particular, medium density of the nanotubes showed the highest emitted current densities. The poor emission of high density distribution might be explained by an electrostatic screening effect provoked by the proximity of neighboring nanotubes. The presence of high-density nanotubes means that there is more charge per unit area and the charge reduces the potential drop perpendicular into the phosphor, not

much different from a flat metal plate. While too loosely distributed nanowires cannot meet the desired requirements of high-emitting points. Figure 4.21 shows the dependence of electric field on the inter-wire spacing.

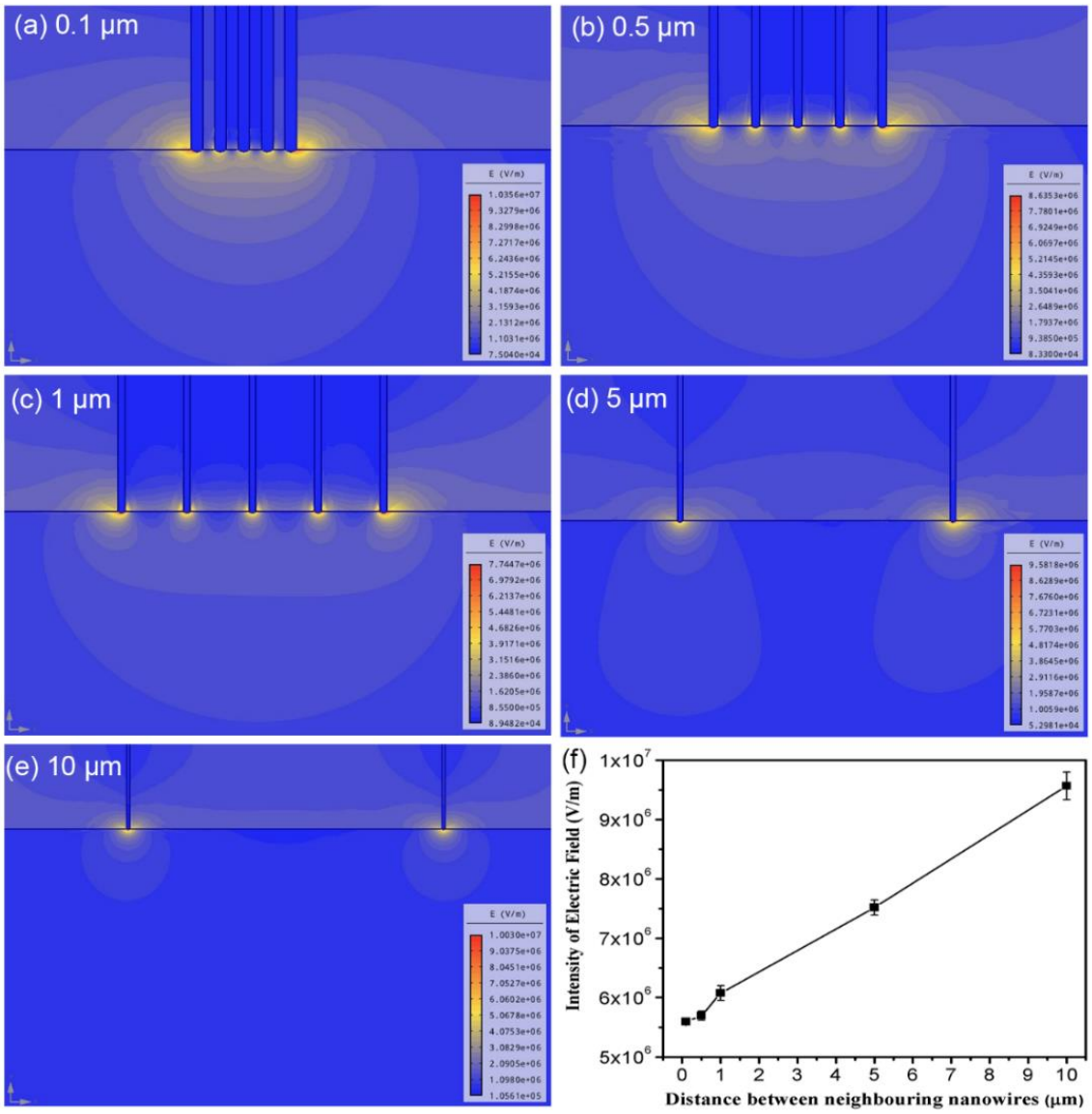


**Figure 4.21** (a)~(e) 2D simulation of electric field varying with the spacing between nanowires; (f) The intensity of electric field as a function of inter-wire spacing.

As shown in Figure 4.21 above, the intensity of electric field increases when the spacing between nanowires raising from 0.1 to 10 μm. According to the Fowler-Nordheim law, the field-emitted current $I \alpha E^2 / W^{3/2} \exp(-BW^{3/2} / E)$, where $E$ is the electric field intensity. Therefore, a significant increase of the emitted current can be achieved even a slightly higher of electric field is applied, which make the nanowire performs like a rectifying diode. However, more accurate 3D simulation is needed to calculate the distribution of electric field that is close to practical devices in the future.

### 4.1.5 Formation of Heterogeneous Structure between The ZnO Nanowire and Phosphor Particles

The heterojunction structure between the ZnO nanowire and $Zn_2GeO_4$:Mn substrate plays a pivotal role in determination of the performance of future EL devices by means of influencing the tunneling effect of the emitted electrons from ZnO nanowires into the $Zn_2GeO_4$:Mn phosphor. In order to investigate the ZnO-$Zn_2GeO_4$:Mn interface, the as-synthesized ZnO nanowires were mechanically stripped off from the $Zn_2GeO_4$:Mn phosphor pellet. Short (less than 2 μm) and thick ZnO nanowires (~200 nm of diameter) were chosen because they could survive with intact heterojunctions to $Zn_2GeO_4$:Mn fragments during the stripping process. Figure 4.22a and Figure 4.22b show TEM images of the heterojunctions between a single ZnO nanowire and $Zn_2GeO_4$:Mn crystal fragment, which were taken from various pieces of the dispersed TEM sample. It can be clearly viewed that the ZnO nanowire is approximately vertical to the surface of a particular $Zn_2GeO_4$:Mn structure. The insets in Figure 4.22a shows selected-area diffraction (SAD) patterns of the nanowire and the $Zn_2GeO_4$:Mn crystal structure, respectively. Growth

direction (0001) of the ZnO nanowire is the same as the one shown in Figure 4.15. As a typical example, a HRTEM image of this ZnO-$Zn_2GeO_4$:Mn interface from the sample in Figure 4.22b reveals the detailed crystal structures, as shown in Figure 4.22c. An enlarged view of the interfacial area (marked by the circle in Figure 4.22c) is shown in Figure 4.22d. The planar spacing for five (010) planes of ZnO ($5 \times 0.29 = 1.45$ nm) is approximately the same as two (110) planes of $Zn_2GeO_4$:Mn ($2 \times 0.72 = 1.44$ nm). An ordered hetero-epitaxial interface between the ZnO (0001) plane and the $Zn_2GeO_4$:Mn (110) plane may be present, however, a more detailed investigation is needed on the hetero-epitaxial interfaces.

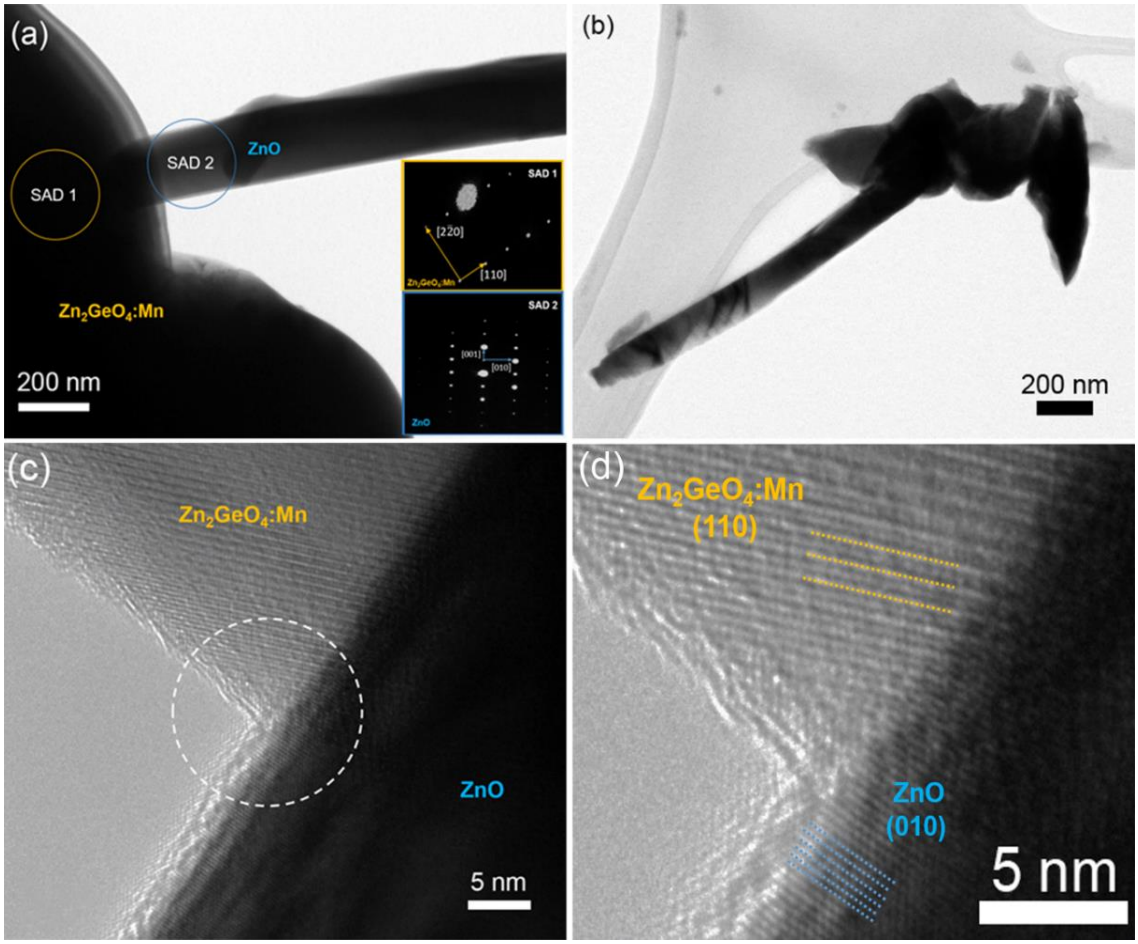


**Figure 4.22** (a) and (b) TEM images of short and thick ZnO nanowires grown on $Zn_2GeO_4$:Mn crystal substrates. Insert: SAD patterns of $Zn_2GeO_4$:Mn crystal (SAD 1) and ZnO nanowire (SAD 2); (c) HRTEM image of the ZnO-$Zn_2GeO_4$:Mn interface region;(d) Enlarged view of the interface (marked circle in c) showing the crystal structures and possibly an ordered hetero-epitaxial interface. The (110) planar spacing of $Zn_2GeO_4$:Mn is 0.72 nm, and the (010) planar spacing of ZnO is 0.29 nm.

### 4.1.6 EL Characteristics of The CVD-Growth ZnO Nanowire-Based EL Devices

The ZnO nanowires were grown on $Zn_2GeO_4$:Mn phosphor pellet, the backside of which is attached on an aluminum stub by nickel paste. A piece of ITO glass was used to contact the top of nanowires array, and the EL characteristics were measured when external

AC voltages with pulse waveforms were applied on the sample. As shown in Figure 4.23, green light is observed from the sample when the applied voltage exceeds a certain of threshold voltage (~ 560 V) at a fixed frequency of 1 kHz. In contrast, no any green light from the sample without ZnO nanowires was founded although the maximum value of the AC voltages (2 kV) was applied on it during our test, which indicates that the ZnO nanowires can enhance the local electric field within the interface of nanowires and phosphor grains. However, the relationship between luminance intensity and applied voltage cannot be repeatedly characterized well because of the stable transparent electrode has not been achieved.

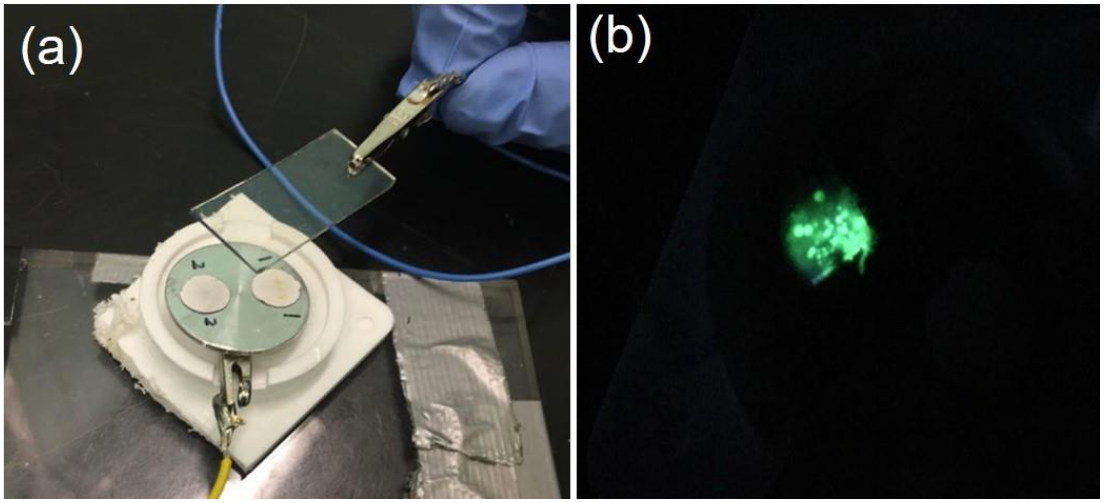


**Figure 4.23** EL measurement of ZnO nanowire-based AC powder EL device. (a) The photograph of the tested EL devices sample; (b) Green-light emission is founded when the ITO glass contacted on the top of the sample after the applied voltage exceeds 560 V.

## 4.2 Fabrication of Hydrothermal-Growth ZnO Nanowire-Based AC Powder EL Device

### 4.2.1 Hydrothermal Synthesis of Vertically Aligned ZnO Nanowire

Zinc oxide nanowire array was synthesized by the hydrothermal process, which is mentioned in section 3.1.1. An ITO-coated glass substrate was consecutively cleaned by sonication in detergent solution, acetone, isopropyl alcohol (IPA), ethanol and deionized (DI) water for 5 min per step, and finally rinsed with DI water and dried with $N_2$ flow. The rectangular pieces (1 cm x 2 cm) of ITO glass are used as conductive and transparent substrates for growth of a vertically aligned ZnO nanowire array through the hydrothermal method. Firstly, zinc acetate solution with a concentration of 12 mmol/L was spun on the top of the clean ITO glass substrate twice to form a uniform ZnO crystal seed layer with a spin speed of 800 rpm. Then the seed layer was annealed at 450 °C for 30 min in order to improve the crystallinity of the ZnO seed layer. Secondly, the ZnO-coated ITO substrate was immersed into a 100 mL of growth solution, which was prepared by thoroughly mixing of 50mmol/L of PEI (polyethyleneimine), 60mmol/L of $Zn(NO_3)_2 \cdot 6H_2O$ and 60 mmol/L HMTA (hexamethylenetetramine). Thirdly, after maintaining the temperature of growth solution at 95 °C for 20 hours, the ITO substrate was taken out from the growth solution and rinsed with DI water every 20 min. Finally, the as-prepared ZnO nanowires grown on the ITO substrate underwent annealing at 200 °C for 30 mins to remove the organic residue.

The length of the nanowire could be tuned by the growth duration. Figure 4.24 shows the SEM results of the nanowires after growth for 4 hours. The length of the nanowire is approximately 1 micron, and the diameter of the nanowire tip is around 25 nm.

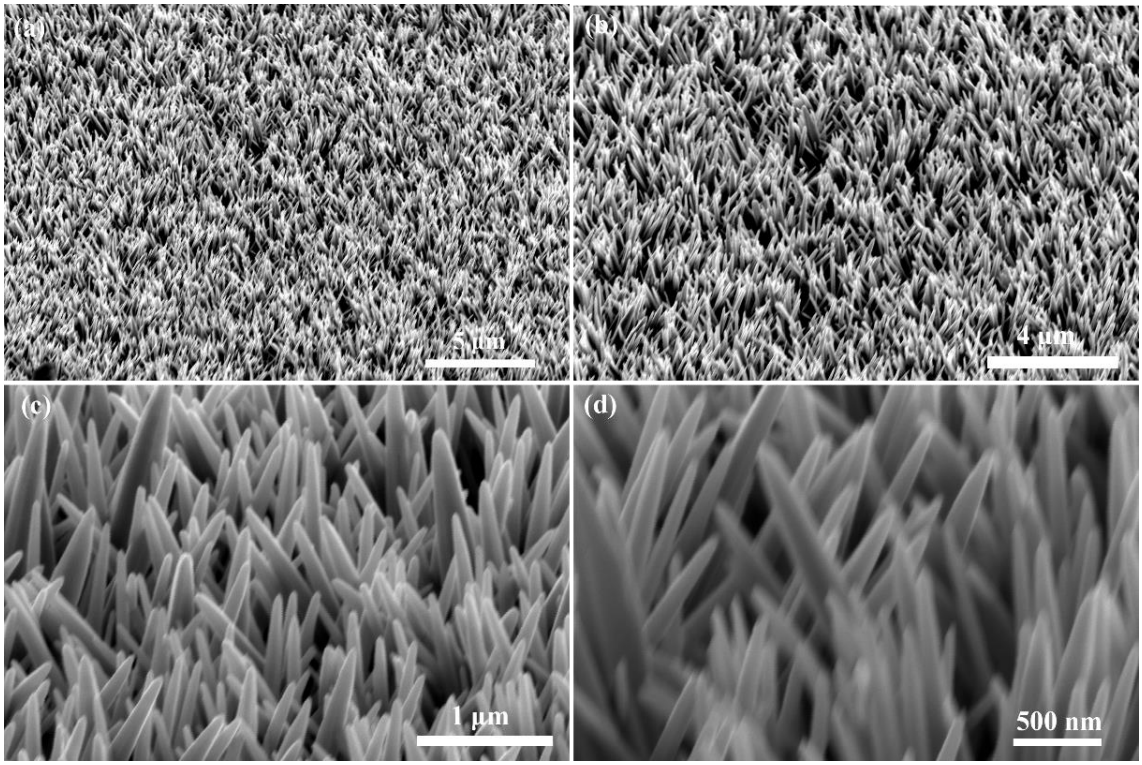


**Figure 4.24** SEM images of the vertically-aligned ZnO nanowires array grown on ITO glass substrate by hydrothermal method for 4 hours.

The length of the nanowires increases to around 5 microns when the growth duration increases. Figure 4.25 shows the SEM result of the same sample having continuous growth for 20 hours. The diameter and the spatial density of the nanowire array almost maintains at the same value, which means the length of the nanowire may be significantly determined by the growth time. Also, the shape of the ZnO nanowires exhibits hexagonal features that implies the preferential growth direction of the nanowire is [0001] when they are synthesized by the hydrothermal method.

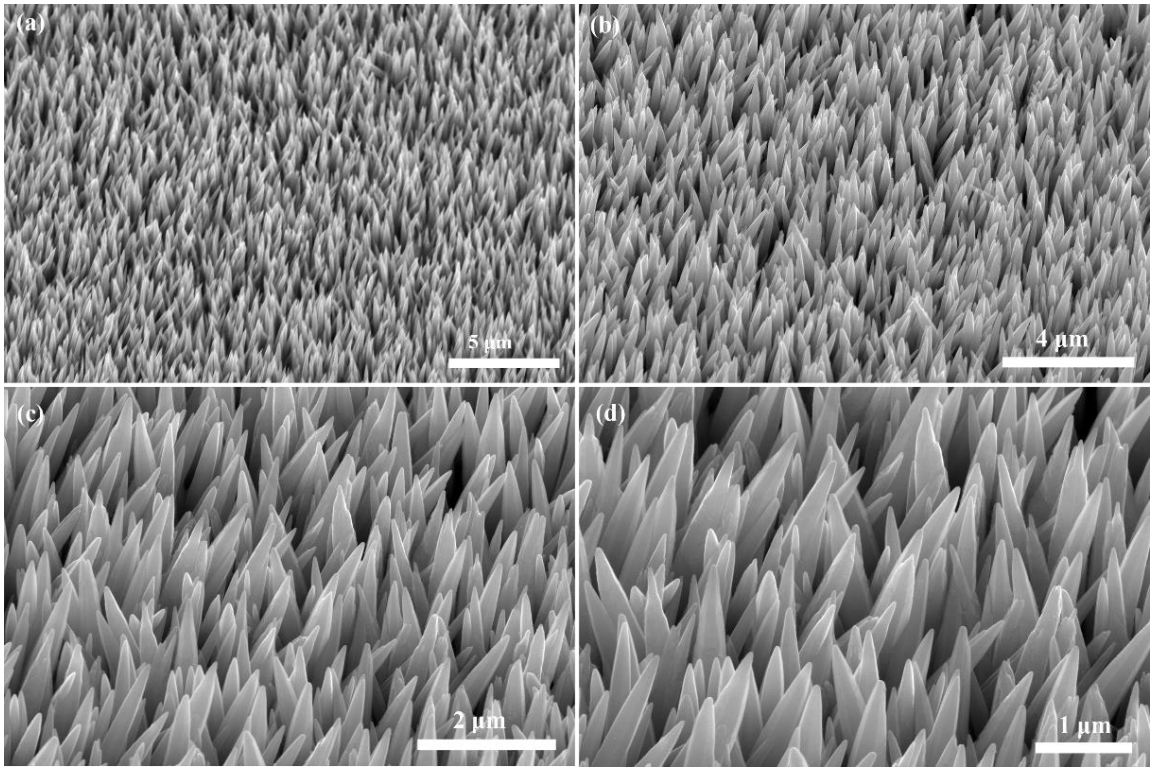


**Figure 4.25** SEM images of the ZnO nanowires array on ITO glass substrate grown by hydrothermal process for 20 hours.

### 4.2.2 Assembly of Hydrothermal-Growth ZnO Nanowire-Based EL Device

An AC powder EL device was fabricated by using the ZnO nanowire array. The nanowires are, ~5 μm in length, as directly synthesized on the ITO glass substrate via the hydrothermal growth process. Figure 4.26 shows the structure of the as-fabricated AC powder EL device, in which a thin layer of phosphor powder, approximately 5 μm in thickness, was deposited on the top of the ZnO nanowire array by drop-coating of the $Zn_2GeO_4$:Mn suspension. Then it was dried in air followed by annealing at 400 °C for 3 hours to improve the contact between the nanowires and phosphor powders. After that, a thin (about 200 μm) sintered $BaTiO_3$ dielectric plate (10 *p*F, Dielectric Laboratories S02BT)

was attached on the phosphor thin layer by using Methylmethacrylate (PMMA, 7 % in Anisole, MICRO CHEM) and dried in air. Finally, a silver paste was applied on the $BaTiO_3$ layer and employed as the back electrode of the EL device.

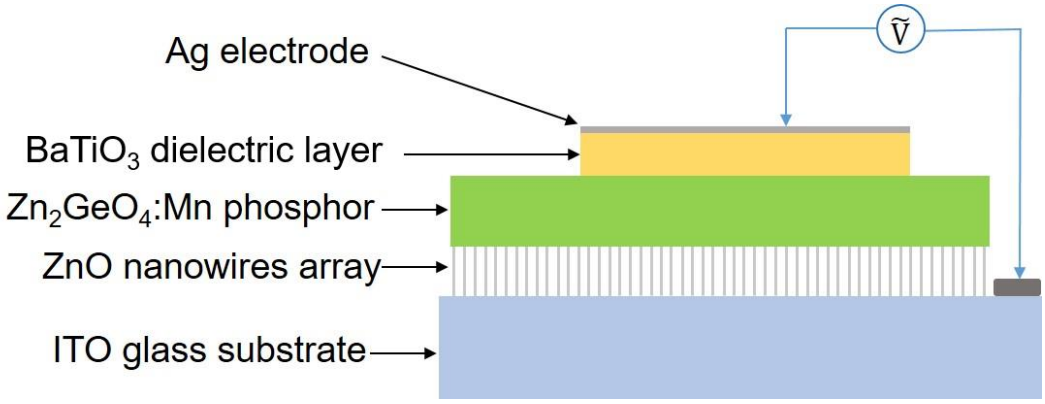


**Figure 4.26** Schematic diagram of the as-fabricated AC powder EL device based on ZnO nanowires array grown by hydrothermal growth.

### 4.2.3 EL Characteristics of Hydrothermal-Growth ZnO Nanowire-Based EL Device

The electroluminescent behavior of the device was characterized when the top and bottom electrodes were connected to an external AC power supply. Figure 4.27 shows the photograph of the electroluminescence phenomenon in the as-fabricated device when the operating AC peak voltage reaches 600 V. It was found that the rectangular lighting area is in accordance to the size of the $BaTiO_3$ dielectric layer. This indicates that the external voltage was applied across the area which is covered by the dielectric layer because of the large dielectric constant of the $BaTiO_3$ dielectric layer.

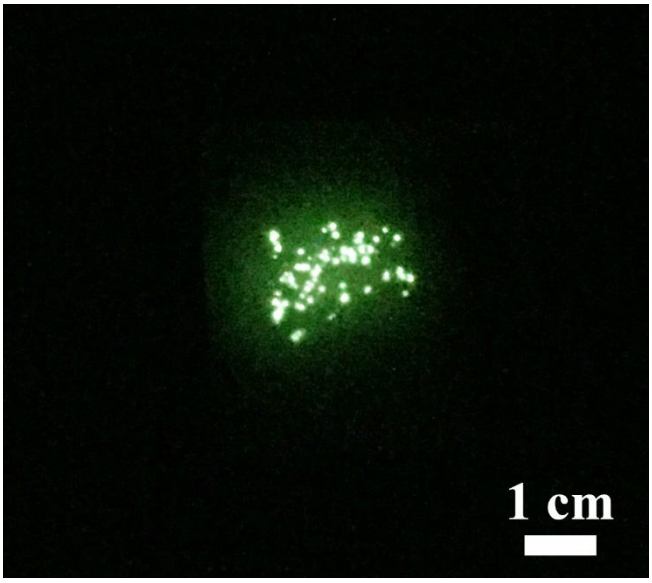


**Figure 4.27** Photograph of the green light emission in the as-fabricated AC powder EL device based on hydrothermal-synthesized ZnO nanowire array when the peak operating AC voltage is 600 V.

The luminescent intensity of the as-fabricated AC powder EL device significantly depends on the operating AC voltage. Figure 4.28 shows the luminescent intensity of the device varies as a function of the operating voltages. The luminescent intensity is monitored while the frequency of the input pulse-waveform AC signal maintains at 5 kHz. The green light emitted from the EL device is found when the AC peak voltage arrives around 400 V, and the luminance intensity exponentially increases as the applied voltages further increase beyond this threshold voltage.

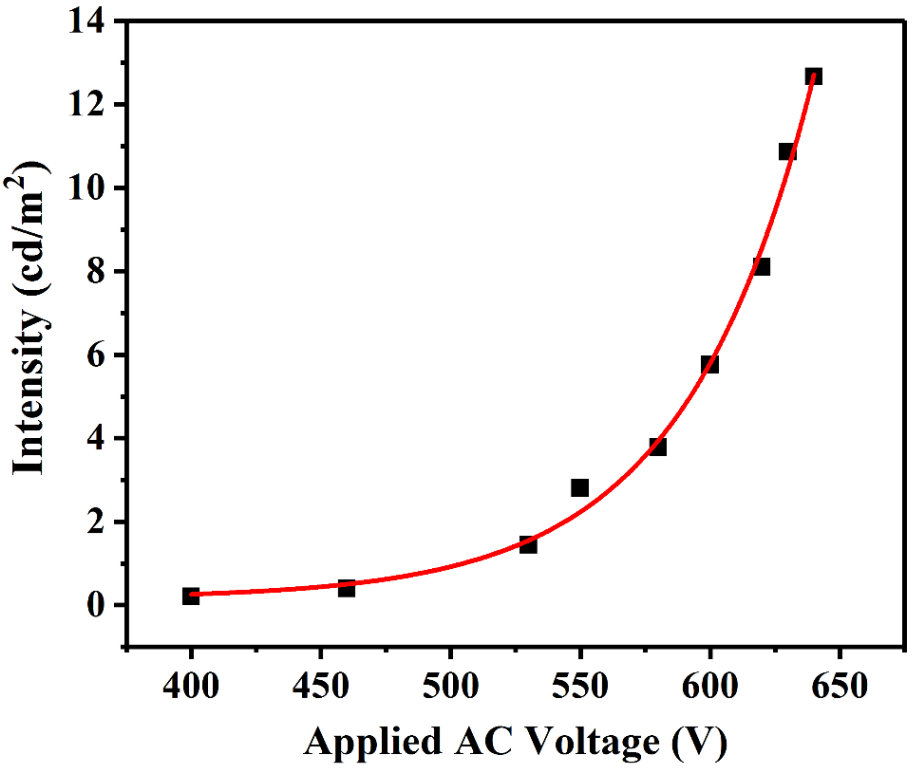


**Figure 4.28** Luminance intensity of the ZnO nanowire-based AC powder EL device as a function of the applied voltage when the frequency of the pulse-like AC signal maintains at 5 kHz.

Figure 4.29 shows the efficiency of the ZnO nanowire-based AC powder EL device as a function of applied bias voltages with maintaining the frequency of the pulse-waveform AC signal at 982 Hz. The maximum luminous efficiency ( $\eta_{max}$ ) could reach 1.31 lm/W at an operating voltage of 550 V. These measurements were repeated three times and the deviation of the efficiency was within 1%. The luminous efficiency is defined as the ratio of the luminescence intensity with power consumption (see section 2.1.7), for example, $\eta=L/P=L/IV$ , where L is luminescence intensity, P is power consumption, V is applied bias voltage, and I is current flowing through the powder EL device. Therefore, the efficiency

largely depends on the current behavior of the device. When the applied bias voltage increased beyond a certain limit of the voltage (550 V in this test), large current flowed in the powder EL device, as a result, the efficiency saturated and reversed, which is accordance to the typical phenomenon of the powder EL devices [52,205].

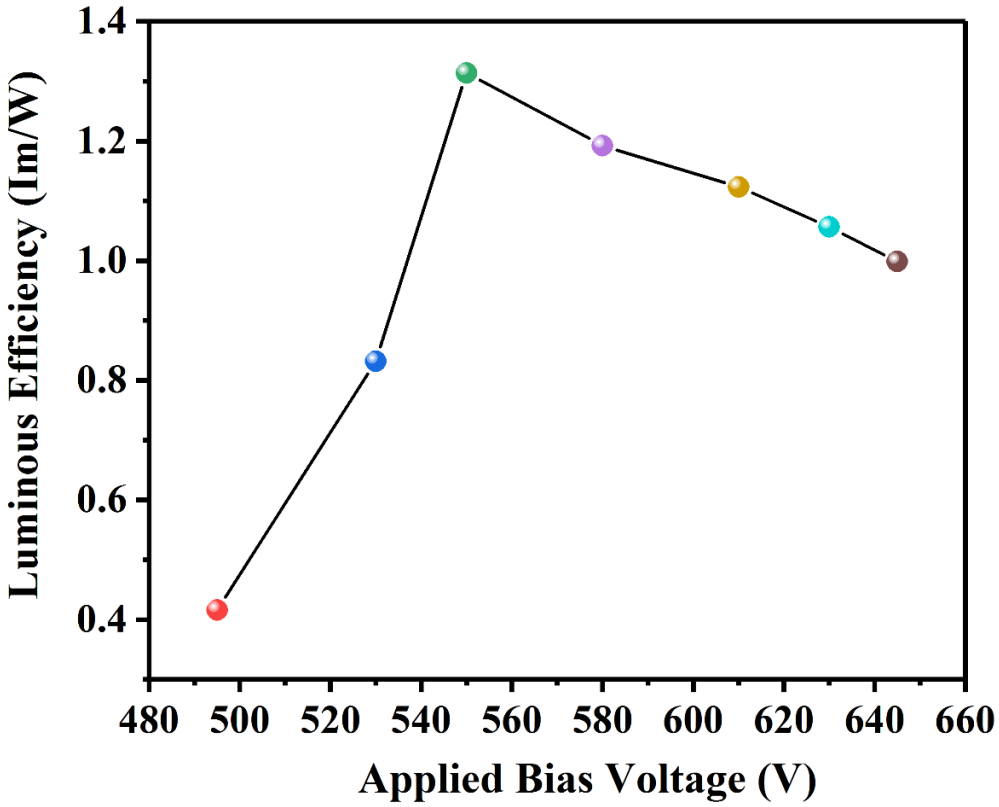


**Figure 4.29** Efficiency of the ZnO nanowire-based AC powder EL device as a function of applied peak AC voltage at a frequency of 982 Hz.

# Chapter 5. CuO Nanowire-Based AC Powder EL Device

## 5.1 Fabrication of CuO Nanowire-Based AC Powder EL Device

For this device, a layer of vertically aligned CuO nanowires was firstly synthesized on a thin Cu plate (purity > 99.9%) by a thermal oxidation method. Secondly, a thin layer of the as-prepared $Zn_2GeO_4$:Mn phosphor powder was drop-coated on the CuO nanowire layer, and subsequently annealed in air. Finally, the composite consisting of CuO nanowires coated with the phosphor powders was sandwiched between top and bottom thin film FTO (fluorine-doped tin oxide) electrodes grown on glass substrates, resulting in accomplishment of the CuO nanowire-enhanced AC powder EL devices.

### 5.1.1 Growth of Vertically Aligned CuO Nanowire Array

A rectangular piece of copper foil (purity > 99.9 %) was cleaned by consecutive sonication in acetone, isopropyl alcohol (IPA), and deionized (DI) water for 5 min each case consecutively, and finally rinsed with DI water and dried with a $N_2$ flow. Then, the foil was immediately transferred into an open furnace. Vertically aligned CuO nanowire arrays were prepared by heating the copper foil in air at 400 °C. Generally, heating the copper foil at 400 °C can produce well-aligned CuO nanowires with diameters in the range of 80−200 nm. The length of nanowires can be controlled by adjustment of the heating time. In our case, the heating time is 3 hours. The annealing procedure was performed as follows: the furnace temperature was raised to the desirable temperature at a rate of 10 °C/min, the sample was kept at this temperature for 3 hours, and finally the furnace was

gradually cooled down to room temperature without opening the furnace, and then samples were removed.

Figure 5.1 shows the scanning electron microscope (SEM) image of the as-grown CuO nanowires. A large-scale, high-density CuO nanowire array is observed. The nanowires have an average diameter of 50 nm and a height of about 5 μm, respectively, with a relatively flat tip.

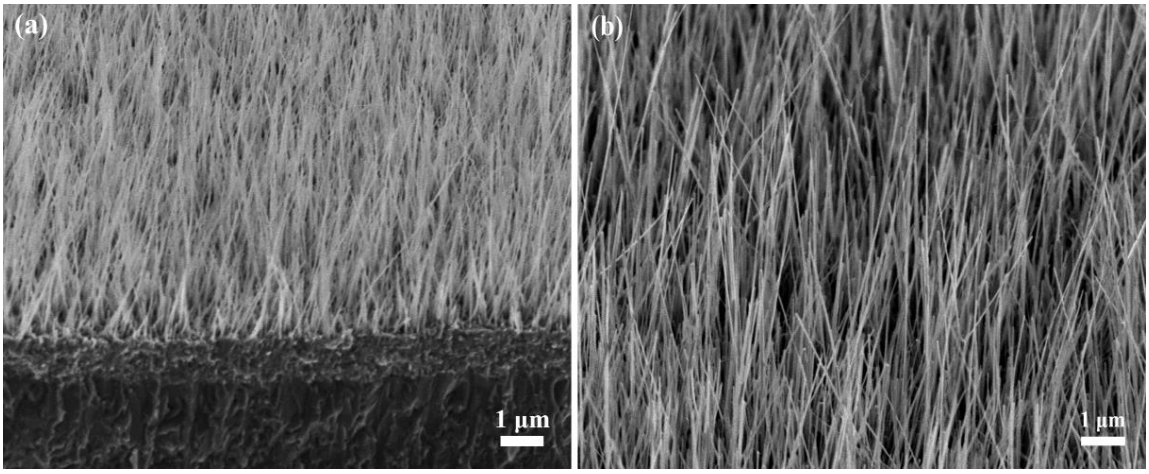


**Figure 5.1** SEM images of the as-synthesized CuO nanowires array on Cu plate by thermal oxidation of Cu foil. (a) Laminate structures of $Cu_2O$ layer, CuO layer and CuO nanowires from bottom to top; (b) High-magnification image of CuO nanowires. The scale bar is 1 μm.

The growth mechanism may be described as 'grain boundary-assisted diffusion growth' [175-185], in which two main steps are involved: (i) a $Cu_2O$ layer forms on the surface of a Cu substrate, serving as the precursor of the CuO growth in the subsequent step; (ii) The CuO nanowires are then formed through rapid and short-circuit diffusion of Cu ions across grain boundaries in the former $Cu_2O$ layer:

$$4Cu + O_2 \rightarrow 2Cu_2O \qquad (5-1)$$

$$2Cu_2O + O_2 \rightarrow 4CuO \qquad (5-2)$$

The structure can be clearly seen from Figure 5.2b showing the three regions: $Cu_2O$, CuO thin layers and CuO nanowire array. The order of copper oxide layers on the Cu substrate can also be explained by the diffusion mechanism in which $Cu_2O$ with higher Cu concentration than the CuO layer is adjacent to the pure Cu substrate. To clarify the spatial distribution of this laminate structure that forms, scanning electron microscope (SEM) combined with energy-dispersive X-ray spectrometer (EDS) analyses were carried out, showing the concentration change of Cu and O elements in the ordered layers (see Figure 5.2), which confirms that the laminated structure is formed during the growth of CuO nanowires.

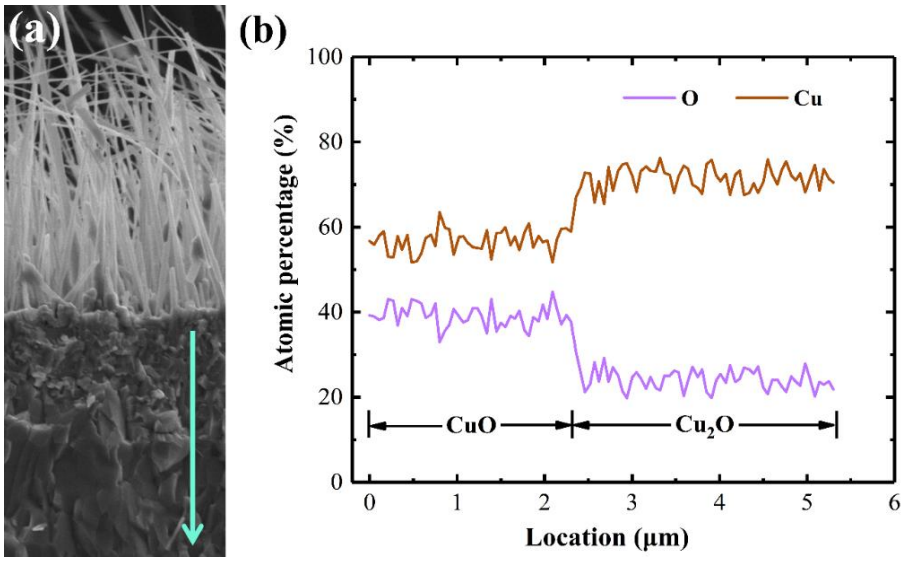


**Figure 5.2** Linear scanning result of EDS. (a) Cross-section SEM image showing the laminate structure of copper oxides formed during thermal oxidation process. They include: CuO nanowires layer, CuO thin layer, and $Cu_2O$ thin layer according to the scanning direction of the arrow. (b) The change of the relative atomic percentage ratio between Cu and O elements following the scanning distance.

In addition, transmission electron microscope (TEM) combined with EDS analysis was used to further investigate the microstructure and crystallography of the grown nanowires (Figure 5.3). The results show that an as-synthesized nanowire has a monoclinic single-crystal structure and that it is pure: only Cu and O elements were detected.

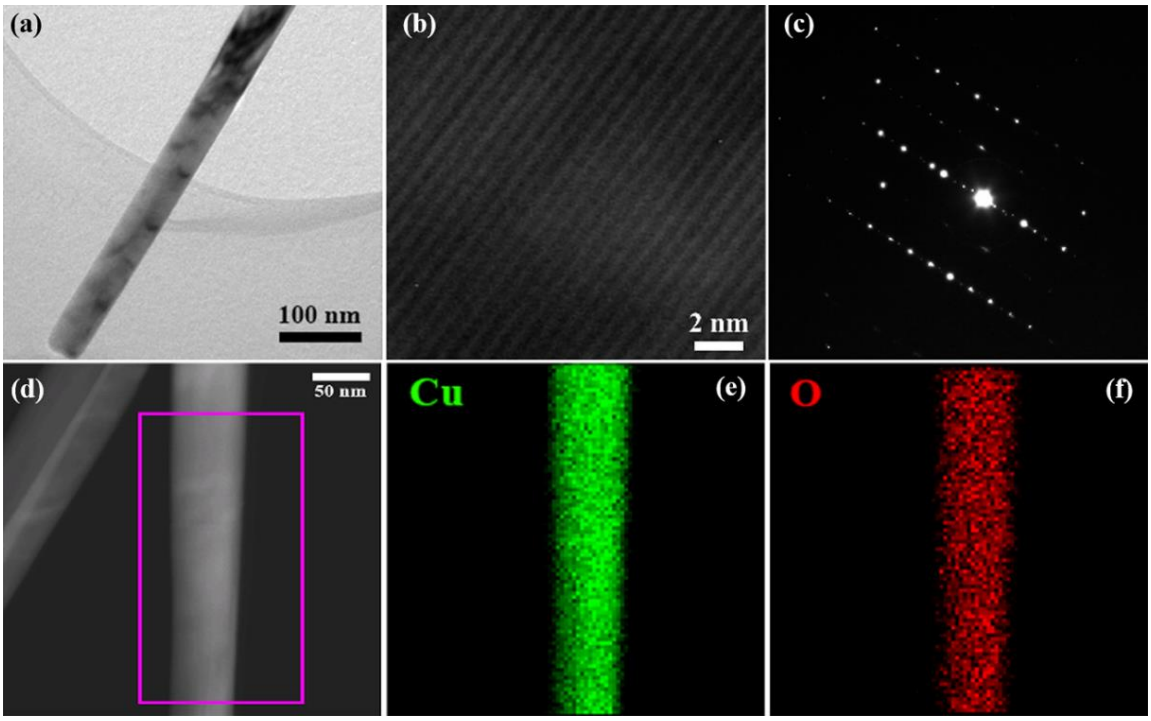


**Figure 5.3** TEM and EDS characterizations of a single as-prepared CuO nanowire. (a) TEM image showing that the CuO nanowire has a diameter of about 60 nm, and (b) High-resolution TEM (HRTEM) image of the nanowire exhibiting the lattice fringe; (c) The corresponding selected-area electron diffraction pattern of the single-crystalline CuO nanowire in (a). The EDS results from a single CuO nanowire in (d) showing that the components within the nanowire is copper in (e) and oxygen in (f).

### 5.1.2 Assembly of CuO Nanowire-Based AC Powder EL Devices

The emission layer of the EL device was prepared by drop-casting of $Zn_2GeO_4$:Mn phosphor powder onto the as-synthesized CuO nanowire array. In particular, the coating solution was made by mixing 0.3 g of $Zn_2GeO_4$:Mn phosphor powder in 30 ml of isopropanol suspension. Then, the mixed suspension was ultra-sonicated for 30 min and stirred for 30 min. Second, the black CuO nanowire sample was placed on a hotplate while maintaining the temperature at 60 °C, and ~ 5 droplets of the mixed suspension were cast on the surface of the CuO nanowire sample. After drying with heat, subsequent identical coating cycles were performed. A uniform coating of $Zn_2GeO_4$:Mn phosphor with an average thickness of 5 μm was formed after repeating the coating cycle 6 times. The color of the sample turned to completely white after drying by heat. Finally, the composite sample was transferred to a furnace and annealed at 400 °C in air for 3 hours in order to acquire the reliably strengthened junctions between the CuO nanowires and the $Zn_2GeO_4$:Mn phosphor particles (see Figure 5.4).

A PMMA binder layer was coated on the annealed CuO nanowire-$Zn_2GeO_4$:Mn phosphor composite by spin coating at a spin rate of 500 rpm for 60 s, and repeating three times. Then, the sample was baked at 100 °C for 2 min, and a fairly stable composite was achieved. After that, the backside of the copper substrate was removed using diluted HF solution. After drying, a PMMA thin layer, ~ 10 μm, was coated on a piece of FTO-coated glass using rod-coating of ~3 μl of PMMA solution (PMMA, 7 % in Anisole, MICRO CHEM). The composite sample was then attached on a piece of FTO-coated glass, with the FTO thin film towards the PMMA layer. After curing in room temperature (25 °C) for 8

hours, the composite was tightly adhered to the FTO glass. Finally, the backside of the copper substrate with an exposed fresh copper surface was connected to the other piece of FTO glass using nickel (Ni) paste.

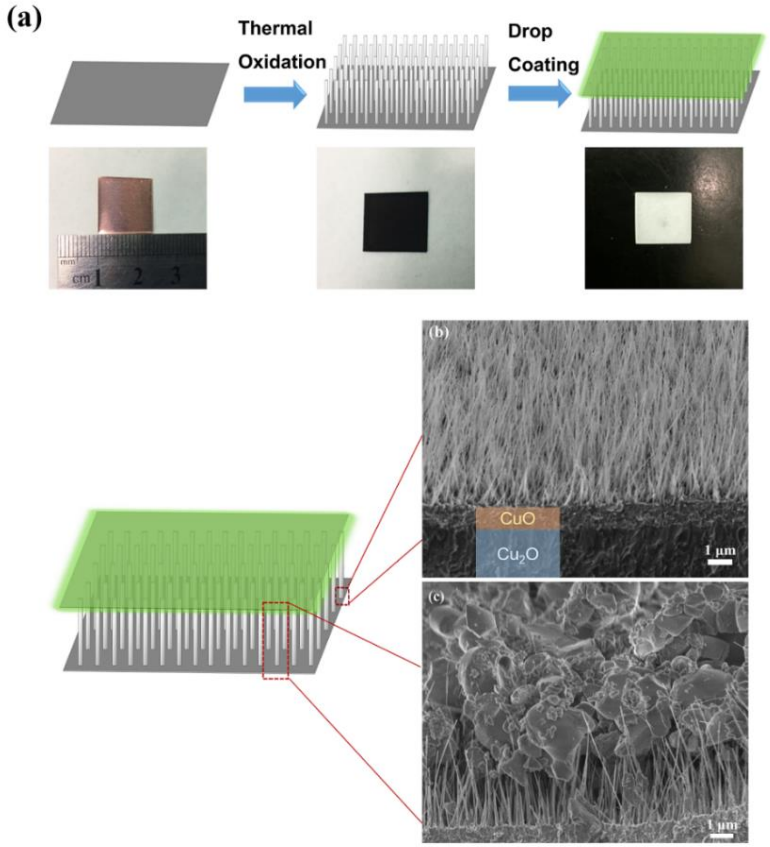


**Figure 5.4** Growth of CuO nanowires by the thermal oxidation of the Cu substrate followed by the formation of CuO nanowire-phosphor heterogeneous junction structure via drop coating method. (a) Flow-chart of the nanowire array grown on Cu substrate, while the corresponding photographs below showing the color change during each step; (b) cross-section SEM image of the vertically aligned CuO nanowires grown on Cu substrate, exhibiting three orderly hierarchic structures including $Cu_2O$ layer, CuO layer and CuO nanowires array from bottom to top; (c) cross-section SEM image showing the heterogeneous junction structure between CuO nanowire and phosphor particles after drop coating followed by annealing at 400 °C for 3 hours.

Figure 5.5a shows a schematic structure of the CuO nanowire-based AC powder EL device by using the aforementioned fabrication method. The image in Figure 5.5b shows

the device with bright green emission with a pulse-waveform AC voltage applied to the nanowire-phosphor structure. The peak-to-peak of the applied voltage is 650 V, and frequency is fixed at 5 kHz.

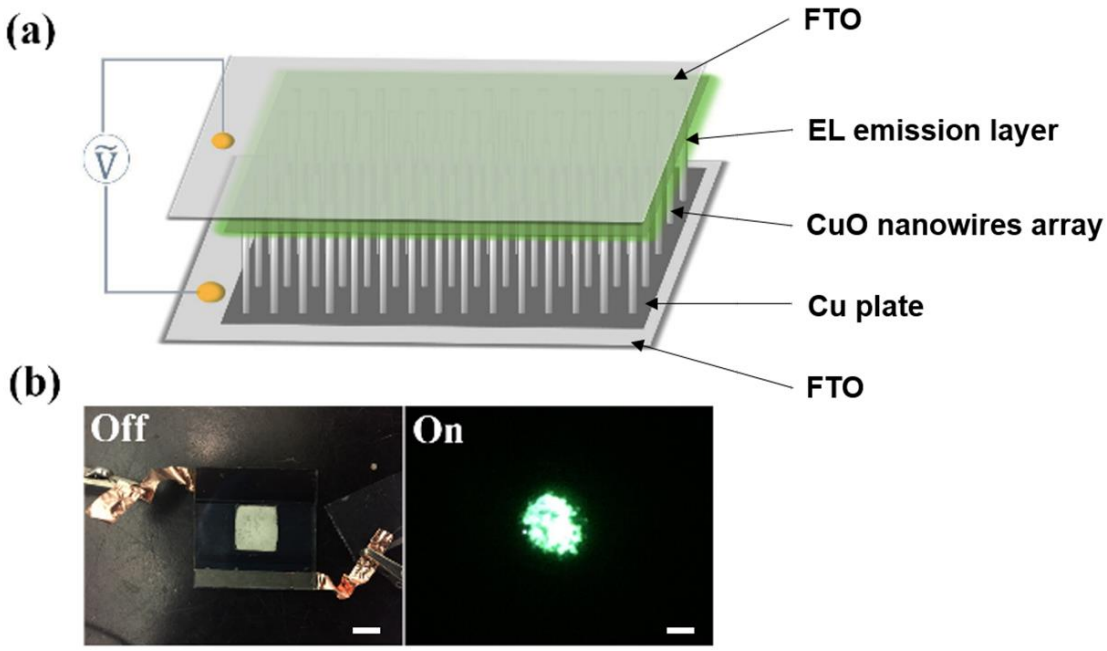


**Figure 5.5** (a) Schematic image showing the device structure. (b) Photographs of the fabricated device in the Off state (left) and On state (right). The scale bar is 1 cm.

## 5.2 Formation of Heterogeneous Junction Structure between CuO Nanowire and Phosphor Particles

Similar to the ZnO nanowire-based AC powder EL devices, the heterogeneous junction between $Zn_2GeO_4$:Mn phosphor particles and vertical CuO nanowire array plays a critical role in producing EL. The junction was formed by a self-assembly process, in which the phosphor particles were drop coated on the nanowire array to form an even particle coating layer with a thickness of about 5 μm, followed by annealing in air at 400 °C. These heterogeneous junctions are revealed by peeling off the phosphor coating layer from the

nanowire arrays carefully as clearly shown in Figure 5.6. Further investigation is needed to clarify details of the junction such as evidence for diffusion and interface formation.

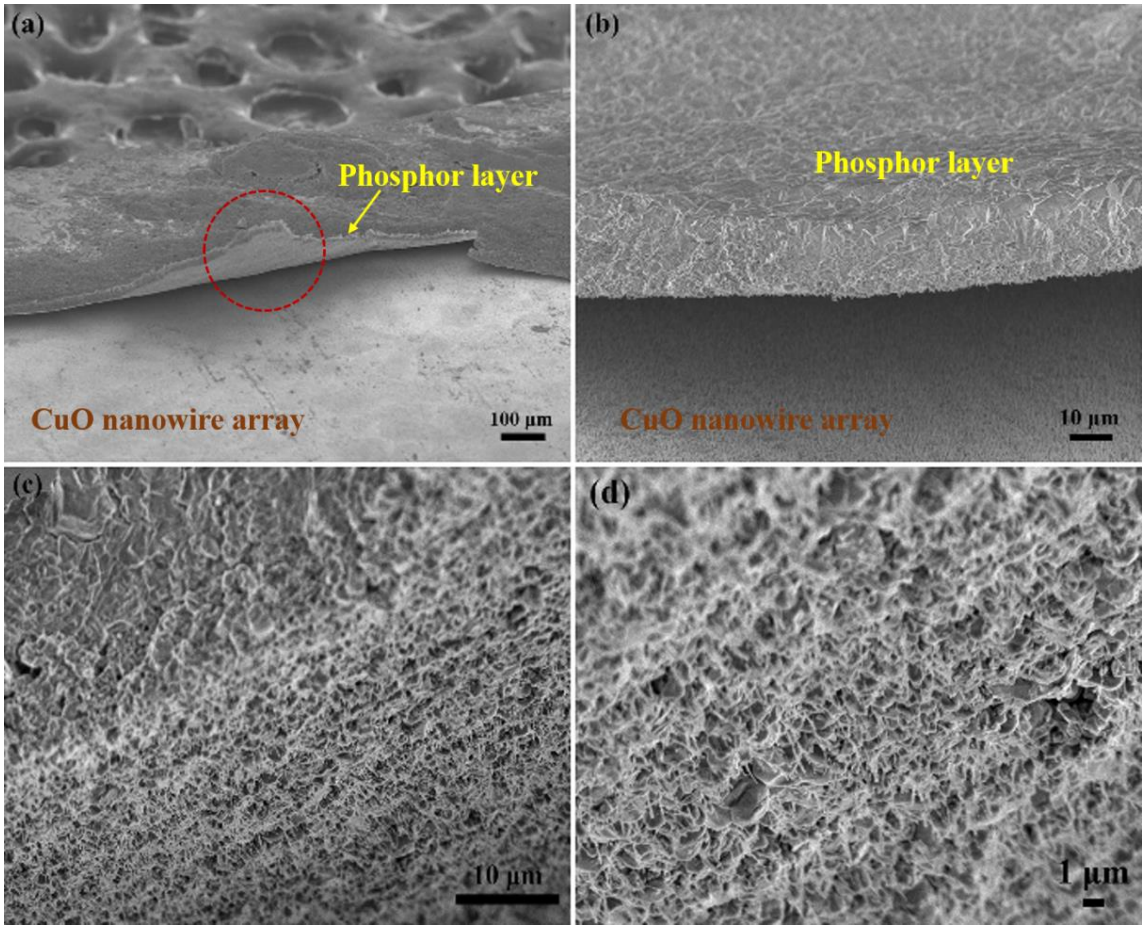


**Figure 5.6** The heterogeneous junction structures between CuO nanowire array and $Zn_2GeO_4$:Mn phosphor powder layer. (a) A curved phosphor layer was partially peeled off from the CuO nanowire arrays underneath; (b) A magnified image exhibiting the particles in phosphor layer and tips of the nanowires; (c) Zoom-in image of the backside of the curved phosphor particle layer clearly shows that the broken tips of CuO nanowires are thermally bonded with the phosphor layer, verifying the reliability of the nanowire-phosphor junctions structures.

In addition, TEM analysis was performed to characterize the heterogeneous junction structures between the CuO nanowire and $Zn_2GeO_4$:Mn phosphor particle in more detail. As shown in Figure 5.7a and 5.7b, a junction structure is formed between a single CuO

nanowire and a $Zn_2GeO_4$:Mn phosphor grain. High-resolution TEM (HRTEM) images of the heterojunction structure revealing the detailed crystal structures are shown in Figure 5.7c and 5.7d. The growth direction of the CuO nanowire was along the [100] crystal orientation, which is a typical growth direction for CuO nanowire synthesized by thermal oxidation method. The $Zn_2GeO_4$:Mn phosphor grain was found to grow along the [001] direction. It is evident that the heterogeneous junction region is free of, for example, an amorphous sheath layer. Also, it was found that a lattice distortion exists within the junction region (see Figure 5.7d). This small lattice mismatch is usually considered to be the main driving force that minimizes the interfacial strain energy. Figure 5.7e and 5.7f show the corresponding fast-Fourier transform (FFT) patterns of the CuO nanowire and $Zn_2GeO_4$:Mn phosphor grain obtained from Figure 5.7d, respectively.

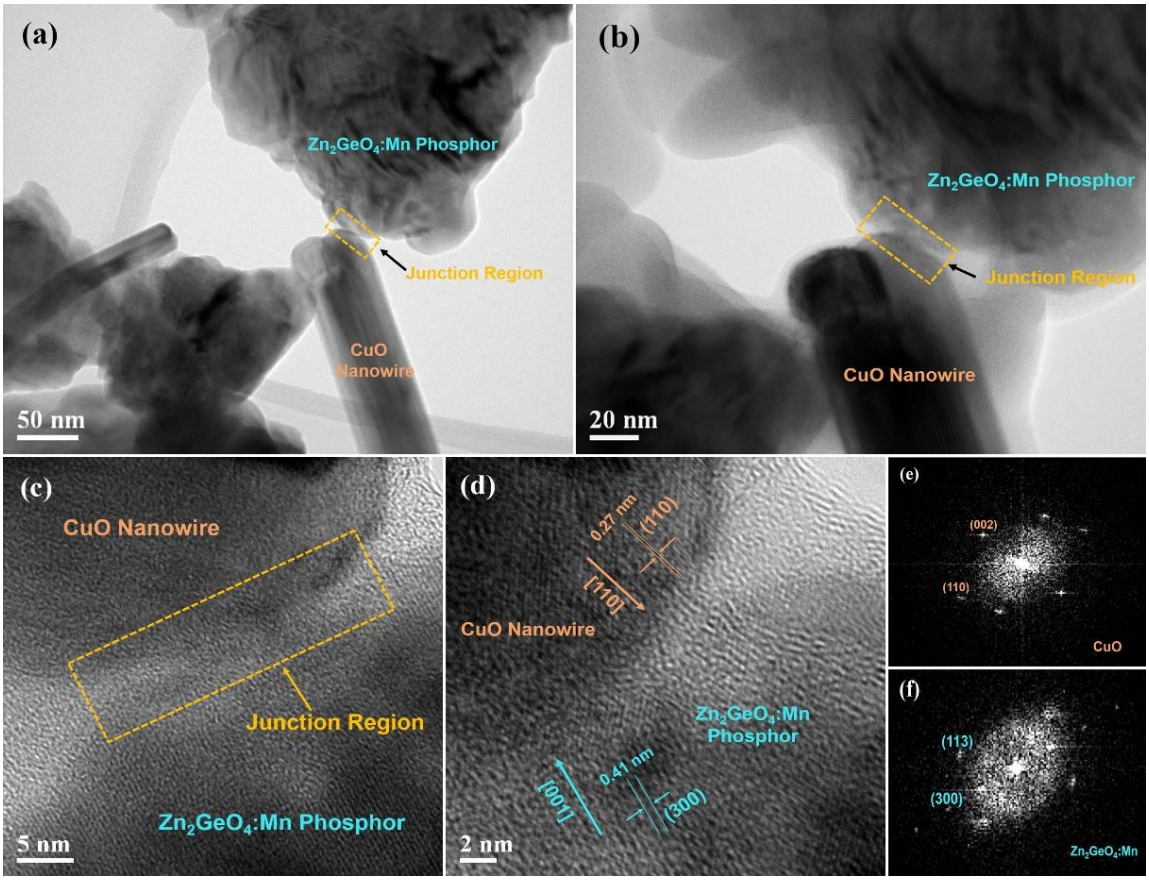


**Figure 5.7** TEM image of the heterogeneous junction structure between CuO nanowire and $Zn_2GeO_4$:Mn phosphor particle. (a) and (b) Low-magnification TEM image of the heterojunction structure. (c) and (d) HRTEM image of the heterojunction structure. (e) and (f) FFT patterns of the CuO nanowire and $Zn_2GeO_4$:Mn phosphor single crystals respectively, obtained from the HRTEM image in part (d).

The stability of the heterogeneous junction structures could be significantly improve by post-annealing process, in which the contacts between the CuO nanowires and their phosphor coating layer becomes more compact and more reliable. Consequently, the purpose of annealing after the drop coating is to facilitate the diffusion of Cu ions from the CuO nanowire tips to the phosphor particle in contact with the phosphor grain. Thus, stable and reliable junctions are formed such that effective carrier injection from the nanowire into the phosphor particle is achieved and carrier injection is increased significantly. It is

also expected that due to the small radius of curvature of the nanowire tips, the copper ions will dominate the diffusion process rather than diffusion of the phosphor atoms. As shown in Figure 5.8, the threshold voltage of the EL device is much lower than that without annealing.

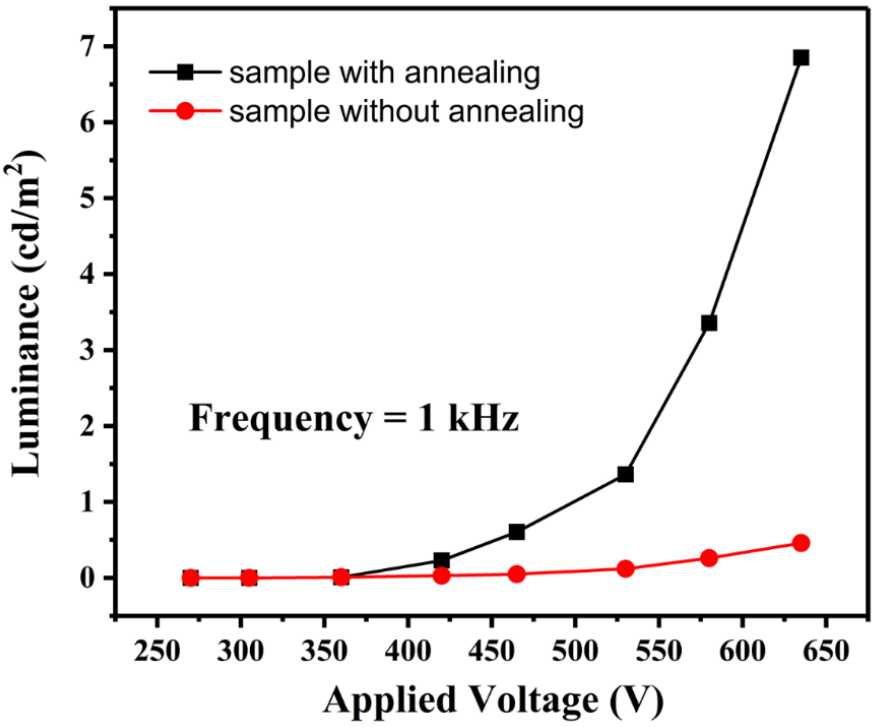


**Figure 5.8** Comparison of brightness as a function of applied voltages between the EL devices with and without annealing treatment. The frequency of the applied pulse-waveform AC voltage is fixed at 1 kHz for both EL device samples.

## 5.3 Finite Element Modelling of CuO Nanowire-Based AC Powder EL Devices

The finite element modelling result of CuO nanowire-based AC powder EL device is illustrated in Figure 5.9, which contains a single CuO nanowire with diameter of 50 nm and height of 2 μm, and a phosphor particle with a thickness of 5 μm and width of 3.5 μm.

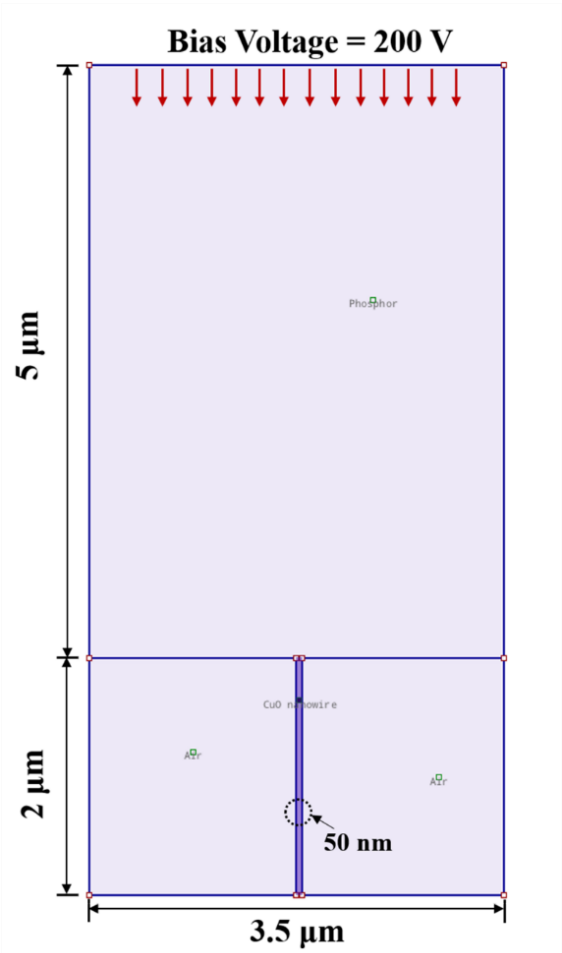


**Figure 5.9** Schematic diagram of the electric-field simulation models of the designed nanowire-based AC powder EL device using Agros 2D 3.2. The simulated region is 3.5 μm x 7 μm in size, upon application of bias voltage of 200 V. The nanowire has the diameter of 50 nm and height of 2 μm, and the phosphor particle is 3.5 μm x 5 μm in size.

By using this model, the field enhancement effect within a CuO nanowire was revealed by two-dimensional static electric field simulations (Agros 2D 3.2), as shown in Figure 5.9. The result apparently indicates that the electric field intensity localized around the junction tip of the nanowire is significantly larger than the other locations within the phosphor particles. In this case, the applied voltage is 200 V between the tip and bottom electrodes, and as a result, the local electric field can be increased from 2.4 x $10^6$ V/m to about 5.0 x $10^8$ V/m, an almost 250-fold enhancement.

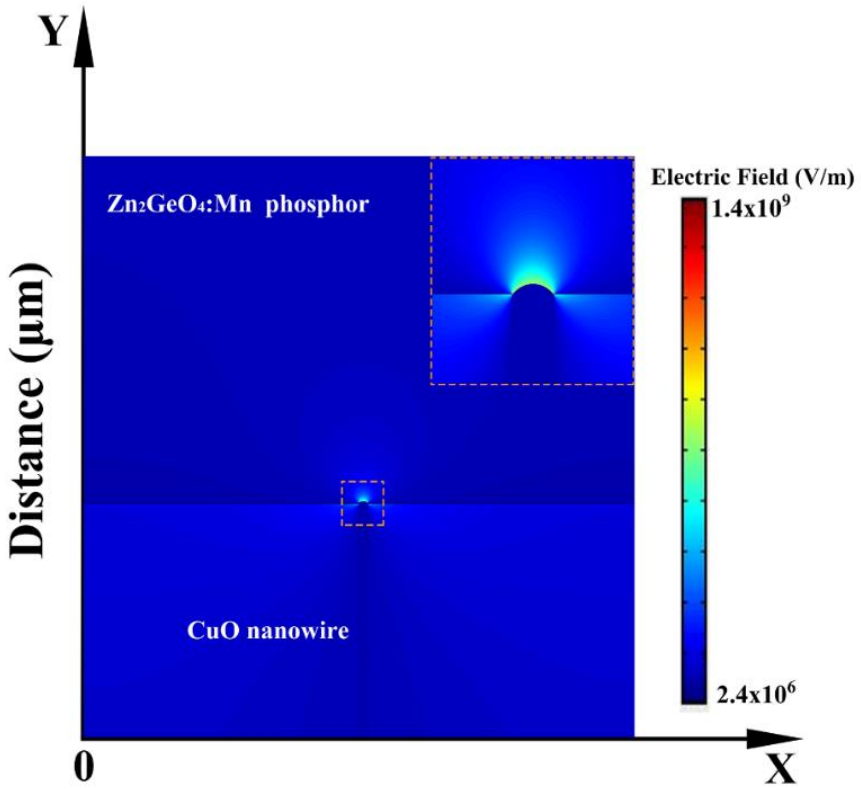


**Figure 5.10** Demonstration of electric-field enhancement effect of CuO nanowire-$Zn_2GeO_4$:Mn phosphor heterogeneous junction. Spatial distribution of the simulated electric field magnitude for $Zn_2GeO_4$:Mn phosphor particle located onto a single CuO nanowire. An enlarged image of the marked rectangular region is shown in the upper-right inset.

## 5.4 EL Characteristics of The CuO Nanowire-Based AC Powder EL Devices

Figure 5.10 shows the EL characteristics of the nanowire-based AC powder EL device. The EL device was powered with a pulsed (pulse width of ~250 μs) AC voltage between the two FTO transparent electrodes. The El emission spectrum was centered at 535 nm with FWHM (full width at half maximum) of 70 nm, as presented in Figure 5.10a, while the inset image of Figure 5.10a shows the Commission International de L'Eclairage (CIE) color coordinate of the emitted light from the top window of the EL device. It is known that the charge carriers are accelerated to high energy under electric field excitation. These hot carriers are injected into $Mn^{2+}$-doped $Zn_2GeO_4$ phosphor particles and cause excitation or impact ionization of the luminescent center ($Mn^{2+}$ ion) in the phosphor, resulting in green light emission during the radiative relaxation of the luminescent center. The luminance intensity versus the applied AC voltage under different frequencies is depicted in Figure 5.10b. The device initiated light emission at the peak voltage of around 350 V, after which the luminance intensity increases quickly as the applied voltage further increases. The observed dependence of the luminescent intensity on the applied bias voltage can be evaluated by the following equation [206]:

$$L = L_0 \exp(-\beta/V) \tag{5–3}$$

where L is the luminance, V is the applied voltage, and $L_0$ and β are the constants determined by the devices. After increasing to a certain voltage value, the probability that electrons are accelerated to a given energy and subsequently excite (or ionize) the luminescent centers will increase rapidly, corresponding to the rapid increase in the

luminance. The fitting curve in Figure 5.10b indicates that the experimental result agrees well with equation 5-3 as bias voltage increases. The luminance-voltage relationship presented here is different from the ZnS:Cu powder EL devices reported by other groups. In their work, the relation between the EL emission intensity and the applied bias voltage follows the equation: $L = L_0 \exp(-\beta/V^{1/2})$ [3,7]. In ZnS:Cu powder EL devices, the directions of the $Cu_{2-x}S$ precipitates are random with respect to the direction of applied electric field. In addition, the aspect ratio of the $Cu_{2-x}S$ precipitate, which is defined as $R_a = L/D$ where L is the length and D is the diameter of the precipitate, is highly variable from grain to grain in ZnS powder. However, the CuO nanowire array synthesized in our work is substantially aligned with respect to the direction of the applied electric field, and most of the nanowires have a similar aspect ratio. This explains the simple exponential relationship in our case. The AC powder EL device demonstrated in this work relies on capacitance to couple to the external voltage and the emission intensity is determined by the applied voltage rather than a current in the case of p-n junction LEDs devices. On the other hand, when the applied frequency increases, the number of acceleration events per second increases correspondingly and as a result, the observed luminance increases approximately linearly with frequency. The relation between the applied frequency and EL intensity is presented in Figure 5.10c, at a fixed the bias voltage of 420 V. In our measurements, the increase in luminance did not shown any sign of saturation with the increase in voltage or frequency within the measurement range. The EL device using oxide-phosphor powders shows excellent stability, as shown in Figure 5.10d. There is under 1 % loss of luminescent intensity after 15 days (equal to 360 hours) when a luminance of

approximate 10.6 cd/m$^2$ is maintained. This remarkable stability relies on the good chemical stability of oxide phosphor powders and effective chemically bonded heterogeneous junctions between the phosphor particles and CuO nanowire array (see Figure 5.7).

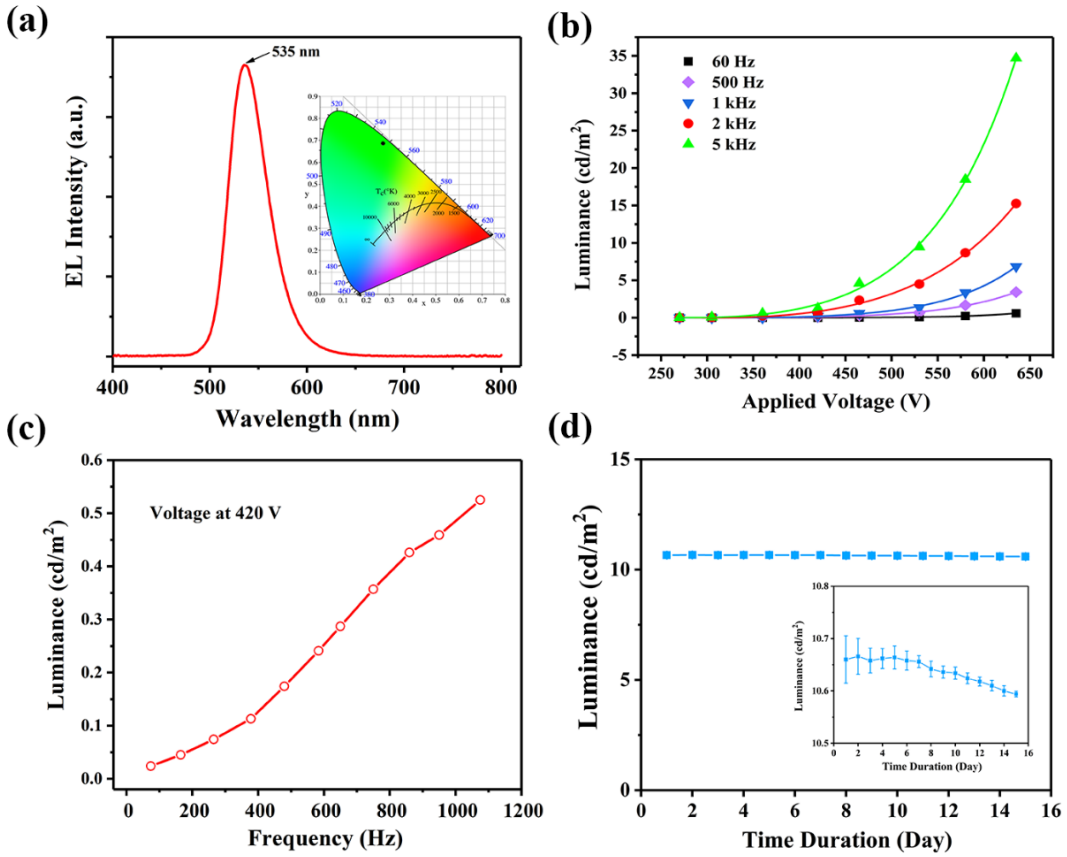


**Figure 5.11** EL characteristics of CuO nanowire-based AC powder EL devices. (a) Electroluminescent spectrum of the CuO nanowire-based EL device. The inset is the color space chromaticity diagram showing CIE coordinate of light emission from the EL device. (b) Luminance of the CuO nanowire-based EL device under various frequencies and the fitting of luminance as a function of applied voltage under various frequencies. (c) Luminescence intensity response as a function of frequency at applied voltage of 420 V. (d) Emission intensity-operation time plot of the CuO nanowire-based EL device. The inset diagram shows the detailed luminance versus operating time characteristics.

The luminous efficiency of the CuO nanowire-based AC powder EL device as a function of applied AC voltage is shown in Figure 5.12. A pulse-waveform AC signal while maintaining a frequency of 1 kHz was used as the electric-field drive source. The maximum luminous efficiency reaches to approximately 1.53 Im/W.

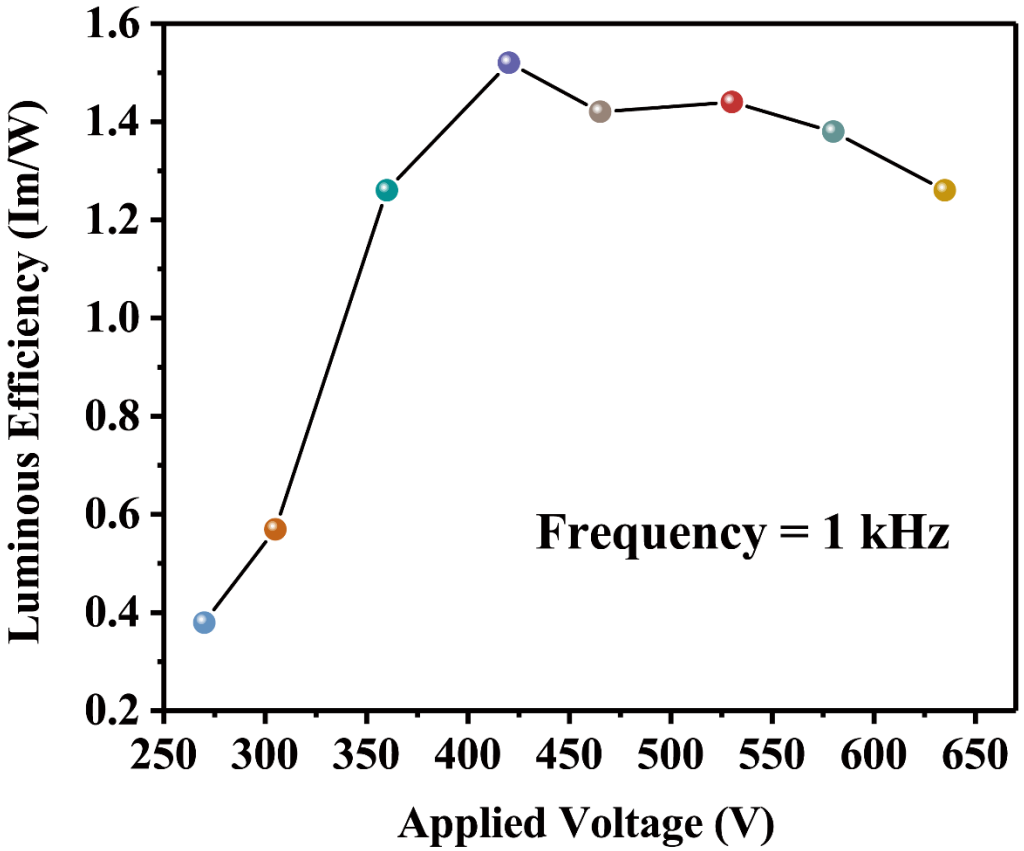


**Figure 5. 12** Luminous efficiency of the CuO nanowire-based AC powder EL device as a function of applied pulse-waveform AC voltage at a frequency of 1 kHz.

The field enhancement effect produced by a CuO nanowire could be illustrated using the band diagram in Figure 5.13. Under the consideration of the Fermi level of a CuO nanowire and the band bending by the local electric field enhancement, the tunneling barrier thickness becomes thin enough to inject electrons from the conduction band of the

CuO nanowire to the conduction band of the phosphor. Then the injected electrons are accelerated by the high electric field and excite the $Mn^{2+}$ luminescent centers by an impact excitation effect. EL emission occurs when the excited luminescent centers undergo radiative transitions to their ground states. Therefore, the role of CuO nanowires could be understood as i) making the high concentration of carriers from the CuO available for injection; ii) by offering junction pathways between nanowire and phosphor particle, and iii) simultaneously providing significant local field enhancement enabling electron injection to the luminescent centers of phosphor. The combination of nanowire density and field enhancement therefore leads to more impact excitation between the luminescent centers and electrons at a relatively low bias voltage. Thanks to the vertically aligned CuO nanowire architecture, EL emission from the $Zn_2GeO_4$:Mn phosphor in achieved under an unprecedentedly low bias voltage and frequency for the first time. No EL emission is observed from the AC powder EL device if the CuO nanowire array is omitted in our device structure.

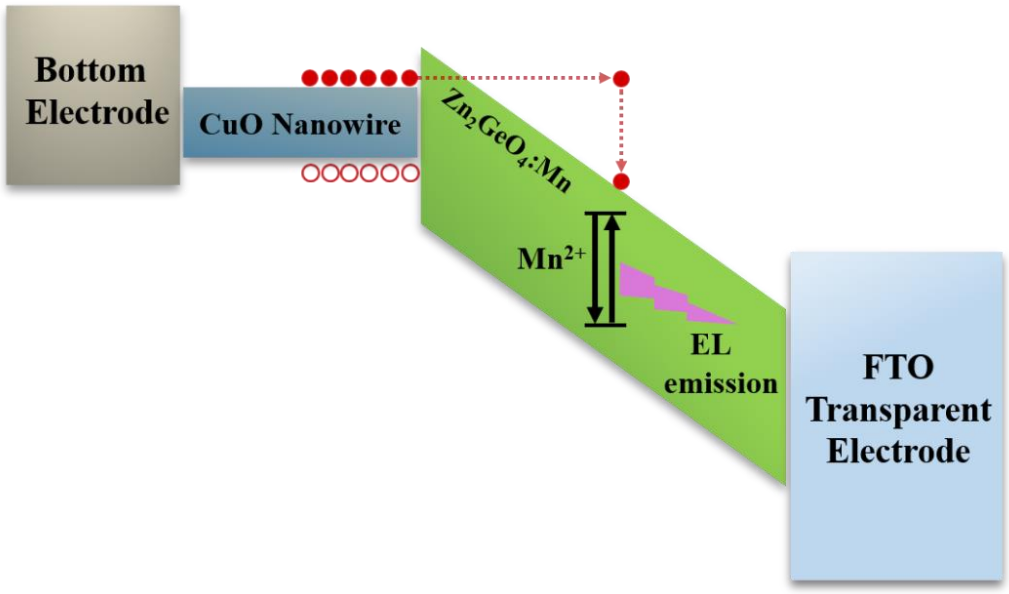


**Figure 5.13** Band structure diagram showing the EL emission mechanism caused by impact-excitation of $Mn^{2+}$ ion in $Zn_2GeO_4$:Mn phosphor, enhanced by CuO nanowire.

It is worth noting that powder EL devices generally require a high dielectric constant layer such as a polymer-barium titanate composite ($\varepsilon_r$ >1000) in order to prevent catastrophic breakdown of the phosphor. A notable aspect of the CuO nanowire-based EL device design is that it does not require a layer with high dielectric constant to prevent catastrophic breakdown of the phosphor. This is because the field enhancement leading to avalanche breakdown is highly localized at around of the nanowire tip and the thick-powder phosphor layer acts as its own dielectric layer, which can therefore render charge regulation and prevent catastrophic breakdown.

# Chapter 6. Conclusion

New types of AC powder EL devices have been achieved by constructing reliable heterogeneous junction architectures between semiconductor nanowires and phosphor powder. The high aspect ratio of the nanowires can enhance the local electric field which results in electroluminescence of the oxide phosphor in the EL devices due to field injection at the nanowire tips.

*n*-type ZnO nanowires were used for electric field enhancement. A sintered $Zn_2GeO_4$:Mn polycrystalline substrate was prepared and the densification process was studied. Then a vertically-aligned ZnO nanowire array was grown on the $Zn_2GeO_4$:Mn polycrystalline substrate via a CVD method. The growth behavior of the nanowire array follows the VLS mechanism, in which the spatial density and size of the nanowires significantly depend on the density and size of the Au catalyst nanoparticles on the $Zn_2GeO_4$:Mn polycrystalline substrate. In addition, it was also proved that the spatial density of the nanowire array can be tailored by tuning the distance between the $Zn_2GeO_4$:Mn substrate and the CVD source powder during the CVD growth process. At the same time, the result in this work shows that the morphology of the CVD-growth ZnO nanowires is also influenced by the oxygen gas flow, the gold catalyst layer, and the source powder material during the growth process. The density-controlled growth of the ZnO nanowire array on the $Zn_2GeO_4$:Mn polycrystalline substrate is realized in this work and the simulation results support that the enhancement effect of local electrical-field varies

with the spatial density of the nanowire array. Finally, this nanowire-phosphor composite was used to fabricate the top-emission AC powder EL device. A bright light emission was found in this EL device when the applied voltage using an ITO-glass top electrode was beyond a threshold value of ~ 560 V, however, the final EL device with an integrated top electrode has not completed yet due to the technique limit on preparation of this top electrode.

On the other hand, a vertically-aligned ZnO nanowire array was synthesized on ITO-coated glass substrate by the aqueous hydrothermal method. The length of the nanowire can be adjusted from 1 μm to around 5 μm by increasing the growth duration from 4 hours to 20 hours. The heterogeneous junction structures between the ZnO nanowire array and $Zn_2GeO_4$:Mn phosphor powder were formed by drop casting of the phosphor suspension on the nanowire array followed by an annealing process. Based on the reliable heterogeneous junction structure, a bottom-emission AC powder EL device was fabricated successfully. The EL performance shows that the luminescence intensity of the ZnO nanowire-based EL device exponentially raises with increasing applied voltage when the voltage exceeds a threshold voltage of ~ 400 V. In addition, the luminescence efficiency of the device reaches 1.31 lm/W when the applied peak voltage was 550 V.

In contrast, vertically-aligned *p*-type CuO nanowire array grown on a Cu substrate were synthesized by a thermal oxidation method. The synthesis process was accomplished by maintaining the growth temperature at 400 °C for 3 hours. By drop-casting of $Zn_2GeO_4$:Mn phosphor suspension on the top of the CuO nanowire array and subsequent post-annealing, a stable heterogeneous junction structure formed and was employed as an electric field-

enhancement architecture in fabrication of highly stable AC powder EL devices. The CuO nanowire-based AC powder EL device shows a good brightness maintenance with a loss of luminescent intensity under 1 % at over 10 cd/$m^2$ luminance over 360 hours of operation. In addition, a highest luminance intensity (~ 35 cd/$cm^2$) was achieved for the first time in an AC powder EL device based on $Zn_2GeO_4$:Mn phosphor.

In summary, the remarkable stability of the oxide-phosphor EL device and the simplicity of the device fabrication provide the prospect to eliminate the inherent degradation problem in traditional sulfide-based AC powder EL devices. In addition, because the growths of ZnO and CuO nanowire arrays are not limited by the morphology and size of the substrate, the proposed approach will further extend to fabricate large-scale EL devices for industrial applications. Our results offer a novel design strategy for both AC-driven lighting and displays. Meanwhile, further development of device performance can be expected by optimizing the phosphor layer thickness, junction structure, or incorporating other oxide phosphors. Other oxide-based phosphor powders could be used to produce emission in red and blue colors, which could provide the other two primary colors for full-color display applications. In addition, the nanowire-based EL device can also be patterned by further developing the drop coating method. For example, suitable masking and patterning methods and/or screen printing methods could pattern the powder phosphors onto the nanowire array at low cost.

# Chapter 7. Future Work

Our work has clearly demonstrated that the performance of AC powder EL device can be largely improved by taking advantage of field-enhancement effect of semiconductor nanowire architecture in the structure of traditional AC powder EL device. Therefore, formation of reliable heterogeneous junction structure between the nanowire and phosphor powder is essential to achieve a high-performance AC powder EL device. However, the formation mechanism of the heterogeneous junction structure has not clearly yet and it is highly desirable to be further investigated in the future. Meanwhile, luminescent efficiency of the CuO nanowire-based AC powder EL device has not been measured, thus, the luminescent efficiency of the device will be measured in the near future. In addition, the novel structures of the nanowire-based AC powder EL devices presented in this research have great potential to be exploited and expended by using other colorful phosphor powders so that full-color EL display devices could be expected.

On the other hand, flexible AC powder EL devices with low processing costs and mechanical flexibility become more and more popular in many applications such as liquid-crystal display, curved back-lighting, and large-scale architectural lighting. In the future, a flexible CuO nanowire-based AC powder EL device might be created by following the technique proposed below.

As shown in Figure 7.1, a CuO nanowire array is directly grown on a thin and flexible Cu foil substrate by a thermal oxidation method. A thin layer consisting of phosphor

powders is coated on the top of CuO nanowires array by a sedimentation method because the Cu thin foil may be bent after thermal oxidation. As a result, the heterogeneous contact structures between the nanowire and phosphor microparticles may be formed. The stability of the heterogeneous contact can be significantly enhanced by annealing the nanowire-phosphor composite at an appropriate temperature. Then the surface of the phosphor may be spin-coated with a thin layer of flexible epoxy or polydimethylsiloxane (PDMS). This polymer thin layer has two functions: 1) to protect the phosphor particles; 2) function as an adhesive to bond the nanowire/phosphor composite to a transparent electrode. Due to the requirement of flexibility in this proposed prototype device, a potential approach could be adopted to fabricate a front transparent and flexible electrode on the composite: 1) to rod-coat or spin-coat Ag nanowires solution onto the surface of the thin polymer layer (either flexible epoxy or PDMS) followed by annealing at a proper temperature; 2) to attach the nanowire/phosphor composite with the polymer cover onto a piece of ITO-PET film. Finally, a bottom electrode could be made by applying some silver paste to the backside of the Cu thin film. As a result, light emission may occur when both the front and bottom electrodes are connected to external AC applied bias voltage.

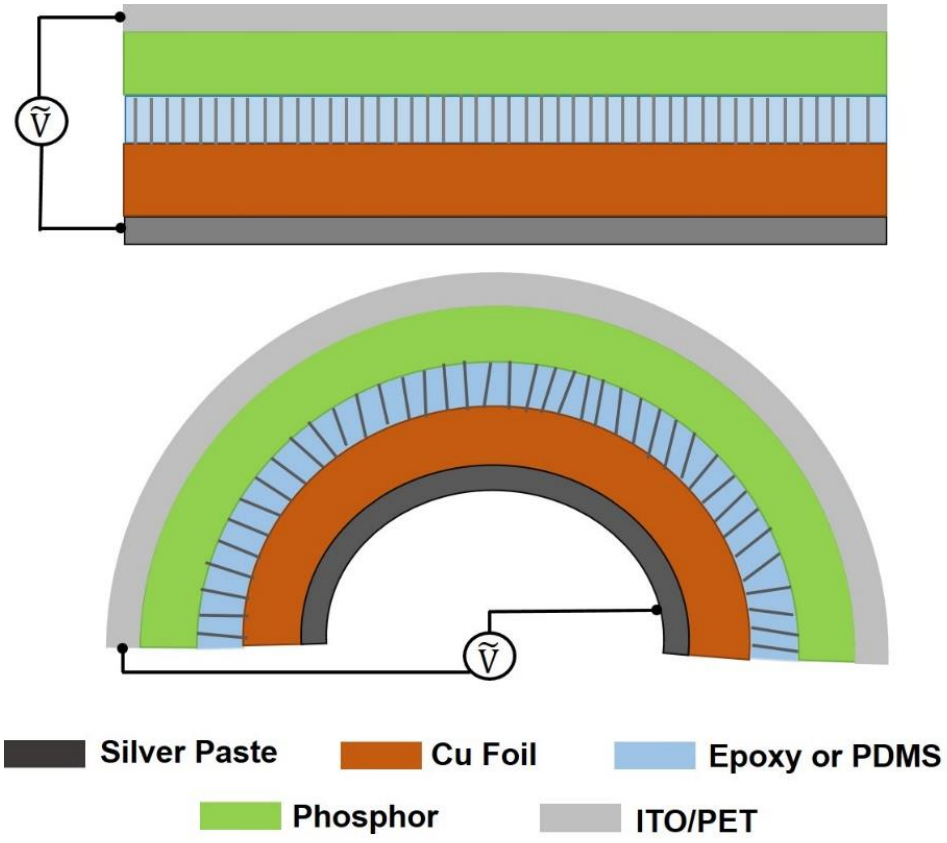


**Figure 7.1** Schematic structures of the proposed flexible AC powder EL device based on CuO nanowires.

# References

[1] G. Destriau, Experimental research on the action of an electric field on phosphorescent sulfides, *J. de Chimie. Physique*, 34 (1937) 117-124.

[2] A. H. Kitai, *Luminescent Materials and Applications*. New York: John Wiley & Sons Inc., 2008.

[3] L. Wen, N. Liu, S. Wang, H. Zhang, W. Zhao, Z. Yang, Y. Wang, J. Su, L. Li, F. Long, Z. Zou, Y. Gao, Enhancing light emission in flexible AC electroluminescent devices by tetrapod-like zinc oxide whiskers, *Opt. Express*, 24 (2016) 23419-23428.

[4] S. H. Cho, S. S. Jo, I. Hwang, J. Sung, J. Seo, S. H. Jung, I. Bae, J. R. Choi, H. Cho, T. Lee, J. K. Lee, T. W. Lee, C. Park. Extremely Bright Full Color Alternating Current Electroluminescence of Solution-Blended Fluorescent Polymers with Self-Assembled Block Copolymer Micelles, *ACS Nano*, 7 (2013) 10809-10817.

[5] C. H. Yang, B. Chen, J. Zhou, Y. M. Chen, Z. Suo, Electroluminescence of Giant Stretchability, *Adv. Mater.*, 28 (2016) 4480-4484.

[6] F. H. Wang, K. F. Chen, Y. H. Chien, C. C. Chang, M. Y. Chuang, Enhanced luminance for inorganic electroluminescent devices with a charged electret, *J. Lumin.*, 141 (2013) 106-110.

[7] J. Wang, C. Yan, G. Cai, M. Cui, A. Lee-Sie Eh, P. See Lee, Extremely Stretchable Electroluminescent Devices with Ionic Conductors, *Adv. Mater.*, 28 (2016) 4490-4496.

[8] C. Schrage, S. Kaskel, Flexible and transparent SWCNT electrodes for alternating current electroluminescence devices, *ACS Appl. Mater. Interfaces*, 1 (2009) 1640-1644.

[9] Z. Wang, Y. Chen, P. Li, X. Hao, J. Liu, R. Huang, Y. Li, Flexible graphene-based electroluminescent devices, *ACS Nano*, 5 (2011) 7149-7154.

[10] G. Liang, H. Hu, L. Liao, Y. He, C. Ye, Highly flexible and bright electroluminescent devices based on Ag nanowire electrodes and top-emission structure, *Adv. Electron. Mater.*, 3 (2017) 1600535.

[11] J. Wang, C. Yan, K. J. Chee, P. S. Lee, Highly stretchable and self-deformable alternating current electroluminescent devices, *Adv. Mater.*, 27 (2015) 2876-2882.

[12] H. Takashima, K. Shimada, N. Miura, T. Katsumata, Y. Inaguma, K. Ueda, M. Itoh, Low-driving-voltage electroluminescence in perovskite films, *Adv. Mater.*, 21 (2009) 3699-3702.

[13] S. Ma, A. H. Kitai, Chemical vapor deposition-based growth of aligned ZnO nanowires on polycrystalline $Zn_2GeO_4$:Mn substrates, *J. Mater. Sci.*, 52 (2017) 9324-9334.

[14] M. Warkentin, F. Bridges, S. A. Carter, M. Anderson, Electroluminescence materials ZnS:Cu,Cl and ZnS:Cu,Mn,Cl studied by EXAFS spectroscopy, *Phys. Rev. B*, 75 (2007) 075301.

[15] A. G. Fischer, Electroluminescent lines in ZnS powder particles II. Models and comparison with experience, *J. Electrochem. Soc.*, 110 (1963) 733-747.

[16] N. E. Grzeskowiak, J. F. Winkelz, Structure and location of electroluminescent light emission within ZnS/Cu ACEL powder phosphor particles, *J. Electrochem. Soc.*, 154 (2007) J289-J294.

[17] S. Medling, F. Bridges, S. A. Carter, Local degradation of electroluminescent emission centers in ZnS:Cu,Cl phosphors, *J. Lumin.*, 134 (2013) 251-254.

[18] F. Chen, A. H. Kitai, Y. Xiang, Temperature-dependent degradation of AC powder EL, *J. Electrochem. Soc.*, 156 (2009) H585-H587.

[19] K. Hirabayashi, H. Kozawaguchi, B. Tsujiyama, Study on A-C powder EL phosphor deterioration factors, *J. Electrochem. Soc.*, 130 (1983) 2259-2263.

[20] A. A. Bol, J. Ferwerda, J. A. Bergwerff, A. Meijerink, Luminescence of nanocrystalline ZnS:$Cu^{2+}$, *J. Lumin.*, 99 (2002) 325-334.

[21] J. Stanley, Y. Jiang, F. Bridges, S. A. Carter, L. Ruhlen, Degradation and rejuvenation studies of AC electroluminescent ZnS:Cu,Cl phosphors, *J. Phys. Condens. Matter*, 22 (2010) 055301.

[22] N. E. Brese, C. L. Rohrer, G. S. Rohrer, Brightness degradation in electroluminescent ZnS:Cu, *Solid State Ionics*, 123 (1999) 19-24.

[23] G. Anoop, K. M. Krishna, M. K. Jayaraj, The effect of Mg incorporation on structural and optical properties of $Zn_2GeO_4$:Mn Phosphor, *J. Electrochem. Soc.*,155 (2008) J7-J10.

[24] T. Minami, Y. Kuroi, T. Miyata, H. Yamada, S. Takata, $ZnGa_2O_4$ as host material for multicolor-emitting phosphor layer of electroluminescent devices, *J. Lumin.*, 72 (1997) 997-998.

[25] I. K. Jeong, H. L. Park, S. I. Mho, Photoluminescence of $ZnGa_2O_4$ mixed with $InGaZnO_4$, *Solid State Ionics*, 108 (1998) 823-826.

[26] K. M. Krishna, G. Anoop, M. K. Jayarajz, Host sensitized white luminescence from $ZnGa_2O_4:Dy^{3+}$ phosphor, *J. Electrochem. Soc.*, 154 (2007) J310-J313.

[27] K. H. Hsu, M. R. Yang, K. S. Chen, A study of $ZnGa_2O_4$ phosphor prepared by the solid method, *J. Mater. Sci.-Mater. Electron.*, 9 (1998) 283-288.

[28] L. C. Williams, D. Norton, J. Budai, P. H. Holloway, Cathodoluminescence from thin film $Zn_2GeO_4$:Mn phosphor grown by pulsed laser deposition, *J. Electrochem. Soc.*, 151 (2004) H188-H191.

[29] J. S. Lewis, P. H. Holloway, Sputtering deposition and electroluminescence of $Zn_2GeO_4$:Mn, *J. Electrochem. Soc.*, 147 (2000) 3148-3150.

[30] J. P. Bender, J. F. Wager, J. Kissick, B. L. Clark, D. A. Keszler, $Zn_2GeO_4$:Mn alternating-current thin-film eletroluminesent devices, *J. Lumin.*, 99 (2002) 311-324.

[31] T. Xiao, A. H. Kitai, G. Liu, A. Nakua, J. Barbier, Thin film electroluminescence in highly anisotropic oxide materials, *Appl. Phys. Lett.*, 72 (1998) 3356-3358.

[32] X. Ouyang, A. H. Kitai, T. Xiao, Electroluminescence of the oxide thin film phosphors $Zn_2SiO_4$and $Y_2SiO_5$, *J. Appl. Phys.*, 79 (1996) 3229-3234.

[33] A. H. Kitai, *Solid State Luminescence*. London: Chapam & Hall, 1993.

[34] H. W. Leverenz, *An introduction to luminescence of solids*. New York: John Wiley & Sons Inc., 1950.

[35] A. Vecht, R. Ellis, Direct current electroluminescence in the zinc sulphide/copper/manganese system, *Nature*, 210 (1966) 1251-1252.

[36] H. K. Henisch, *Electroluminescence*. Oxford: Progamon, 1962.

[37] L. E. Tannas, *Flat-panel displays and CRTs*. New York: Van Nostrand Reinhold Company Inc., 1985.

[38] A. G. Fischer, Electroluminescent II-VI Heterojunctions, *J. Electrochem. Soc.*, 118 (1971) 139c.

[39] T. P. Brody, F. C. Luo, Z. P. Szepesi, D. H. Davies, A 6 x 6-in 20-lpi electroluminescent display panel, *IEEE Trans. electron devices*, 22 (1975) 739.

[40] M. Sawada, S. Oobayashi, K. Yamaguchi, H. Takemura, M. Nakamura, K. Momose, H. Saka, Characteristics of light emission lifetime of electroluminescent phosphor encapsulated by titanium–silicon–oxide film, *Jpn. J. Appl. Phys.*, 41 (2002) 3885-3889.

[41] S. Shionoya, W. M. Yen, *Phosphor handbook*. New York: CRC Press LLC, 1998.

[42] P. M. Jaffe, On the theory of electroluminescence deterioration, *J. Electrochem. Soc.*, 108 (1961) 711.

[43] Y. Y. Chen, J. G. Duh, B. S. Chiou, C. G. Peng, Luminescent mechanisms of ZnS:Cu:Cl and ZnS:Cu:Al phosphors, *Thin Solid Films*, 392 (2001) 50-55.

[44] H. Gobrecht, H. E. Gumlich, Sur le renforcement et l'extinction par les champs e´lectriques alternatifs de la luminescence des sulfures de zinc active´s au manganese, *J. Phys. Radium* 17 (1956) 754-757.

[45] W. A. Thornton, Electroluminescence maintenance, *J. Electrochem. Soc.*, 107 (1960) 895-907.

[46] W. A. Thornton, Electroluminescence in zinc sulfide, *Phys. Rev.* 102 (1956) 38.

[47] D. R. Vij, *Handbook of Electroluminescent Materials*. London: Institute of Physics Publishing Ltd., 2004.

[48] B. Wagstaff, A. Kitai, Electroluminescence of $Zn_2GeO_4$:Mn through SiC whisker electric field enhancement, *J. Lumin.*, 167 (2015) 310.

[49] A. G. Fischer, Electroluminescent lines in ZnS powder particles. I. Embedding media and basic observations, *J. Electrochem. Soc.*, 109 (1962) 1047.

[50] M. Warkentin, F. Bridges, S. A. Carter, M. Anderson, Electroluminescence materials ZnS:Cu,Cl and ZnS:Cu,Mn,Cl studied by EXAFS spectroscopy, *Phys. Rev. B*, 75 (2007) 075301.

[51] A. H. Kitai, *Solid state luminescence*. London: Chapam & Hall, 1993.

[52] Y. A. Ono, *Electroluminescent displays*. Singapore: World Scientific Publishing Co. Pte. Ltd, 1995.

[53] C. X. Guo, S. Y. Zhang, B. L. Li, L. Xu, Microscopic structure and distribution of Cu in the electroluminescence phosphor ZnS:Cu, *J. Lumin.*, 782 (1988) 40-41.

[54] S. Medling, C. France, B. Balaban, M. Kozina, Y. Jiang, F. Bridges, S. A. Carter, Understanding and improving electroluminescence in mill-ground ZnS:Cu,Cl phosphors. *J. Phys. D: Appl. Phys.*, 44 (2011) 205402.

[55] G. R. Fern, T. Ireland, P. Harris, J. Silver, R. Withnall, A. Salimian, P. K. Santra, M. Leoni, A. Erko, A. Lennie, C. C. Tang, Crystal structure of quenched and in-field electroluminescent phosphors. *Diamond Light Source Proceedings*, 1 (2010) e106.

[56] T. G. Ireland, J. Silver, Studies on the orientation of ACEL ZnS:Cu particles in applied AC fields, *ECS J. Solid State Sci. and Technol.*, 3 (2014) R25-R32.

[57] J. L. Gillson, F. J. Darnell, Electroluminescence in zinc sulfide, *Phys. Rev.*, 125 (1962) 149.

[58] M. Bredol, H. S. Dieckhoff, Materials for powder-based AC-electroluminescence, *Materials*, 3 (2010) 1353-1374.

[59] E. Bacaksız, T. D. Dzhafarov, V. D. Novruzov, K. Öztürk, M. Tomakin, T. Küçükömeroğlu, M. Altunbaş, E. Yanmaz, B. Abay, Copper diffusion in ZnS thin film. *Phys. Status Solidi A*, 201(2004) 2984.

[60] K. Hirabayashi, H. Kozawaguchi, B. Tsujiyama, Study on AC powder EL phosphor deterioration factors. *J. Electrochem. Soc.*, 130 (1983) 2259-2263.

[61] J. Schanda, *Colorimetry: Understanding the CIE system*. New York: John Wiley & Sons Inc., 2007.

[62] G. Blasse, B. C. Grabmaier, *Luminescent Materials*. Berlin: Springer-Verlag, 1994.

[63] J. A. Duffy, *Bonding, energy levels and bands in inorganic solids*. New York: John Wiley & Sons Inc., 2008.

[64] D. S. McClure, Optical spectra of exchange coupled $Mn^{++}$ ion pairs in ZnS:MnS, *J. Chem. Phys.*, 39 (1963) 2850.

[65] R. E. Shrader, S. Larach, P. N. Yocom, Cathodoluminescence efficiency of $Tm^{+3}$ in zinc sulfide, *J. appl. Phys*., 42 (1971) 4529.

[66] Y. T. Nien, I. G. Chen, C. S. Hwang, S. Y. Chu, Microstructure and electroluminescence of ZnS:Cu,Cl phosphor powders prepared by firing with CuS nanocrystallites, *J. Electrochem. Soc.*, 17, (2006) 299-303.

[67] A. Suzuki, S. Shionoya, Mechanism of the green-copper luminescence in ZnS crystals. I. Direct evidence for the pair emission mechanism, *J. Phys. Soc. Jpn.*, 31 (1971) 1455-1461.

[68] T. Minami, T. Miyata, S. Takata, I. Fukada, High-luminance green $Zn_2SiO_4$:Mn thin-film electroluminescent devices using an insulating $BaTiO_3$ ceramic sheet, *Jpn. J. Appl. Phys.*, 30 (1991) L117.

[69] B. K. Wanger, F. Zhang, P. Manigault, W. Park, C. J. Summers, P. N. Yocom, D. Zarimba, Recent development in low voltage cathodoluminescent phosphors, *Processing of the 7th International Display Workshops*, 2000.

[70] T. Miyata, T. Minami, K. Saikai, S. Takata, $Zn_2SiO_4$ as a host material for phosphor-emitting layers of TFEL devices, *J. Lumin.*, 926 (1994) 60-61.

[71] A. H. Kitai, Oxide phosphor and dielectric thin films for electroluminescent devices, *Thin Solid Films* 445 (2003) 367-376.

[72] G. Stuyven, P. D. Visschere, K. Neyts, A. Kitai, Characterization of the electro-optical behavior of $Zn_2Si_{0.5}Ge_{0.5}O_4$:Mn thin-film electroluminescent devices, *J. Appl. Phys.*, 93 (2003) 4622-4627.

[73] T. Xiao, A. H. Kitai, G. Liu, A. Nakua, Bright green oxide phosphors for EL devices, *SID Symposium Digest of Technical Papers*, 28 (1997) 419-422.

[74] J. R. Morones, J. L. Elechiguerra, A. Camacho, K. Holt, J. B. Kouri, J. T. Ramirez, M. J. Yacaman, The bactericidal effect of silver nanoparticles, *Nanotechnology*, 16 (2005) 2346-2353.

[75] S. C. Farmer, T. E. Patten, Photoluminescent polymer/quantum dot composite nanoparticles, *Chem. Mater.*, 13 (2001) 3920-3926.

[76] H. Zeng, G. Duan, Y. Li, S. Yang, X. Xu, W. Cai, Blue luminescence of ZnO nanoparticles based on non-equilibrium processes: defect origins and emission controls, *Adv. Funct. Mater.*, 20 (2010) 561-572.

[77] E. H. Sargent, Colloidal quantum dot solar cells, *Nat. Photon.*, 6 (2012) 133-135.

[78] H. Y. Wang, A. C. Lua, Development of metallic nickel nanoparticle catalyst for the decomposition of methane into hydrogen and carbon nanofibers, *J. Phys. Chem. C*, 116 (2012) 26765-26775.

[79] W. J. E. Beek, M. M. Wienk, R. A. J. Janssen, Efficient hybrid solar cells from zinc oxide nanoparticles and a conjugated polymer, *Adv. Mater.*, 16 (2004) 1009-1013.

[80] N. Padmavathy, R. Vijayaraghavan, Enhanced bioactivity of ZnO nanoparticles-an antimicrobial study, *Sci. Technol. Adv. Mater.*, 9 (2008) 035004.

[81] W. T. Al-Jamal, K. T. Al-Jamal, P. H. Bomans, P. M. Frederik, K. Kostarelos, Functionalized-quantum-dot-liposome hybrids as multimodal nanoparticles for cancer, *Small*, 4 (2008) 1406-1415.

[82] R. Schreiber, J. Do, E. M. Roller, T. Zhang, V. J. Schuller, P. C. Nickels, J. Feldmann, T. Liedl, Hierarchical assembly of metal nanoparticles, quantum dots and organic dyes using DNA origami scaffolds, *Nat. Nanotech.*, 9 (2014) 74-78.

[83] W. Cao, C. Xiang, Y. Yang, Q. Chen, L. Chen, X. Yan, L. Qian, Highly stable QLEDs with improved hole injection via quantum dot structure tailoring, *Nat. Commun.*, 9 (2018) 2608.

[84] P. Claus, A. Brückner, C. Mohr, H. Hofmeister, Supported gold nanoparticles from quantum dot to mesoscopic size scale: effect of electronic and structural properties on catalytic hydrogenation of conjugated functional groups, *J. Am. Chem. Soc.*, 122 (2000) 11430-11439.

[85] Y. P. Sun, B. Zhou. Y. Lin, W. Wang, K. A. S. Fernando, P. Pathak, M. J. Meziani, B. A. Harruff, X. Wang, H. Wang, P. G. Luo, H. Yang, M. E. Kose, B. Chen, L. M. Veca, S. Y. Xie, Quantum-sized carbon dots for bright and colorful photoluminescence, *J. Am. Chem. Soc.*, 128 (2006) 7756-7757.

[86] I. Robel, M. Kuno, P. V. Kamat, Size-dependent electron injection from excited CdSe quantum dots into $TiO_2$ nanoparticles, *J. Am. Chem. Soc.*, 129 (2007) 4136-4137.

[87] P. V. Kamat, Quantum dot solar cells. Semiconductor nanocrystals as light harvesters, *J. Phys. Chem. C*, 112 (2008) 18737-18753.

[88] U. Hasegawa, S. M. Nomura, S. C. Kaul, T. Hirano, K. Akiyoshi, Nanogel-quantum dot hybrid nanoparticles for live cell imaging, *Biochem. Biophys. Res. Commun.*, 331 (2005) 917-921.

[89] H. Lv, Z. Xi, Z. Chen, S. Guo, Y. Yu, W. Zhu, Q. Li, X. Zhang, M. Pan, G. Lu, S. Mu, S. Sun, A new core/shell NiAu/Au nanoparticle catalyst with Pt-like activity for hydrogen evolution reaction, *J. Am. Chem. Soc.*, 137 (2015) 5859-5862.

[90] Y. Jin, J. Wang, B. Sun, J. C. Blakesley, N. C. Greenham, Solution-processed ultraviolet photodetectors based on colloidal ZnO nanoparticles, *Nano Lett.*, 8 (2008) 1649-1653.

[91] T. Mitsudome, Y. Mikami, H. Funai, T. Mizugaki, K. Jitsukawa, K. Kaneda, Oxidant-free alcohol dehydrogenation using a reusable hydrotalcite-supported silver nanoparticle catalyst, *Angew. Chem. Int. Ed.*, 47 (2008) 138-141.

[92] H. S. Choi, W. Liu, P. Misra, E. Tanaka, J. P. Zimmer, B. I. Ipe, M. G. Bawendi, J. V. Frangioni, Renal clearance of quantum dots, *Nat. Biotechnol.*, 25 (2007) 1165-1170.

[93] L. Qian, Y. Zheng, J. Xue, P. H. Holloway, Stable and efficient quantum-dot light-emitting diodes based on solution-processed multilayer structures, *Nat. Photon.*, 5 (2011) 543-548.

[94] L. Wang, Q. Xiong, F. Xiao, H. Duan, 2D nanomaterials based electrochemical biosensors for cancer diagnosis, *Biosens. Bioelectron.*, 89 (2017) 136-151.

[95] J. C. Spear, B.W. Ewers, J. D. Batteas, 2D-nanomaterials for controlling friction and wear at interfaces, *Nano Today*, 10 (2015) 301-314.

[96] C. H. Lambert, S. Mangin, B. S. D. Ch. S. Varaprasad, Y. K. Takahashi, M. Hehn, M. Cinchetti, G. Malinowski, K. Hono, Y. Fainman, M. Aeschlimann, E. E. Fullerton, All-optical control of ferromagnetic thin films and nanostructures, *Science*, 345 (2014) 1337-1340.

[97] L. J. Brennan, M. T. Byrne, M. Bari, Y. K. Gun'ko, Carbon nanomaterials for dye-sensitized solar cell applications: A bright future, *Adv. Energy Mater.*, 1 (2011) 472-485.

[98] J. You, M. Li, B. Ding, X. Wu, C. Li, Crab chitin-based 2D soft nanomaterials for fully biobased electric devices, *Adv. Mater.*, 29 (2017) 1606895.

[99] S. Su, J. Chao, D. Pan, L. Wang, C. Fan, Electrochemical sensors using two-dimensional layered nanomaterials, *Electroanalysis*, 27 (2015) 1062-1072.

[100] D. S. Hecht, L. Hu, G. Irvin, Emerging transparent electrodes based on thin films of carbon nanotubes, graphene, and metallic nanostructures, *Adv. Mater.*, 23 (2011) 1482-1513.

[101] M. W. J. Prins, K. O. Grosse-Holz, G. Müller, J. F. M. Cillessen, J. B. Giesbers, R. P. Weening, R. M. Wolf, A ferroelectric transparent thin-film transistor, *Appl. Phys. Lett.*, 68 (1996) 3650-3652.

[102] L. Peng, Z. Fang, Y. Zhu, C. Yan, G. Yu, Holey 2D nanomaterials for electrochemical energy storage, *Adv. Energy Mater.*, 8 (2018) 1702179.

[103] T. N. Narayanan, B. K. Gupta, S. A. Vithayathil, R. R. Aburto, S. A. Mani, J. Taha-Tijerina, B. Xie, B. A. Kaipparettu, S. V. Torti, P. M. Ajayan, Hybrid 2D nanomaterials as dual-mode contrast agents in cellular imaging, *Adv. Mater.*, 24 (2012) 2992-2998.

[104] Y. Jing, Z. Zhou, C. R. Cabrera, Z. Chen, Metallic $VS_2$ monolayer: A promising 2D anode material for lithium ion batteries, *J. Phys. Chem. C*, 117 (2013) 25409-25413.

[105] C. D. Schaper, Patterned transfer of metallic thin film nanostructures by water-soluble polymer templates, *Nano Lett.*, 3 (2003) 1305-1309.

[106] B. Luo, G. Liu, L. Wang, Recent advances in 2D materials for photocatalysis, *Nanoscale*, 8 (2016) 6904-6920.

[107] P. K. Kannan, D. J. Late, H. Morgan, C. S. Rout, Recent developments in 2D layered inorganic nanomaterials for sensing, *Nanoscale*, 7 (2015) 13293-13312.

[108] K. Nomura, H. Ohta, A. Takagi, T. Kamiya, M. Hirano, H. Hosono, Room-temperature fabrication of transparent flexible thin-film transistors using amorphous oxide semiconductors, Nature, 432 (2004) 488-491.

[109] Y. Zhu, L. Peng, Z. Fang, C. Yan, X. Zhang, G. Yu, Structural engineering of 2D nanomaterials for energy storage and catalysis, *Adv. Mater.*, 30 (2018) 1706347.

[110] Y. Guo, K. Xu, C. Wu, J. Zhao, Y. Xie, Surface chemical-modification for engineering the intrinsic physical properties of inorganic two-dimensional nanomaterials, *Chem. Soc. Rev.*, 44 (2015) 637-646.

[111] J. Xiong, J. Di, J. Xia, W. Zhu, H. Li, Surface defect engineering in 2D nanomaterials for photocatalysis, *Adv. Funct. Mater.*, 28 (2018) 1801983.

[112] J. Britt, C. Ferekides, Thin-film CdS/CdTe solar cell with 15.8% efficiency, *Appl. Phys. Lett.*, 62 (1993) 2851-2852.

[113] X. Peng, L. Peng, C. Wu, Y. Xie, Two dimensional nanomaterials for flexible supercapacitors, *Chem. Soc. Rev.*, 43 (2014) 3303-3323.

[114] A. H. Khan, S. Ghosh, B. Pradhan, A. Dalui, L. K. Shrestha, S. Acharya, K. Ariga, Two-dimensional (2D) nanomaterials towards electrochemical nanoarchitectonics in energy-related applications, *Bull. Chem. Soc. Jpn.*, 90 (2017) 627-648.

[115] Y. Huang, X. Duan, Y. Cui, L. J. Lauhon, K. H. Kim, C. M. Lieber, Logic gates and computation from assembled nanowire building blocks, *Science*, 294 (2001) 1313-1317.

[116] M. H. Huang, S. Mao, H. Feick, H. Yan, Y. Wu, H. Kind, E. Weber, R. Russo, P. Yang, Room-temperature ultraviolet nanowire nanolasers, *Science*, 292 (2001) 1897-1899.

[117] M. S. Gudiksen, L. J. Lauhon, J. Wang, D. C. Smith, C. M. Lieber, Growth of nanowire superlattice structures for nanoscale photonics and electronics, *Nature*, 415 (2002) 617-620.

[118] K. Peng, Y. Xu, Y. Wu, Y. Yan, S. T. Lee, J. Zhu, Aligned single-crystalline Si nanowire arrays for photovoltaic applications, *Small*, 1 (2005) 1062-1067.

[119] B. Tian, T. J. Kempa, C. M. Lieber, Single nanowire photovoltaics, *Chem. Soc. Rev.*, 38 (2008) 16-24.

[120] L. Liao, Y. C. Lin, M. Bao, R. Cheng, J. Bai, Y. Liu, Y. Qu, K. L. Wang, Y. Huang, X. Duan, High-speed graphene transistors with a self-aligned nanowire gate, *Nature*, 467 (2010) 305-308.

[121] G. Wang, H. Wang, Y. Ling, Y. Tang, X. Yang, R. C. Fitzmorris, C. Wang, J. Z. Zhang, Y. Li, Hydrogen-treated $TiO_2$ nanowire arrays for photoelectrochemical water splitting, *Nano Lett.*, 11 (2011) 3026-3033.

[122] H. Kind, H. Yan, B. Messer, M. Law, P. Yang, Nanowire ultraviolet photodetectors and optical switches, *Adv. Mater.*, 14 (2002) 158-160.

[123] C. Thelander, P. Agarwal, S. Brongersma, J. Eymery, L. F. Feiner, A. Forchel, M. Scheffler, W. Riess, B. J. Ohlsson, U. Gösele, L. Samuelson, Nanowire-based one-dimensional electronics, *Materials Today*, 9 (2006) 28-35.

[124] K. Takei, T. Takahashi, J. C. Ho, H. Ko, A. G. Gillies, P. W. Leu, R. S. Fearing, A. Javey, Nanowire active-matrix circuitry for low-voltage macroscale artificial skin, *Nat. Mater.*, 9 (2010) 821-826.

[125] E. Garnett, P. Yang, Light trapping in silicon nanowire solar cells, *Nano Lett.*, 10 (2010) 1082-1087.

[126] Y. Li, F. Qian, J. Xiang, C. M. Lieber, Nanowire electronic and optoelectronic devices, *Materials Today*, 9 (2006) 18-27.

[127] M. T. Björk, B. J. Ohlsson, C. Thelander, A. I. Persson, K. Deppert, L. R. Wallenberg, L. Samuelson, Nanowire resonant tunneling diodes, *Appl. Phys. Lett.*, 81 (2002) 4458-4460.

[128] L. Cao, J. S. White, J. S. Park, J. A. Schuller, B. M. Clemens, M. L. Brongersma, Engineering light absorption in semiconductor nanowire devices, *Nat. Mater.*, 8 (2009) 643-647.

[129] J. Xiang, W. Lu, Y. Hu, Y. Wu, H. Yan, C. M. Lieber, Ge/Si nanowire heterostructures as high-performance field-effect transistors, *Nature*, 441 (2006) 489-493.

[130] Y. Cui, Z. Zhong, D. Wang, W. U. Wang, and C. M. Lieber, High performance silicon nanowire field effect transistors, *Nano Lett.*, 3 (2003) 149-152.

[131] J. Goldberger, A. Hochbaum, R. Fan, P. Yang, Silicon vertically integrated nanowire field effect transistors, *Nano Lett.*, 6 (2006) 973-977.

[132] Z. S. Wu, W. Ren., D. W. Wang, F. Li, B. Liu, H. M. Cheng, High-energy $MnO_2$ nanowire/graphene and graphene asymmetric electrochemical capacitors, *ACS Nano*, 4 (2010) 5835-5842.

[133] R. Könenkamp, R.C. Word, C. Schlegel, Vertical nanowire light-emitting diode, *Appl. Phys. Lett.*, 85 (2004) 6004-6006.

[134] C. Soci, A. Zhang, B. Xiang, S. A. Dayeh, D. P. R. Aplin, J. Park, X. Y. Bao, Y. H. Lo, D. Wang, ZnO nanowire UV photodetectors with high internal gain, *Nano Lett.*, 7 (2007) 1003-1009.

[135] Z. L. Wang, ZnO nanowire and nanobelt platform for nanotechnology, *Mater. Sci. Eng. R*, 64 (2009) 33-71.

[136] Y. W. Heo, D. P. Norton, L. C. Tien, Y. Kwon, B. S. Kang, F. Ren, S. J. Pearton, J. R. LaRoche, ZnO nanowire growth and devices, *Mater. Sci. Eng. R*, 47 (2004) 1-47.

[137] B. Meyer, D. Marx, Density-functional study of the structure and stability of ZnO surfaces, *Phys. Rev. B*, 67 (2003) 035403.

[138] C. Klingshirn, ZnO: From basics towards applications, *phys. Stat. Sol. (b)*, 244 (2007) 3027-3073.

[139] Z. L. Wang, J. Song, Piezoelectric nanogenerators based on zinc oxide nanowire arrays, *Science*, 312 (2006) 242-246.

[140] Q. Wan, Q. H. Li, Y. J. Chen, T. H. Wang, X. L. He, J. P. Li, C. L. Lin, Fabrication and ethanol sensing characteristics of ZnO nanowire gas sensors, *Appl. Phys. Lett.*, 84 (2004) 3654-3656.

[141] W. U. Huynh, J. J. Dittmer, A. P. Alivisatos, Hybrid nanorod-polymer solar cells, *Science*, 295 (2002) 2425-2427.

[142] P. G. Collins, A. Zettl, H. Bando, A. Thess, R. E. Smalley, Nanotube nanodevice, *Science*, 278 (1997) 100-102.

[143] H. W. Ch. Postma, T. Teepen, Z. Yao, M. Grifoni, C. Dekker, Carbon nanotube single-electron transistors at room temperature, *Science*, 293 (2001) 76-79.

[144] P. L. McEuen, M. S. Fuhrer, H. Park, Single-walled carbon nanotube electronics, *IEEE Trans. Nanotechnol.*, 1 (2002) 78-85.

[145] P. Avouris, J. Appenzeller, R. Martel, S.J. Wind, Carbon nanotube electronics, *Proc. IEEE*, 91 (2003) 1772-1784.

[146] W. B. Choi, D. S. Chung, J. H. Kang, H. Y. Kim, Y. W. Jin, I. T. Han, Y. H. Lee, J. E. Jung, N. S. Lee, G. S. Park, J. M. Kim, Fully sealed, high-brightness carbon-nanotube field-emission display, *Appl. Phys. Lett.*, 75 (1999) 3129-3131.

[147] C. Niu, E. K. Sichel, R. Hoch, D. Moy, H. Tennent, High power electrochemical capacitors based on carbon nanotube electrodes, *Appl. Phys. Lett.*, 70 (1997) 1480-1482.

[148] A. Javey, J. Guo, Q. Wang, M. Lundstrom, H. Dai, Ballistic carbon nanotube field-effect transistors, *Nature*, 424 (2003) 654-657.

[149] V. Sazonova, Y. Yaish, Hande Üstünel, D. Roundy,, T. A. Arias, P. L. McEuen, A tunable carbon nanotube electromechanical oscillator, *Nature*, 431 (2004) 284-287.

[150] E. Hammel, X. Tang, M. Trampert, T. Schmitt, K. Mauthner, A. Eder, P. Pötschke, Carbon nanofibers for composite applications, *Carbon*, 42 (2004) 1153-1158.

[151] V. G. Dubrovskii, G. E. Cirlin, V. M. Ustinov, Semiconductor nanowhiskers: Synthesis, properties, and applications, *Semiconductors*, 43 (2009) 1539-1584.

[152] Q. X. Zhao, M. Willander, R. E. Morjan, Q. H. Hu, E. E. B. Campbell, Optical recombination of ZnO nanowires grown on sapphire and Si substrates, *Appl. Phys. Lett.*, 83 (2003) 165-167.

[153] X. Wang, C. J. Summers, Z. L. Wang, Large-scale hexagonal-patterned growth of aligned ZnO nanorods for nano-optoelectronics and nanosensor arrays, Nano Lett, 4 (2004) 423-426.

[154] H. T. Ng, J. Li, M. K. Smith, P. Nguyen, A. Cassell, J. Han, M. Meyyappan, Growth of epitaxial nanowires at the junctions of nanowalls, *Science*, 300 (2003) 1249.

[155] M. Yan, H. T. Zhang, E. J. Widjaja, R. P. H. Chang, Self-assembly of well-aligned gallium-doped zinc oxide nanorods, *J. Appl. Phys.*, 94 (2003) 5240-5246.

[156] Z. Gu, M. P. Paranthaman, J. Xu, Z. W. Pan, Aligned ZnO nanorod arrays grown directly on zinc foils and zinc spheres by a low-temperature oxidization method, *ACS Nano*, 3 (2009) 273–278.

[157] W. I. Park, D. H. Kim, S. W. Jung, G. C. Yi, Metalorganic vapor-phase epitaxial growth of vertically well-aligned ZnO nanorods. *Appl. Phys. Lett.*, 80 (2002) 4232-4234.

[158] J. J. Wu, S. C. Liu, Low-temperature growth of well-aligned ZnO nanorods by chemical vapor deposition. *Adv. Mater.*, 14 (2002) 215-218.

[159] H. Yuan, Y. Zhang, Preparation of well-aligned ZnO whiskers on glass substrate by atmospheric MOCVD, *J. Cryst. Growth*, 263 (2004) 119-124.

[160] Vayssieres, L. Growth of arrayed nanorods and nanowires of ZnO from aqueous solutions, *Adv. Mater.*, **15** (2003) 464-466.

[161] L. E. Greene, M. Law, D. H. Tan, M. Montano, J. Golderger, G. Somorjai, P. Yang, General route to vertical ZnO nanowire arrays using textured ZnO seeds, *Nano Lett.*, 5 (2005) 1231-1236.

[162] Z. R. Tian, J. A. Voigt, J. Liu, B. McKenzie, M. J. McDermott, M. A. Rodrigue, H. Konishi, H. Xu, Complex and oriented ZnO nanostructures. *Nat. Mater.*, 2 (2003) 821-826.

[163] R. S. Wagner, W. C. Ellis, Vapor-liquid-solid mechanism of single crystal growth, *Appl. Phys. Lett.*, 4 (1964) 89.

[164] R. S. Wagner, *VLS mechanism of crystal growth in whisker technology*. New York: John Wiley & Sons Inc., 1970.

[165] E. I. Givargizov, Fundamental aspects of VLS growth, *J. Cryst. Growth*, 31 (1975) 20-30.

[166] S. Xu, N. Adiga, S. Ba, T. Dasgupta, C. F. J. Wu, Z. L. Wang, Optimizing and improving the growth quality of ZnO nanowire arrays guided by statistical design of experiments, *ACS Nano*, 3 (2009) 1803-1212.

[167] L. E. Greene, B. D. Yuhas, M. Law, D. Zitoun, P. Yang, Solution-grown zinc oxide nanowires, *Inorg. Chem.*, 45 (2006) 7535-7543.

[168] Q. Li, J. Bian, J. Sun, J. Wang, Y. Luo, K. Sun, D. Yu, Controllable growth of well-aligned ZnO nanorod arrays by low-temperature wet chemical bath deposition method, *Appl. Surf. Sci.*, 256 (2010) 1698-1702.

[169] Z. Han, S. Li, J. Chu, Y. Chen, Controlled growth of well-aligned ZnO nanowire arrays using the improved hydrothermal method, *J. Semicond.*, 34 (2013) 063002.

[170] S. Xu, C. Lao, B. Weintraub, Z. L. Wang, Density-controlled growth of aligned ZnO nanowire arrays by seedless chemical approach on smooth surfaces, *J. Mater. Res.*, 23 (2011) 2072-2077.

[171] L. Roza, M. Y. A. Rahman, A. A. Umar, M. M. Salleh, Direct growth of oriented ZnO nanotubes by self-selective etching at lower temperature for photo-electrochemical (PEC) solar cell application, *J. Alloys. Compd.*, 618 (2015) 153-158.

[172] J. Qiu, X. Li, W. He, S. J. Park, H. K. Kim, Y. H. Hwang, J. H. Lee, Y. D. Kim, The growth mechanism and optical properties of ultralong ZnO nanorod arrays with a high aspect ratio by a preheating hydrothermal method, *Nanotechnology*, 20 (2009) 155603.

[173] C. L. Hsu, K. C. Chen, Improving piezoelectric nanogenerator comprises ZnO nanowires by bending the flexible PET substrate at low vibration frequency, *J. Phys. Chem. C*, 116 (2012) 9351-9355.

[174] T. Mahalingam, K. M. Lee, K. H. Park, S. Lee, Y. Ahn, J. Y. Park, K. H. Koh, Low temperature wet chemical synthesis of good optical quality vertically aligned crystalline ZnO nanorods, *Nanotechnology*, 18 (2007) 035606.

[175] S. H. Yi, S. K. Choi, J. M. Jang, J. A. Kim, W. G. Jung, Low-temperature growth of ZnO nanorods by chemical bath deposition, *J. Colloid. Interface Sci.*, 313 (2007) 705-710.

[176] X. Jiang, T. Herricks, Y. Xia, CuO nanowires can be synthesized by heating copper substrates in air, *Nano Lett.*, 2 (2002) 1333-1338.

[177] M. L. Zhong, D. C. Zeng, Z. W. Liu, H. Y. Yu, X. C. Zhong, W. Q. Qiu, Synthesis, growth mechanism and gas-sensing properties of large-scale CuO nanowires, *Acta Mater.*, 58 (2010) 5926-5932.

[178] J. Zhang, B. Wang, J. Zhou, R. Xia, Y. Chu, J. Huang, Preparation of advanced CuO nanowires/functionalized graphene composite anode material for lithium ion batteries, *Materials*, 10 (2017) 72.

[179] L. Liao, Z. Zhang, B. Yan, Z. Zheng, Q. L. Bao, T. Wu, C. M. Li, Z. X. Shen, J. X. Zhang, H. Gong, J. C. Li, T. Yu, Multifunctional CuO nanowire devices: p-type field effect transistors and CO gas sensors, *Nanotechnology*, 20 (2009) 085203.

[180] A. M. B. Gonçalves, L. C. Campos, A. S. Ferlauto, R. G. Lacerda, On the growth and electrical characterization of CuO nanowires by thermal oxidation, *J. Appl. Phys.*, 106 (2009) 034303.

[181] P. Raksa, A. Gardchareon, T. Chairuangsri, P. Mangkorntong, N. Mangkorntong, S. Choopun, Ethanol sensing properties of CuO nanowires prepared by an oxidation reaction, *Ceram. Int.*, 35 (2009) 649-652.

[182] M. Farbod, N. M. Ghaffari, I. Kazeminezhad, Effect of growth parameters on photocatalytic properties of CuO nanowires fabricated by direct oxidation, *Mater. Lett.*, 81 (2012) 258-260.

[183] H. T. Hsueh, T. J. Hsueh, S. J. Chang, F. Y. Hung, T. Y. Tsai, W. Y. Weng, C. L. Hsu, B. T. Dai, CuO nanowire-based humidity sensors prepared on glass substrate, *Sensors Actuat. B:Chem.*, 156 (2011) 906-911.

[184] J. Chen, K. Wang, L. Hartman, W. Zhou, $H_2S$ detection by vertically aligned CuO nanowire array sensors, *J. Phys. Chem. C*, 112 (2008) 16017-16021.

[185] A. Kargar, Y. Jing, S. J. Kim, C. T. Riley, X. Pan, D. Wang, ZnO/CuO heterojunction branched nanowires for photoelectrochemical hydrogen generation, *ACS Nano*, 7 (2013) 11112-11120.

[186] L. B. Luo, X. H. Wang, C. Xie, Z. J. Li, R. Lu, X. B. Yang, J. Lu, One-dimensional CuO nanowire: synthesis, electrical, and optoelectronic devices application, *Nanoscale Res. Lett.*, 9 (2014) 637.

[187] H. Wan, H. E. Ruda, A study of the growth mechanism of CVD-grown ZnO nanowires, *J. Mater. Sci.:Mater. Electron.*, 21(2010) 1014-1049.

[188] J. Song, X. Wang, E. Riedo, Z. L. Wang, Systematic study on experimental conditions for large-scale growth of aligned ZnO nanowires on nitrides, *J. Phys. Chem. B*, 109 (2005) 9869-9872.

[189] X. Wang, J. Song, P. Li, J. H. Ryou, R. D. Dupuis, C. J. Summers, Z. L. Wang, Growth of uniformly aligned ZnO nanowire heterojunction arrays on GaN, AlN, and $Al_{0.5}Ga_{0.5}N$ substrates, *J. Am. Chem. Soc.*, 127 (2005) 7920-7923.

[190] X. Wang, J. Song, Z. L. Wang, Nanowire and nanobelt arrays of zinc oxide from synthesis to properties and to novel devices, *J. Mater. Chem.*, 17 (2007) 711-720.

[191] M. Kirkham, X. Wang, Z. L. Wang, R. L. Snyder, Solid Au nanoparticles as a catalyst for growing aligned ZnO nanowires: a new understanding of the vapour-liquid-solid process, *Nanotechnology*, 18 (2007) 365304.

[192] X. Wang, J. Song, C. J. Summers, J. H. Ryou, P. Li, R. D. Dupuis, Z. L. Wang, Density-controlled growth of aligned ZnO nanowires sharing a common contact: A simple, low-cost, and mask-free technique for large-scale applications, *J. Phys. Chem. B*, 110 (2006) 7720-7724.

[193] P. Yang, H. Yan, S. Mao, R. Russo, J. Johnson, R. Saykally, N. Morris, J. Pham, R. He, H. J. Choi, Controlled growth of ZnO nanowires and their optical properties, *Adv. Funct. Mater.*, 12 (2002) 323-331.

[194] M. H. Huang, Y. Wu, H. Feick, N. Tran, E. Weber, P. Yang, Catalytic growth of zinc oxide nanowires by vapor transport, *Adv. Mater.*, 13 (2001) 113-116.

[195] R. T. R., Kumar, E. McGlynn, M. Biswas, R. Saunders, G. Trolliard, B. Soulestin, J. R. Duclere, J. P. Mosnier, M. O. Henry, Growth of ZnO nanostructure on Au-coated Si: Influence of growth temperature on growth mechanism and morphology, *J. Appl. Phys.*, 104 (2008) 084309.

[196] S. H. Jo, Y. Tu, Z. P. Huang, D. L. Carnahan, D. Z. Wang, Z. F. Ren, Effect of length and spacing of vertically aligned carbon nanotubes on field emission properties, *Appl. Phys. Lett*., 82 (2003) 3520.

[197] S. H. Jo, J. Y. Tu, Z. F. Ren, R. A. Farrer, T. Baldacchini, J. T. Fourkas, Field-emission studies on thin films of zinc oxide nanowires, *Appl. Phys. Lett*., 83 (2003) 4821.

[198] L. Nilsson, O. Groening, C. Emmenegger, O. Kuettel, E. Schaller, L. Schlapbach, H. Kind, J. M. Bonard, and K. Kern, Scanning field emission from patterned carbon nanotube films, *Appl. Phys. Lett*., 76 (2000) 2071.

[199] J. M. Bonard, N. Weiss, H. Kind, T. Stöckli, L. Forró, K. Kern, A. Châtelain, Tuning the field emission properties of patterned carbon nanotube films, *Adv. Mater*., 13 (2001) 184-188.

[200] S. Ma, A. H. Kitai, ZnO nanowire growth by chemical vapor deposition with spatially controlled density on $Zn_2GeO_4$:Mn polycrystalline substrates, *Mater. Res. Express*, 4 (2017) 065012.

[201] K. Vanheusden, W. L.Warren, C. H. Seager, D. R. Tallant, J. A. Voigt, B. E. Gande, Mechanisms behind green photoluminescence in ZnO phosphor powders, *J. Appl. Phys*., 79 (1996) 7983.

[202] W. E. Rogers, *Introduction to electric field: A vector analysis approach*. New York: McGraw-Hill Inc., 1954.

[203] S. S. Bamji, A. T. Bulinski, K. M. Prasad, Electric field calculations with the boundary element method, *IEEE Trans. Electr. Insul.*, 28 (1993) 420-424.

[204] L. Cisse, S. S. Bamji, A. T. Bulinski, Electric field calculations for needle-plane geometry and space charge in polyethylene, *IEEE Trans. Dielectr. Electr. Insul.*, 10, (2003) 176-180.

[205] J. Y. Kim, S. H. Park, T. Jeong, M. J. Bae, S. Song, J. Lee, I. T. Han, D. Jung, S. Yu, Paper as a substrate for inorganic powder electroluminescence devices, *IEEE Trans. Electron. Devices*, 57 (2010) 1470-1474.

[206] S. Ma, Z. Peng, A. H. Kitai, A CuO nanowire-based alternating current oxide powder electroluminescent device with high stability, *Angew. Chem. Int. Ed.*, 57 (2018) 11267-11272.